Electron Microscopical Investigations of Doped and Undoped $Ba_{0.5}Sr_{0.5}Co_{0.8}Fe_{0.2}O_{3-d}$ for Oxygen Separation Membranes

Zur Erlangung des akademischen Grades eines
Doktors der Naturwissenschaften
von der Fakultät für Physik
des Karlsruher Instituts für Technologie (KIT)

genehmigte
Dissertation
von

Dipl.- Phys. Philipp Müller

aus Pforzheim

Tag der mündlichen Prüfung: 31. Mai 2013

Referentin: Prof. Dr. D. Gerthsen
Korreferentin: Prof. Dr.-Ing. E. Ivers-Tiffée

angefertigt am
Laboratorium für Elektronenmikroskopie (LEM)
Karlsruher Institut für Technologie (KIT)

Parts and excerpts of this thesis have already been published as journal articles. Figures are reprinted with permission:

Reprinted with permission from P. Müller, H. Störmer, L. Dieterle, C. Niedrig, E. Ivers-Tiffée, D. Gerthsen. Decomposition pathway of cubic $Ba_{0.5}Sr_{0.5}Co_{0.8}Fe_{0.2}O_{3-d}$ between 700 °C and 1000 °C analyzed by electron microscopic techniques. Solid State Ionics, 206:57-66, 2012.

Reprinted with permission from P. Müller, H. Störmer, M. Meffert, L. Dieterle, C. Niedrig, S. F. Wagner, E. Ivers-Tiffe and D. Gerthsen. Secondary Phase Formation in $Ba_{0.5}Sr_{0.5}Co_{0.8}Fe_{0.2}O_{3-d}$ Studied by Electron Microscopy. Chemistry of Materials, 25:564-573, 2013.

Reprinted with permission from D. Fuchs, P. Müller, A. Sleem, R. Schneider, D. Gerthsen and H. v. Löhneysen. Growth and interfacial properties of epitaxial $CaCuO_2$ thin films. Journal of Applied Physics, 112:103529, 2012.

Further results are submitted to a scientific journal and might be subject of copyright in the future.

Akronyms

AFM	Atomic Force Microscopy
BCO	$Ba_{n+1}Co_nO_{3n+3}(Co_8O_8)$
BSCF	$Ba_{0.5}Sr_{0.5}Co_{0.8}Fe_{0.2}O_{3-\delta}$
BSCF3X	$Ba_{0.5}Sr_{0.5}(Co_{0.8}Fe_{0.2})_{0.97}X_{0.03}O_{3-\delta}$
BSCF3Sc	$Ba_{0.5}Sr_{0.5}(Co_{0.8}Fe_{0.2})_{0.97}Sc_{0.03}O_{3-\delta}$
BSCF3Y	$Ba_{0.5}Sr_{0.5}(Co_{0.8}Fe_{0.2})_{0.97}Y_{0.03}O_{3-\delta}$
BSCF3Zr	$Ba_{0.5}Sr_{0.5}(Co_{0.8}Fe_{0.2})_{0.97}Zr_{0.03}O_{3-\delta}$
BSCFY	$Ba_{0.5}Sr_{0.5}(Co_{0.8}Fe_{0.2})_{1-x}Y_xO_{3-\delta}$
BSCFZ	$Ba_{0.5}Sr_{0.5}(Co_{0.8}Fe_{0.2})_{1-x}Zr_xO_{3-\delta}$
BSCZF	$Ba_{0.5}Sr_{0.5}(Co_{0.6}Zr_{0.2})Fe_{0.2}O_{3-\delta}$
BSE	Back Scattered Electrons
CBED	Convergent-Beam Electron Diffraction
CCO	$CaCuO_2$
CCS	Carbon Capture and Storage
DM	Digital Micrograph
EBPVD	Electron Beam Physical Vapor Deposition
EDXS	Energy-Dispersive X-ray Spectroscopy
EELS	Electron Energy Loss Spectroscopy
ELNES	Energy-Loss Near-Edge Structure
FEG	Field-Emission Gun
FIB	Focused Ion Beam
FOLZ	First Order Laue-Zone
FWHM	Full Width at Half Maximum
GIF	Gatan Imaging Filter
HOLZ	Higher Order Laue-Zones
HRTEM	High-Resolution Transmission Electron Microscopy
HAADF	High-Angle Annular Dark-Field
IFP	Institute of Solid State Physics

IKTS Fraunhofer Institut für Keramische Technologien und Systeme, Hermsdorf, Germany
IWE Institut für Werkstoffe der Elektrotechnik, KIT, Karlsruhe, Germany

JEMS Java Electron Microscopy Simulations

KIT Karlsruhe Institute of Technology

LSAT $(LaAlO_3)_{0.3}(Sr_2AlTaO_6)_{0.7}$
LSC $La_xSr_{1-x}CoO_{3-\delta}$
LSC64 $La_{0.6}Sr_{0.4}CoO_{3-\delta}$
LSCF $La_xSr_{1-x}Co_yFe_{1-y}O_{3-\delta}$

MIEC Mixed Ionic-Electronic Conductor
MLLS Multiple Linear Least Square

NGO $NdGaO_3$

PCA Principal Component Analysis
PIPS Precision Ion Polishing System
PLD Pulsed Laser Deposition

RBS Rutherford Backscattering Spectrometry

SAED Selected-Area Electron Diffraction
SCF $SrCo_{1-x}Fe_xO_{3-\delta}$
SE Secondary Electrons
SEM Scanning Electron Microscopy
SNR Signal-to-Noise Ratio
STEM Scanning Transmission Electron Microscopy
STO $SrTiO_3$
SQUID Superconducting QUantum Interference Device

TEM Transmission Electron Microscopy
TIA TEM Imaging and Analysis

XAS X-ray Absorption Spectroscopy
XPS X-ray Photoelectron Spectroscopy
XRD X-Ray Diffraction

ZLP Zero-Loss Peak
ZOLZ Zero Order Laue-Zone

Symbols

a	lattice parameter
Al	aluminium
Ar	argon
Ba	barium
Ca	calcium
Co	cobalt
Cu	copper
c_O	oxygen concentration
C_i	concentration of element i in a sample
d; δ	oxygen deficiency
D	diffusion coefficient
D	matrix containing spectra data for PCA
$\bar{D}$	nomalized matrix containing spectra data for PCA
Δ_{AB}	thickness dependence of X-ray absorption
Dy	dysprosium
E_L	laser energy
Er	erbium
Eu	europium
F	FARADAY constant; $F = 96\,485.3365\,\mathrm{C\,mol^{-1}}$
Fe	iron
F_L	laser repetition frequency
Ga	gallium
Gd	gadolinium
I_i	intensity of characteristic X-ray line of element i
$j_{O^{2-}}$	oxygen ion flow
k	surface exchange coefficient
$k_{A,B}$	sensitivity factor in CLIFF-LORIMER evaluation technique of X-ray intensities for elements A and B

La	lanthanum
λ	wavelength
L_c	characteristic length of a membrane
m	number of spectra for PCA algorithm
m	multiplicity; $m = 2j + 1$
n	number of depositions in the PLD process
n	number of channels in an EEL spectrum
n	number cubic perovskite atomic layers in the BCO phase
N	nitrogen
Nd	neodymium
$P_{O_2,d}$	oxygen partial pressure during deposition
$P_{O_2,c}$	oxygen partial pressure during cool down
R	gas constant; $R = 8.314\,4621\,\mathrm{J\,mol^{-1}\,K^{-1}}$
R_i	ion radius of atom i
O	oxygen
Pr	praseodymium
Sc	scandium
σ_{el}	electron conductivity
σ_{ion}	ion conductivity
Sm	samarium
Sr	strontium
t	sample thickness
Ta	tantalum
t_{tol}	GOLDSCHMIDT tolerance factor
t_{90}	time after which 90 % of a phase transition or separation of exponential character is completed
T	temperature
t_S	substrate temperature
u	relative atomic mass; $u = 1.660\,538\,921(73) \times 10^{-27}\,\mathrm{kg}$
Y	yttrium
Z	atomic mass
Zn	zinc
Zr	zirconium

Contents

1 Introduction

In modern material science there is an increasing need for materials with tailored physical and chemical properties. Therefore, material systems that can be modified on an atomic scale are of great interest. In the field of technical ceramics, advancements in the understanding of the perovskite crystal structure paved the way to a material system with numerous parameters that can be varied. The perovskite structure consists of two distinguished atomic sites (A- and B-type) which can be occupied by many different cations. This chemical flexibility influences specific properties like, e.g., electrical conductivity, ionic conductivity, electric susceptibility, physical- and chemical stability as well as high-temperature superconductivity [1].

Electron microscopy is an appropriate tool to investigate perovskite materials and is, therefore, used for the investigations in this work. Transmission Electron Microscopy (TEM) combines atomic-resolution imaging with electron diffraction for electron crystallography and advanced analytical techniques. Based on the combination of these techniques, different phases in the samples can be characterized in detail. Scanning Electron Microscopy (SEM) is a fast method for analyzing a large quantity of samples. Different phases can be distinguished on the basis of topography and determination of chemical composition.

Introduction of Mixed Electronic-Ionic Conductivity (MIEC) to the perovskite materials renders them appropriate for the use in oxygen separation membranes. The main motivation in this field is to achieve stable operation of a power plant combined with oxygen separation facilities for long-term periods at relatively low temperature (600-800 °C). $Ba_{0.5}Sr_{0.5}Co_{0.8}Fe_{0.2}O_{3-\delta}$ (BSCF) in the cubic perovskite phase is considered as promising membrane material because of its excellent oxygen ion conductivity in the desired temperature range. The limiting factor in the development of BSCF-based oxygen separation membranes, however, is the degradation of the membrane material as consequence of long-term operation at 600-800 °C. Within this work BSCF samples were studied by electron microscopic techniques to understand the fundamental processes which lead to the degradation of the separation performance. Furthermore, the thermodynamical stability of the cubic BSCF phase was improved by doping. Transition metals with fixed valence state such as Y and Zr were found to be suitable candidates for doping of BSCF.

Furthermore, surface coating of BSCF is studied to improve the performance of BSCF-based oxygen permeation membranes. In the course of the present study, doped and undoped epitaxial BSCF layers were prepared and coated with a nano-porous $La_xSr_{1-x}CoO_{3-\delta}$ (LSC) layer to improve the oxygen exchange rate and stability with regard to the formation of secondary phases at the surface.

As far as methodology is concerned, a new technique was introduced which allows to evaluate the valence state of Co in cubic BSCF and secondary phases. The technique is based on the determination of Co-$L_{2,3}$ white-lines in Electron Energy Loss Spectroscopy (EELS) data. The valence change of the Co-cation was discovered to be an essential process during secondary phase formation. Mapping of the Co-valence state at microscopic resolution provides a deeper understanding of the degradation of BSCF and facilitates the efforts on stabilization.

As the A- and B-site of the perovskite structure can be occupied by numerous different cations, not only oxygen conductivity, but also properties like magnetism and superconductivity can be tailored. The material system $CaCuO_2$ (CCO) can be considered as model system for cuprate-based superconductors. As the material was reported to be unstable under standard pressure conditions, the effort of this study was to stabilize CCO by epitaxial pressure introduced by a suitable substrate. As the material itself is not superconducting, the superconductivity has to be introduced by modifying the structure (charge carrier doping). In the group of Dr. D. Fuchs (Institute of Solid State Physics (IFP), Karlsruhe Institute of Technology (KIT)) charge carrier doping was studied by adequate termination of the substrate providing doping by a special pyramidal O-coordination at the interface layer.
The experience in the investigation of epitaxial BSCF films by electron microscopy was applied to characterize the interface and thermodynamical stability of $CaCuO_2$ (CCO) on $NdGaO_3$ (NGO) substrate. High-resolution TEM and Scanning Transmission Electron Microscopy (STEM) investigations were performed to investigate the substrate termination of NGO and the quality of the CCO growth. Combined with results from X-Ray Diffraction (XRD), Rutherford Backscattering Spectrometry (RBS) and low-temperature magnetic measurements, the structural reasons for the suppression of superconductivity were revealed.

The present work is composed of 4 main parts. In chapter 2 an overview of the material properties of BSCF is presented. The special electron microscopical methods used and developed for investigation are detailed in chapter 3. Furthermore, results of the investigation of both, BSCF bulk samples and thin-films, are reported and discussed in chapters 4.1 and 4.2. Different phases after annealing treatments were distinguished

and analyzed in detail to increase knowledge of the degradation process in BSCF.
In chapter 5 the work on the CCO-NGO interface is described. The mechanisms of the growth of CCO thin-films are described. The reasons why no superconductivity is found in the systems prepared in the course of the present study are investigated by TEM and discussed.

2 Fundamentals

The reduction of carbon dioxide emissions despite growing world-wide prosperity is one of the main tasks of our society. Science in the field of renewable energies achieved great progress in the recent decades. However, the lack of large-scale energy storage solutions forces us to still trust on fossil power plants. Carbon Capture and Storage (CCS) technology could act as intermediate step towards a completely sustainable energy supply. Key technology for CCS power plants is the cheap production of pure oxygen. Oxygen separation membranes [2–7] offer a solution for an energy saving and, therefore, cost effective O_2-supply. This work focuses on the structural properties and degradation mechanisms of $Ba_{0.5}Sr_{0.5}Co_{0.8}Fe_{0.2}O_{3-\delta}$ (BSCF) perovskite material, which has been identified as a promising material for oxygen separation membranes.
This chapter presents a review on the efforts of membrane development and contributes to the understanding of membrane degradation and sketches current achievements in performance improvement.

2.1 Working principle of oxygen separation membranes

The schematic function principle of an oxygen separation membrane is shown in Figure 2.1. The main part consists of a Mixed Ionic-Electronic Conductor (MIEC) material that transports O^{2-}-anions in direction of an oxygen concentration gradient. Charge equilibrium is established by electrons flowing in opposite direction. The oxygen concentration gradient $\frac{\partial c_0}{\partial x}$ is the driving force for oxygen separation and has to be established in a separation plant by either pumping the permeate site or using a sweep gas to remove the separation product.
The oxygen flow through the membrane is described by both, the oxygen diffusion coefficient D and the surface exchange coefficient k. The Onsager equation describes the dependence of the O^{2-}-anion flow $j_{O^{2-}}$ through the membrane surface (oxygen incorporation) for systems near the equilibrium [2].

$$j_{O^{2-}} = \frac{1}{2} k \cdot c_O \frac{\Delta \mu_O}{RT} \tag{2.1}$$

R is the gas constant, T the temperature, c_O the oxygen concentration in equilibrium and μ_O the chemical potential of oxygen.

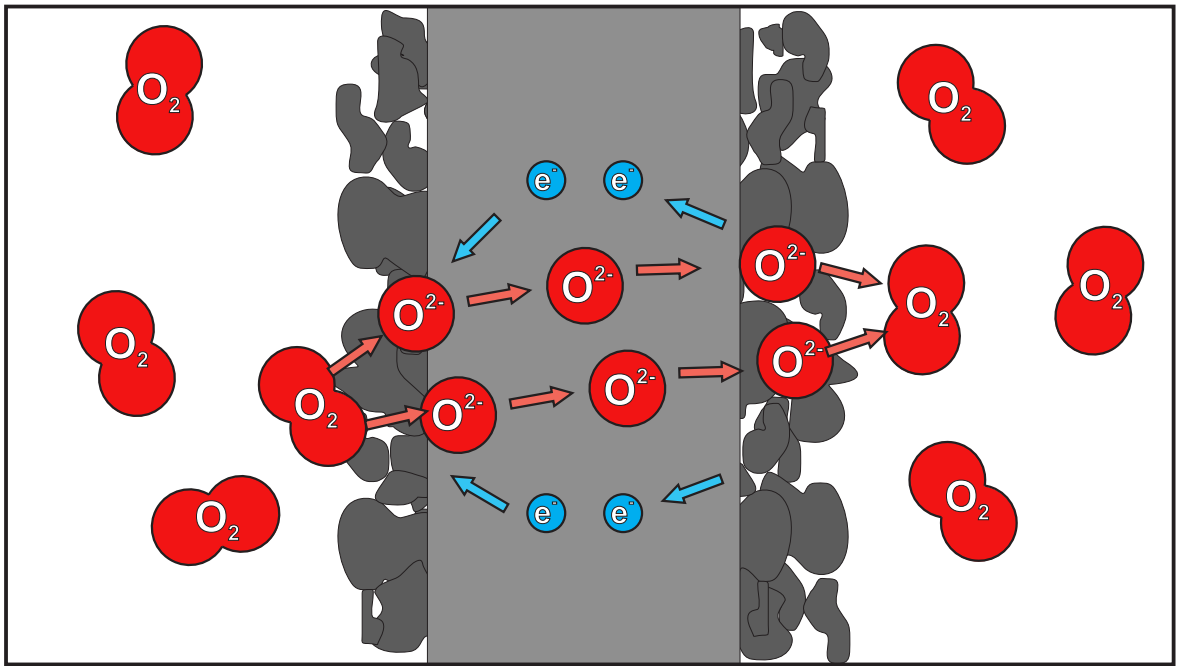

Figure 2.1: Function principle of an oxygen separation membrane. Oxygen is transported in direction of a partial pressure gradient. Charge balance is achieved by electron transport.

The O^{2-}-anion flow through the membrane material is determined by FICK's first law [2]:

$$j_{O^{2-}} = -D\frac{\partial c_0}{\partial x} \qquad \text{while} \qquad D = \frac{1}{8F^2}\frac{\sigma_{el}\cdot\sigma_{ion}}{\sigma_{el}+\sigma_{ion}}\frac{\partial \mu_O}{\partial c_O} \tag{2.2}$$

F is the FARADAY constant, while σ_i is the electronic or ionic conductivity, respectively. The fraction of k and D defines the characteristic length of the membrane L_c. The characteristic length L_c is an important measure for membrane design. For thicknesses smaller L_c, surface exchange becomes the limiting factor.

$$L_c = \frac{D}{k} \tag{2.3}$$

Typical values for L_c were determined to be in the range of 10^{-3}-10^{-9} m [2, p. 505]. For performance improvement, the membrane thickness has to be in the order of L_c within the restrictions of mechanical stability and gas tightness. A typical BSCF membrane thickness is in the order of 1 mm [8]. As detailed in Figure 2.1 the surface area may be enlarged by porous surface coatings to overcome performance bottlenecks generated by limited surface exchange. These coatings can either consist of the same material or a material with a higher surface exchange coefficient. Surface coating of membrane material was a subject of investigations in the course of the present work. The results are presented in section 4.2.3.

O^{2-}-conductivity through a perovskite crystal is described analogous to electron hole conductivity in a semiconductor. O^{2-}-anions are transported through the lattice via O^{2-}-vacancies which need to be present in a high, randomly distributed concentration for substantial O^{2-}-diffusion. The O^{2-}-vacancy concentration in the perovskite material depends on the temperature, the O_2 partial pressure and the valence of the cations. The fundamentals of mixed conducting materials are described in more detail in the review paper of Liu et al.[6].

2.2 Development of mixed ionic-electronic conductors

Mixed conductivity in calcia-stabilized zirconia was already described in 1982 by Cales and Baumard [9]. The material replaced stabilized zirconia in the following years as stabilized zirconia is not electrically conducting and was, therefore, dependent on external circuitry. A MIEC material with significant oxygen conductivity was described by Teraoka et al. [10, 11]. They varied the cation compositions in the system $La_xSr_{1-x}Co_yFe_{1-y}O_{3-\delta}$ (LSCF). BSCF was developed based on the experience with the LSCF system by exchange of La with Ba. Shao et al. [12] improved the performance and the stability of the cubic BSCF phase by variation of the cation ratio. The composition of $Ba_{0.5}Sr_{0.5}Co_{0.8}Fe_{0.2}O_{3-\delta}$ performs best in terms of both, oxygen conductivity and stability [12]. A detailed description of BSCF stability will be presented in the next section 2.3.

2.3 Thermodynamical stability of the BSCF system

To gain insight into the principles of the stability of BSCF, it is necessary to understand the perovskite structure at first. Figure 2.2 shows a rendering [13, 14] of an ideal cubic perovskite with the schematic formula of ABO_3.

Cubic perovskites crystallize in space group $Pm\bar{3}m$ and consist of two shifted cubic lattices. The first cubic lattice is occupied by the A-site cations (green) and the second by the B-site cations (blue). The O^{2-}-anions (red) describe an octahedron with the B-site in its center. The crystal structure of the perovskite depends on the ion radii R_i of oxygen anions and the cations (see Table 2.1). Goldschmidt introduced a tolerance factor t_{tol} providing an empirical measure for the distortion of a perovskite unit cell [15].

$$t_{tol} = \frac{1}{\sqrt{2}} \cdot \frac{R_A + R_O}{R_B + R_O} \tag{2.4}$$

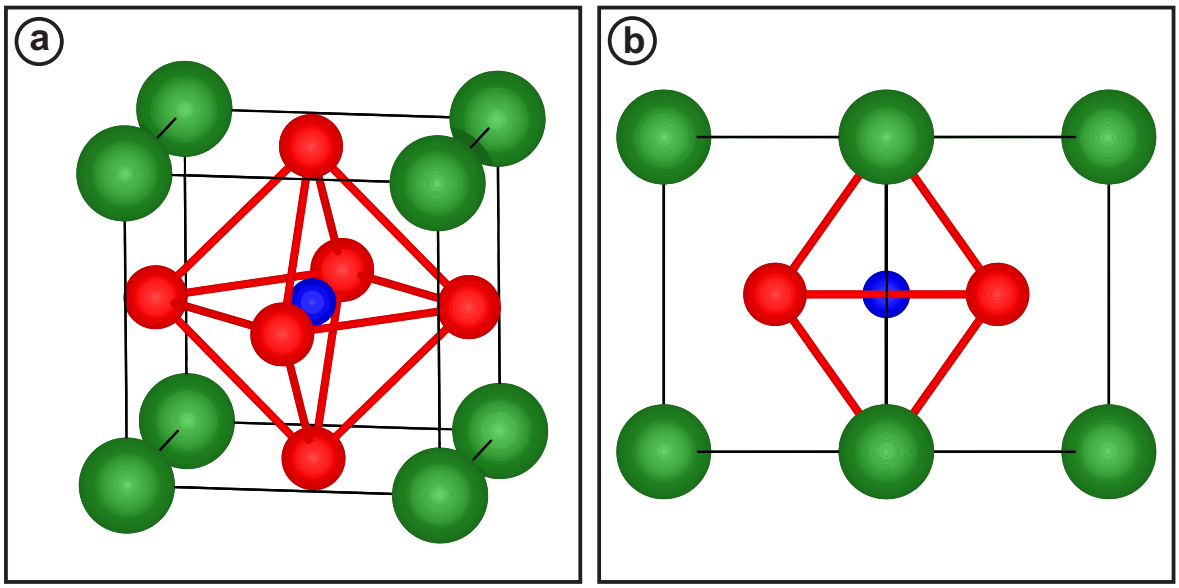

Figure 2.2: a) Elementary cell of an ideal cubic perovskite structure in [100]-zone axis and b) [101]-zone axis, with A-site cation positions in green, B-site cation positions in blue and O^{2-}-anions in red.

ion	radius [pm]
$^{XII}Ba^{2+}$	161
$^{XII}Sr^{2+}$	144
$^{VI}Co^{2+}$ (LS)	65
$^{VI}Co^{2+}$ (HS)	74.5
$^{VI}Co^{3+}$ (LS)	54.5
$^{VI}Co^{3+}$ (HS)	61
$^{VI}Co^{4+}$ (HS)	53
$^{VI}Fe^{2+}$ (LS)	61
$^{VI}Fe^{2+}$ (HS)	76
$^{VI}Fe^{3+}$ (LS)	55
$^{VI}Fe^{3+}$ (HS)	64.5
$^{VI}Zr^{4+}$	72
$^{VI}Y^{3+}$	90.0
$^{VI}Sc^{3+}$	74.5
$^{IV}O^{2-}$	138

Table 2.1: Ion radii in BSCF, taken from [16].

In principle, the equation is just the ratio of the perovskite lattice parameter calculated in two ways. It is assumed that the crystal consists of ions packed as dense spheres. For stable perovskites t_{tol} was determined to be between $0.78 < t_{tol} < 1.05$. The cubic perovskite structure is formed for values of $t_{tol} \approx 1$. Deviations lead to a crystallization in different symmetries. For values of $t_{tol} < 1$ rhombohedral symmetry is favored, for values of $t_{tol} > 1$ hexagonal symmetries are common. Depending on the material system further crystal systems may occur.
The ion radii for the elements contained in BSCF and investigated dopants (see chapter 2.4) are presented in Table 2.1. For A-site cations, a coordination of XII and for B-site cations, a coordination of VI was assumed according to the perovskite symmetry. Depending on the valence and spin state of the B-site cations, the tolerance factor of $Ba_{0.5}Sr_{0.5}Co_{0.8}Fe_{0.2}O_{3-\delta}$ varies between $0.97 < t_{tol} < 1.07$. The empirical model, therefore, predicts phase transformations in BSCF depending on the valence state of the B-site cations. As Co can change its ion radius in a broad range, phase instabilities are expected to stem from transitions of the Co cation into different oxidation states at elevated temperatures.
In recent years much effort was put on stabilization of the cubic BSCF material system. Starting from $SrCo_{1-x}Fe_xO_{3-\delta}$ (SCF) an additional A-site ion was added to prevent an ordering of O^{2-}-vacancies and, therefore, the transition into the orthorhombic brownmillerite structure [17]. An ordered structure of the oxygen vacancies is reported to decrease the oxygen conductivity significantly [2]. Ba was selected among multiple alternatives like (La, Pr, Sm, Nd, Er, Eu, Gd and Dy) because of the excellent oxygen conductivity at lower temperatures in the resulting materials [12, 18]. Fe on the B-site is important to keep the cubic structure, as BSC was reported to crystallize in a rhombohedral structure [19].
The composition of $Ba_{0.5}Sr_{0.5}Co_{0.8}Fe_{0.2}O_{3-\delta}$ (BSCF) is a compromise between stability (low Ba, high Sr content) and performance (high Ba, low Sr content) [20, 21]. At the beginning of BSCF research it was believed to be purely cubic in the desired application temperature range of 600-1000 °C. After more detailed studies, the stability range of BSCF was narrowed down, as more and more phase transitions were reported. Švarcová et al. reported a hexagonal phase in $Ba_{0.5}Sr_{0.5}Co_{0.8}Fe_{0.2}O_{3-\delta}$ [22], a result which was reproduced by further groups [23, 24] and in the course of the present study. The degradation into a hexagonal phase is caused by the significant electrostatic charge imbalance which was introduced into the system to generate high O^{2-}-conductivity. As described by Zeng et al. [17] who refer to [25] the charge can be balanced as desired by a temperature dependent formation of O^{2-}-vacancies. However, the valence state of Fe and especially Co can also change from 2+ to 3+. As the ion radii are dependent on the valence state this leads to an instability of the system and, therefore, to phase transformation.

The valence state of B-site cations in BSCF was investigated by several groups. While the valence state of Fe was demonstrated to be stable at 3+ [26, 27], it was reported that Co can change its valence state in the application-relevant temperature range. Arnold et al. [28] determined the Co-valence state for cubic BSCF in dependence of the temperature by in-situ TEM using an electrical heating holder. They measured the energy of the intensity maximum of the Co-L_3 white-line which was compared to values of reference materials. The Co-valence of BSCF changes from 2.6+ at room temperature to 2.3+ at 250 °C to 2.2+ at 500 °C. Efimov et al. [24] detected an increase of the Co-valence in secondary phases by the same method which was confirmed by calculations [29, 30]. According to Arnold et al. [28] the Co-valence of the hexagonal phase is expected to be significantly higher than 2.3+. The hexagonal phase is reported [31] to share a volume fraction of 50 % at temperatures of 800 °C and below where an increase of the Co-valence was reported. The Co-valence of BSCF at temperatures between room temperature and 800 °C was measured by Harvey et al. [26, 32] applying X-ray Absorption Spectroscopy (XAS) to analyze the fine structure of the Co-K edge. They observe a predominant oxidation state of 3+ for the Co-cation. A connection of the increased Co-valence to the hexagonal phase, which was also detected in their study, can be deduced from these results. However, despite all efforts, only indirect estimates of the Co-valence of the hexagonal BSCF phase were published up to now.
Inspired by these studies, a new EELS-based evaluation method was developed to gain insight into the Co-valence state in different secondary phases of BSCF (see section 3.8). According to the current knowledge of the degradation of the BSCF system this technique directly allows to image the process responsible for the instability of BSCF. The results of these studies are reported in section 4.1.8.
Yáng et al. gave a review on the phases in the BSCF system [33] including a first schematic phase map (Figure 4.26). It is notable that all end members of the BSCF system ($BaCoO_{3-\delta}$, $BaFeO_{3-\delta}$, $SrCoO_{3-\delta}$, $SrFeO_{3-\delta}$) do not crystallize in cubic symmetry. BSCF, therefore, occupies a stability island in the phase map. Niedrig et al. [34] pinpointed the transition to the hexagonal phase to the temperature range between 825 °C and 840 °C. However, the results of the previously mentioned groups are mostly based on integral neutron or X-ray diffraction investigations. This work extends the knowledge of the degradation of BSCF by intense electron microscopical studies. The results of these studies including the detailed analysis of recently discovered secondary phases in the BSCF system will be reported in section 4.

2.4 Improvement of BSCF performance

As described in section 2.3, BSCF degradation is mainly driven by the valence change of the B-site cations and the associated change of the ion radius. Therefore, the introduction of additional cations, especially on the B-site is a very promising approach for stabilization of the system. As Fe-based MIEC are reported to be more stable [35], the main effort was set on Co reduction in the membranes. Feldhoff et al. and Martynczuk et al. investigated Co-free oxygen separation membranes. They exchanged Co by Zn [36–39], Al [40] or Cu [41]. Although neither a complete stabilization nor a performance advantage in short-term permeation experiments was achieved, the long-term performance in the intermediate temperature range was improved. Meng et al. reported on $Ba_{0.5}Sr_{0.5}(Co_{0.6}Zr_{0.2})Fe_{0.2}O_{3-\delta}$ (BSCZF) material, where a significant reduction of Co by the introduction of Zr resulted in increased stability [42]. Yakovlev et al. investigated the system $Ba_{0.5}Sr_{0.5}(Co_{0.8}Fe_{0.2})_{1-x}Zr_xO_{3-\delta}$ (BSCFZ) for x=0, 0.01, 0.03, 0.05, and 0.10 [43]. They report on a stabilization of the cubic perovskite phase beside a high oxygen conductivity for x=0.03. Doping with Y of the system $Ba_{0.5}Sr_{0.5}(Co_{0.8}Fe_{0.2})_{1-x}Y_xO_{3-\delta}$ (BSCFY) with x=0-0.2 also leads to a stabilization of the cubic perovskite phase. Haworth et al. [44, 45] also discovered a significant performance improvement with its peak for x=0.025. According to the authors, the operation temperature of a BSCFY membrane can be decreased by 70 °C in comparison to pure BSCF, without performance reduction. Nevertheless, the transition to the hexagonal phase cannot be suppressed by doping with Y.
In this work three different dopants with fixed valence state (Table 2.1) were investigated. The dopant substitutes the B-site according to the chemical formula $Ba_{0.5}Sr_{0.5}(Co_{0.8}Fe_{0.2})_{0.97}X_{0.03}O_{3-\delta}$ (BSCF3X), where X stands for Sc, Y and Zr. The main aim of the current work is to investigate the microstructural changes caused by doping and the effect on material performance. The results will be reported in section 4.1.6 and discussed in section 4.3.5.

2.5 Massive samples vs. thin-films

Two types of samples were analyzed in the course of this work. Samples prepared from massive material (about 10 x 5 x 5 mm) were used to investigate the stability of volume material without influence of surface effects (see section 4.1). This step is necessary to understand the complex processes in the material as it consists of multiple different cations. Epitaxial thin-film samples (thickness $\approx$ 100 nm) (section 4.2) were prepared and analyzed to investigate BSCF as thin membrane material. In addition to the degradation processes discussed for volume material, further stabilizing and destabilizing effects are expected. On the one hand, the epitaxial pressure introduced

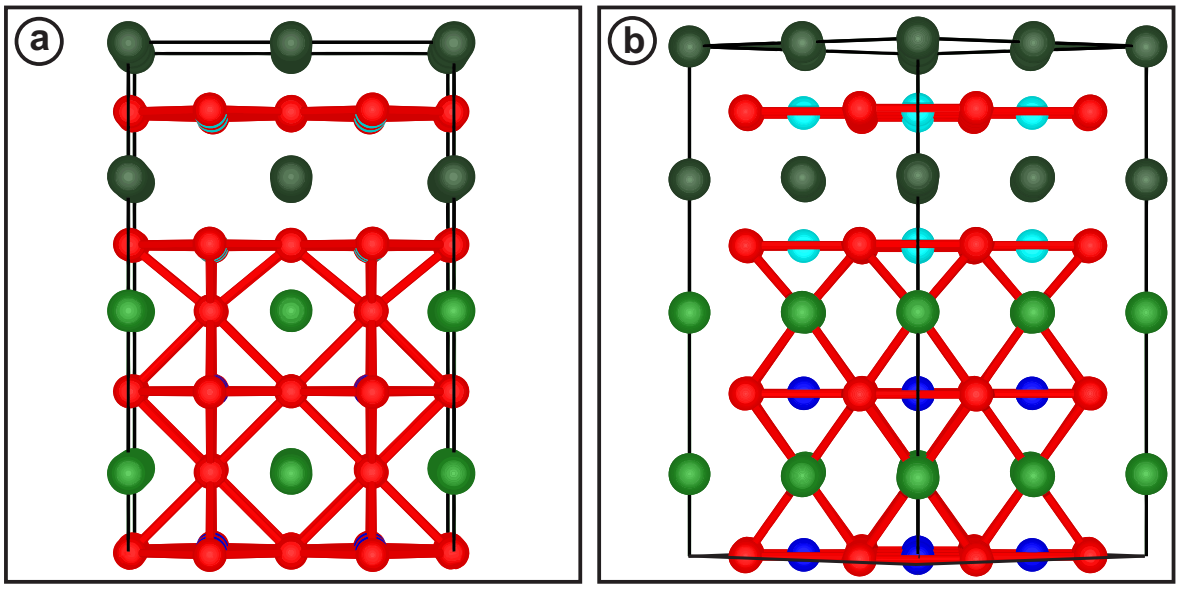

Figure 2.3: Structure models of the CCO-NGO interface in a) [100] pseudo cubic zone axis and b) [110] pseudo cubic zone axis. The atomic sites are colored: Nd (green), Ga (blue), O (red), Ca (dark green) and Cu (pale blue).

by a suitable substrate material may stabilize the cubic phase of thin BSCF films. On the other hand, the surface of the thin-film is exposed to CO_2 which was reported to poison the membrane surface by carbonate formation [46–48]. Unfortunately many potential applications of oxygen separation membranes require stability under high CO_2 partial pressures. To overcome this limitation, thin-films with coatings were prepared to improve the oxygen conductivity in CO_2-containing atmospheres. LSC is a promising material system for this purpose as it shows good oxygen conductivity and no surface poisoning in CO_2 containing atmospheres [49, 50]. Furthermore, secondary Co_3O_4 phases, reported to form at LSC surfaces [51], are discussed to even improve the oxygen surface exchange rate [52].

2.6 The interface $CaCuO_2$–$NdGaO_3$

Beside the interest in perovskites due to their MIEC properties, other perovskites are investigated due to superconductivity. Thin perovskite films deposited on suitable substrates are discussed as 2-dimensional superconductors. Such a material is of great experimental and theoretical interest.

$CaCuO_2$ (CCO) is a prototype system for cuprate-based high-temperature superconductors like $YBa_2Co_3O_{7-x}$. CCO itself is not superconducting. However, superconductivity may be introduced by modifying the coordination of the Cu-atoms in the lattice. This process is called charge carrier doping. Doping can be achieved by additional cations providing a charge carrier reservoir or by a special pyramidal or octahedral

O-coordination of the Cu-cations. The essential O-atom at the apex of the circumscribed pyramid (octahedron) is called apex oxygen. This coordination was reported to be an essential characteristic for many different types of cuprate-based superconductors [53]. For CCO, the pyramidal apex O-coordination can be artificially introduced to the structure at the interface with a suitable substrate material. In this case, a 2-dimensional superconducting layer is generated.

As CCO was reported to be unstable under standard atmosphere conditions [54], the material has to be stabilized. The stabilization can be achieved by adding 10 % of Sr to the A-site [55]. However, the superconducting properties are negatively affected by the Sr-substitution. Stabilization of thin-films can also be achieved by the epitaxial pressure introduced by the growth on an appropriate substrate.

The system $ACuO_2$ (with A= Ca, Sr, Ba) was investigated in detail since the synthesis under ambient pressure was realized by Siegrist et al. [56]. $ACuO_2$ crystallizes in the tetragonal structure (P4/mmm) and can be described as an alternating stacking of planes of A and CuO_2 [56]. These CuO_2 planes are believed to be essential for cuprate-based superconductors with high critical temperature [57], as they can be doped by apex oxygen.

The investigation in this work was concentrated on $CaCuO_2$ (CCO) because the ion radius of Ca stabilizes the 2D CuO_2 planes best and prevents the formation of 1D CuO chains which occur for example for A= Sr [58]. Furthermore, this study especially focuses on an interface structure between CCO and a perovskite substrate, as only this interface can be doped by the substrate to form a 2D-superconductor.

The substrate has to be chosen carefully to assure the required A-site termination providing the apex O-anion. Among the possible substrates $SrTiO_3$ (STO), $LaAlO_3$ (LAO), $(LaAlO_3)_{0.3}(Sr_2AlTaO_6)_{0.7}$ (LSAT) and $NdGaO_3$ (NGO), only NGO can be stabilized embracing a single A-site termination [59]. The other substrates show mixed or B-site termination [60].

In Figure 2.3 the system is shown in a) [100]- and b) [110]-zone axis orientation with the epitaxial CCO layer on top. The O-anions are colored in red. The cations are depicted in green (Nd), blue (Ga), dark green (Ca) and pale blue (Cu). The $NdGaO_3$ (NGO) substrate material is usually not reported to crystallize in perovskite structure but in orthorhombic symmetry. However, in [110]-zone axis orientation, the pseudo cubic lattice parameter of $a \approx 0.386\,\text{nm}$ almost agrees with the lattice parameter of CCO (a=0.3855 nm) and, therefore, generates an appropriate epitaxial pressure to stabilize the CCO thin-film. As shown in Figure 2.3, the NGO substrate also comprises perovskite like stacking of AO and BO_2 layers in [001]-direction. Furthermore, Figure 2.3 demonstrates that for A-site termination of the substrate, the Cu-cations are located in the pyramidal O-coordination with the apex O-anion provided by the NGO substrate. As this coordination may hole-dope the CuO_2 plane at the interface, the potential su-

perconductivity in the system is expected to be confined to the direct vicinity of the interface, as demonstrated for CCO on STO [61].
The growth of perfect CCO layers on perovskite substrates was examined by different groups [62–65] with insufficient success, most likely because of the intrinsic chemical instability of CCO; a problem which this study aims to overcome by the epitaxial pressure introduced by the NGO substrate. Furthermore, no superconductivity of the system was reported yet (publication of SCHÖN et al. [66] was retracted due to scientific misconduct).

To understand the electronic properties of the CCO-NGO interface, TEM was applied to confirm the epitaxial growth of CCO and to specifically assign the superconducting behavior to the pyramidal coordinated CuO_2 planes, since superconductivity in the system also may arise from the presence of defect layers [67] or impurity phases [68, 69].
The absence of superconductivity may also occur due to imperfections of the growth. The TEM analysis was conducted also to focus on sample quality and to shed more light on the reasons for imperfect layer growth. The TEM investigations were accompanied by detailed XRD analyses, resistivity measurements, Atomic Force Microscopy (AFM) measurements and analyses with a Superconducting QUantum Interference Device (SQUID), published in [70].

3 Electron microscopy and methodological developments

Electron microscopy comprises numerous different techniques of imaging, diffraction and spectroscopy. A broad overview on Transmission Electron Microscopy (TEM) techniques is explained, for instance in, the textbook by Williams and Carter [71]. Scanning Electron Microscopy (SEM) is explained, for example, in the textbook by Reimer [72]. In the following a short overview will be presented on the techniques which were mainly used in this work. Special analytical techniques were developed and applied for the post-processing of Energy-Dispersive X-ray Spectroscopy (EDXS) and Electron Energy Loss Spectroscopy (EELS) measurements. The analyses of EDX spectra by the standard-based Cliff-Lorimer technique is explained in section 3.7. A new evaluation technique for the determination of Co-valence states from EEL spectra was developed in the course of this work and is described in sections 3.6 and 3.8.

3.1 Instrumentation for electron microscopy

SEM investigations were conducted using both, an LEO 1530 microscope (now: Carl Zeiss NTS GmbH, Oberkochen, Germany) equipped with an Field-Emission Gun (FEG) and a GEMINI® column, and an FEI environmental SEM Quanta 650 (FEI company, Hillsboro, Oregon, USA) also featuring a FEG.
TEM studies were performed utilizing a Philips CM200 FEG/ST microscope (now: FEI company) equipped with a FEG and a 4 k x 4 k TemCam-F416 CMOS camera from TVIPS (Tietz Video and Imaging Processing Systems GmbH, Munich, Germany) operated at 200 kV. Electron diffraction investigations were performed on an LEO 922 (now: Carl Zeiss NTS GmbH) transmission electron microscope featuring an in-column energy filter operated at 200 kV. Diffraction patterns were recorded on imaging plates from DITABIS (Digital Biomedical Imaging Systems AG, Pforzheim, Germany). Analytical TEM and STEM analyses were performed with an aberration-corrected FEI Titan^3 80-300 (FEI company) microscope operated at 300 kV. The machine is equipped with a FEG, a 30 mm^2 EDAX Si(Li) X-ray detector with an ultra-thin window and an energy resolution of 136 eV (EDAX Inc., Mahwah, New Jersey, USA) for EDXS. Furthermore, a post-column Tridiem 865 HR Gatan Imaging Filter (GIF) (Gatan Inc., Pleasanton, California, USA) with an energy resolution of 0.7 eV and a total channel

count of 2048 is attached. The GIF was operated at a dispersion of 0.05 eV/channel. Simulations of diffraction patterns were done with the software package Java Electron Microscopy Simulations (JEMS) version 3.6322U2011 by Stadelmann [73].

3.2 Sample preparation

Samples of bulk BSCF material for SEM were polished using diamond lapping films and were subsequently chemically etched using colloidal silicon dioxide solution (Oberflächentechnologien D. Ziesmer, Kempen, Germany) to generate contrast due to surface topography. The chemical solution was dispersed on a polishing cloth followed by polishing for 1-3 min. TEM sample preparation was performed by conventional methods including grinding using diamond lapping films, dimple grinding and polishing. Ar^+-ion etching was applied as final thinning step on a Precision Ion Polishing System (PIPS) (Gatan Inc.), a DuoMill (Gatan Inc.), or a IV3 Ion Mill (Technoorg-Linda Ltd. Co., Budapest, Hungary). For electron diffraction, samples in distinct zone-axis orientation were prepared using an FEI Strata 400S (FEI company) Focused Ion Beam (FIB) system following the process described by Ayache et al. [74].

3.3 Fast mapping of phases in BSCF

The investigation of BSCF degradation depending on annealing time and temperature results in a large set of different samples that have to be investigated with regard to their microstructure and phase composition. As a TEM study is a time-consuming task, a method for faster phase determination by SEM was developed and applied in the course of this work. Samples of BSCF bulk material were prepared for SEM by the techniques described in section 3.2. Figure 3.1a) shows a scheme how selective etching of different phases by colloidal silicon causes a distinct topography of the sample surface. This topography can be imaged with high contrast and resolution using the in-lens detector (Secondary Electrons (SE) dominated contrast) of the GEMINI® column. Figure 3.1b) shows a typical SEM micrograph of a sample prepared as described. As typical SE and Back Scattered Electrons (BSE) SEM images do not contain electron crystallographic information, TEM studies have to be performed in addition to assign the areas of different contrast to crystallographic phases.

To link different phases that were determined by electron diffraction in the transmission electron microscope to SEM images, chemical composition analyses by EDXS were performed in both microscope types. The assignment of individual phases is therefore only correct if one assumes that all different phases have a distinctive chemical composition. However, these assumptions were appropriate for all phases that

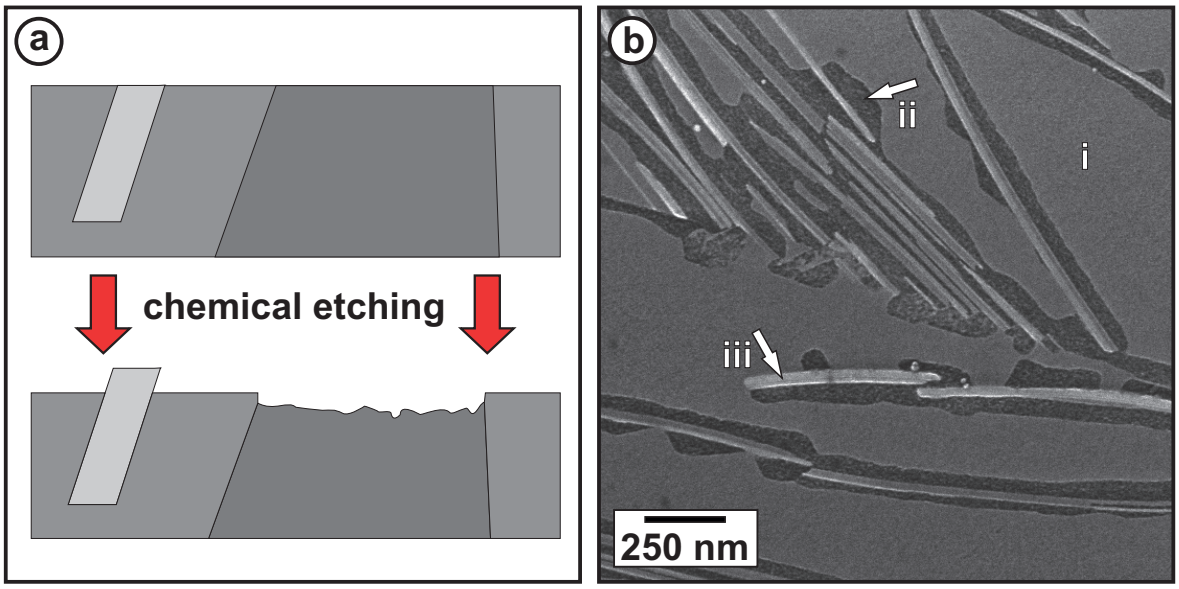

Figure 3.1: a) Phase-depending topography of BSCF samples introduced by chemical etching; b) typical SEM SE in-lens image showing different contrasts. The different regions (i)-(iii) cannot be be assigned to crystallographic phases directly. TEM investigations have to be supplemented.

were determined in the BSCF system in the course of this work. The determination of the crystal structure by TEM was performed using different electron diffraction techniques. Selected-Area Electron Diffraction (SAED) patterns of different zone-axes were recorded for large grains ($> 100\,\mathrm{nm}$) to determine their crystal structure and was therefore mostly used to detect the large grains of the cubic perovskite phase. Accompanying to electron diffraction, simulations of diffraction patterns of the cubic perovskite BSCF phase were calculated using the JEMS software [73] and the crystallographic data from Koster and Mertins [75]. Convergent-Beam Electron Diffraction (CBED) was used to collect diffraction data from smaller crystallites. This particular diffraction technique and the involved data evaluation is described in section 3.5. Fourier-analysis of High-Resolution Transmission Electron Microscopy (HRTEM) images and JEMS simulations were applied to determine the crystal structure of very small sample regions. Based on these investigations the light gray regions (i) in Figure 3.1b) can be assigned to the cubic perovskite phase, while the darker regions (ii) correspond to a secondary hexagonal phase with different chemical composition. The brighter, plate-like regions (iii) consist of thin lamellae of cubic, hexagonal and a newly assigned $Ba_{n+1}Co_nO_{3n+3}(Co_8O_8)$ (BCO)-type phase which is described more closely in sections 4.1.2-4.1.4.

3.4 Scanning Transmission Electron Microscopy (STEM)

Scanning Transmission Electron Microscopy (STEM) is a serial acquisition technique which can be implemented in transmission electron microscopes. A small electron probe is generated by the condenser system and is scanned by two pairs of deflection coils located above the sample. Below the sample, further image formation optics is not required. Elastic and inelastic scattering of the incoming electron beam results in an angular distribution of the electrons below the sample. Inelastic scattering can give rise to the generation of characteristic X-rays which are detected by a detector mounted above the sample at an inclination of 14.6 ° (FEI Titan^3 80-300). Energy loss of the electrons by inelastic scattering can be investigated by an energy filter mounted below the sample plane. Usually, a large set of different detectors is available yielding both bright- and dark-field images and analytical information simultaneously. The serial character of the image acquisition allows the assignment of the spectroscopic information to a distinct sample region. Chemical analysis by EDXS (see chapter 3.7) and investigation of the oxidation states by EELS (see chapter 3.8) with a lateral resolution only limited by the probe diameter, the distance between two individual measuring points and the sample thickness can be achieved.

High-Angle Annular Dark-Field (HAADF) STEM is a special scanning imaging technique which was pioneered by Crewe et al. [76, 77]. Wall et al. discussed an annular dark-field detector first [78]. An annular detector is introduced at a definable camera length below the sample. A hole in the middle of the detector assures that only electrons scattered into large angles hit the detector. The signal measured by the detector therefore strongly depends on the atomic number Z and the thickness of the sample. As rough approximation one can assume a Z^2 dependence due to the same dependence for Rutherford scattering. Crewe [79] proposed a $Z^{3/2}$ dependence. For samples with constant thickness and density, regions with brighter image intensity therefore can be assigned to heavier elements unambiguously. The "distance" of the detector relative to the sample can be controlled virtually by different excitation of the electron lenses between sample and detector. This allows balancing intense material contrast (short distances) with high count rates and good Signal-to-Noise Ratio (SNR) (large distances). Further information on STEM is presented, for instance, in the textbook by Williams and Carter [71].

High resolution HAADF STEM imaging was often applied in this work because of the easily interpretable image contrast compared to HRTEM. It was pioneered in the late 1980ies by Shin, Kirkland and Silcox [80] and is the consequent further development of (HAADF) STEM. In modern microscopes atomic resolution can be achieved

for thin samples oriented along a highly symmetric zone axis. Due to the significant dependence of the detector signal on Z, bright spots can be directly assigned to atomic columns without interpretation and simulation of interference pattern as necessary for HRTEM. Brighter columns either consist of heavier atoms or a more dense stacking of atoms. The significant Z dependence can be used to determine the chemical composition with atomic resolution in a crystal lattice. For the perovskite structure investigated in the present study, A- and B-site cations can easily distinguished by their different atomic number. For thin samples the resolution is limited by the probe size. In practice, the broadening of the probe due to multiple scattering in the sample is the limiting factor. Multiple scattering is reduced for thin samples. The minimum thickness of the perovskite samples prepared in the course of this study was limited due to amorphization.
In recent studies [81] a difference of ΔZ=3 was resolved by comparison of the image intensities with standard samples. HAADF STEM is therefore a powerful technique for the investigation of secondary phases in perovskites, which requires structural investigation on atomic level and the determination of the chemical composition and oxidation state. A historic roundup of all aspects of (HAADF) STEM is given by Pennycook [82].

3.5 Convergent-Beam Electron Diffraction (CBED)

Convergent-Beam Electron Diffraction (CBED) is an advanced diffraction technique in TEM. It offers information on, e.g. the precise electron high tension, sample thickness and crystal structure. In this work the main focus was set on the determination of the crystal structure. For the other CBED applications the reader might refer to the textbook of Williams and Carter[71].
For CBED, a convergent electron probe is formed in the condenser lens system of the microscope. In contrast to SAED, the size of the sample region under investigation is not limited by the diameter of the selected-area aperture but by the spot size of the convergent electron beam. As detailed in Figure 3.2a), this illumination not only enables for a high spatial resolution, but also allows determination of the full point and space group of a distinct crystallite. The convergent illumination can be described as a superposition of incoming electrons with different incident angles. The interaction of the electrons with the sample therefore has to be described by a superposition of differently tilted Ewald spheres. For this reason, the Higher Order Laue-Zones (HOLZ) are cut by the Ewald sphere at a position closer to the center of the illumination (see Figure 3.2a)). As the 3-dimensional information of the crystal structure is contained in the electrons diffracted from the HOLZ (outer part of the CBED pattern in Figure

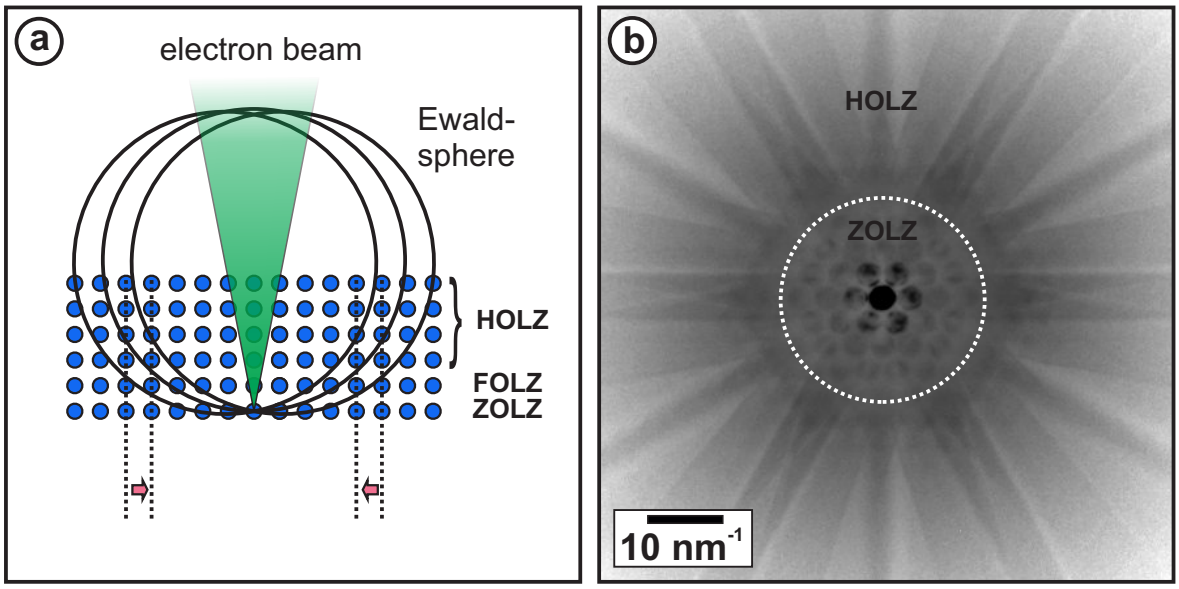

Figure 3.2: a) Effect of convergent illumination on the information in the diffraction image. The tilted components of the incident beam correspond to tilted EWALD spheres which cut the HOLZ closer to the center. b) CBED pattern of a hexagonal crystallite oriented in [0001]-zone axis.

3.2b)), a CBED pattern contains the full symmetry and lattice parameters of the crystal structure under investigation.
The CBED patterns were evaluated applying the method described by MORNIROLI and STEEDS [83]. It is based on the work of BUXTON et al. [84]. The determination of the crystal structure is a two-step process:

- The 2-dimensional symmetry of the Zero Order LAUE-Zone (ZOLZ) is determined (inner part of Figure 3.2b)). This information can be obtained either from an SAED pattern or from the ZOLZ reflections in a CBED pattern.

- The full 3-dimensional symmetry of a CBED pattern is determined. This is a very difficult step which requires a CBED pattern of an exactly oriented crystallite containing HOLZ reflections (outer part of Figure 3.2b)).

Ten different symmetries (plane point groups) can be distinguished in this notation: 1, 2, 3, 4, 6, m, 2mm, 3m, 4mm and 6mm. The number gives the amount of rotation operations within a full rotation which lead to an indistinguishable pattern. m (mm) describes one (or two) independent mirror plane symmetries. To improve accuracy of the symmetry determination, the sample can be tilted in direction of the mirror-planes to check whether the symmetry holds in the HOLZ.
According to Table 3.1 which was taken from [83] one can then determine the diffraction class of a diffraction pattern. The diffraction class is connected to the crystal point group as listed in Table 3.2 taken from [84]. As both assignments in most cases are

diffraction class	2D-symmetry	3D-symmetry
1, 1_R	1	1
2, 21_R	2	2
2_R	2	1
m_R	m	1
m, $m1_R$	m	m
$2m_Rm_R$	2mm	2
2mm, $2mm1_R$	2mm	2mm
2_Rmm_R	2mm	m
4, 41_R	4	4
4_R	4	2
$4m_Rm_R$	4mm	4
4mm, $4mm1_R$	4mm	4mm
4_Rmm_R	4mm	2mm
3, 31_R	3	3
$3m_R$	3m	3
3m, $3m1_R$	3m	3m
6, 61_R	6	6
6_R	6	3
$6m_Rm_R$, $6mm1_R$	6mm	6
6mm	6mm	6mm
6_Rmm_R	6mm	3m

Table 3.1: Diffraction class as function of 2D- and 3D-symmetry of the diffraction pattern, taken from [83].

	1	1_R	2	2_R	21_R	m_R	m	$m1_R$	$2m_Rm_R$	2mm	2_Rmm_R	$2mm1_R$	4	4_R	41_R	$4m_Rm_R$	4mm	4_Rmm_R	$4mm1_R$	3	$3m_R$	6	6_R	3m	6_Rmm_R	31_R	61_R	$6m_Rm_R$	6mm	$3m1_R$	$6mm1_R$
1	X																														
$\bar{1}$				X																											
2	X		X			X																									
m	X	X					X																								
2/m				X	X						X																				
222	X					X			X																						
mm2	X					X	X	X		X																					
mmm				X		X					X	X																			
4	X					X							X																		
$\bar{4}$	X					X								X																	
4/m				X							X				X																
422	X					X			X							X															
4mm	X					X	X	X									X														
$\bar{4}2m$	X					X	X	X	X									X													
4/mmm				X							X	X							X												
3	X																			X											
$\bar{3}$				X																		X									
32	X		X			X															X										
3m	X	X					X																	X							
$\bar{3}m$				X	X						X														X						
6	X					X																X				X					
$\bar{6}m$	X						X																				X				
6/m				X							X																	X			
622	X					X			X																				X		
6mm	X					X	X	X																						X	
$\bar{6}m2$	X					X	X	X			X																				X
6/mmm				X		X					X	X																			X
23	X					X			X											X											
m3				X		X						X											X								
432	X					X			X							X						X									
$\bar{4}3m$	X					X		X										X			X										
m3m				X					X			X				X			X					X							

Table 3.2: Diffraction point group as function of diffraction class [84].

ambiguous, different zone axes of each phase have to be investigated. To achieve a fast assignment involving the evaluation of as few as possible diffraction patterns, it is helpful to record diffraction patterns of the highest symmetrical zone axes which can be accessed by the goniometer. In case of the hexagonal symmetry, one can achieve an unambiguous assignment with only one CBED pattern of highest symmetry. For a known crystal structure this method can also be used to determine the zone axis [83].

3.6 Spectra processing by Principal Component Analysis (PCA)

The evaluation of EELS and EDXS data with low SNR requires elaborate spectra post-processing. Spectra with a low SNR result from short acquisition times like they occur in linescans and mappings, as the maximum measurement time is limited to about 10 h due to sample drift.
A noise-elimination algorithm involving Principal Component Analysis (PCA) [85, 86] was applied in the present study. Datasets from mappings and linescans represent a perfect application of the PCA algorithm as it requires a large set of similar spectra for a reliable, artifact-free noise reduction.
The algorithm is an orthogonal transformation. In this context each spectrum can be considered as vector which linearly depends on the other vectors. For the mathematic realization of the algorithm the data is considered as a matrix $D = m \times n$ with the number of spectra m and the number of channels per spectra n. The algorithm is a change of basis of D. The first essential step of the algorithm is the calculation of a normalized matrix $\bar{D}$ according to the equation:

$$\bar{D}_{ij} = D_{ij} - \sum_{l=1}^{n} \frac{D_{il}}{n} \tag{3.1}$$

By identifying the basic, uncorrelated vectors (principal components) one can create a new basis of the multidimensional dataset. In a second step, the vectors (raw-data spectra) are projected to the new orthogonal basis. By limiting the number of principle components to a set of the most relevant components (components with high variance), the back-projection results in a reduction of dimensions of the dataset and therefore a decrease of complexity.

PCA was applied to reduce noise in qualitative EDXS mappings. Figure 3.3 gives a comparison between an unfiltered (gray curve) and PCA-filtered EDX spectrum (red and blue curves). The number of principal components involved in the back-projection was varied from 3 (red curve) to 10 (blue curve). Significant noise reduction is already

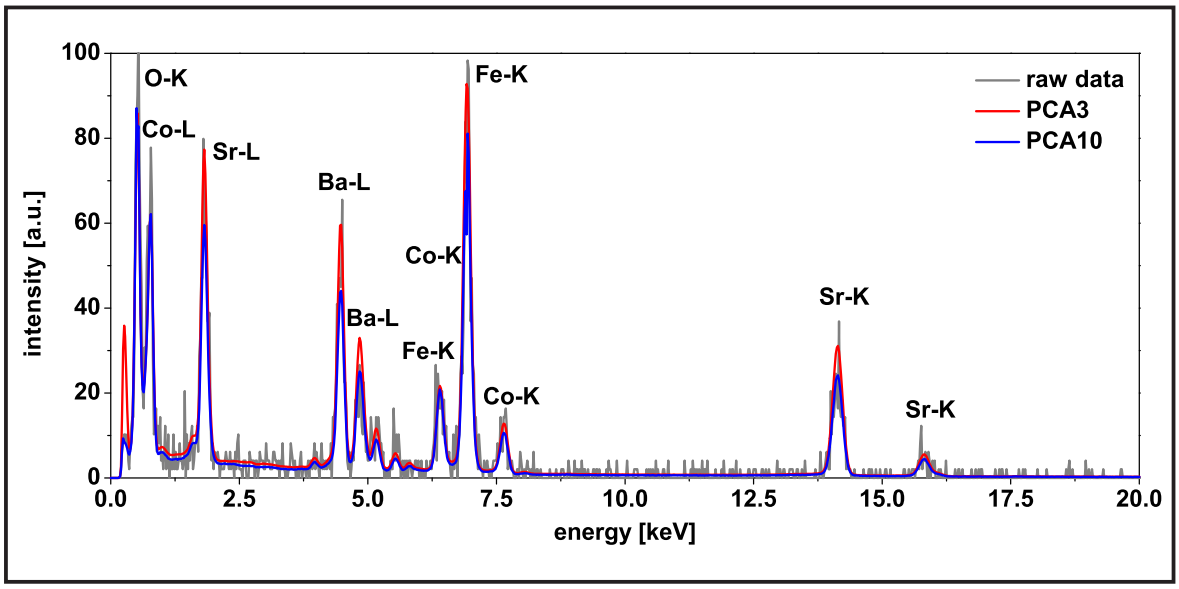

Figure 3.3: Effect of PCA-based noise reduction on EDX spectra. The gray curve represents the raw-data. The red curve was filtered by PCA using the first 3 principal components for back-projection, while the blue curve involved 10 principal components.

achieved for the red curve. PCA influences the data in a way that quantitative evaluation is not possible. Peak ratios might be changed if the SNR is small (compare the red and blue curve). Furthermore, the background of noisy data might be completely removed after back-transformation. This can be understood as it is interpreted as noise. The effect is demonstrated in Figure 3.3 in regions of high X-ray energy. By comprising a large amount of principal components into the back-projection, the artifacts of PCA are minimized. However the noise is less reduced. In the present work PCA was used to qualitatively illustrate composition changes in different chemical phases. Furthermore, it was used to verify the absence of trace elements (dopants) in BSCF. For noise reduction of EDX spectra, depending on the data, the first 2-15 principle components were employed to calculate the filtered spectrum.

PCA was also applied to EELS as essential step in the white-line distance-based evaluation of the Co-valence state (see section 3.8.2). Data with low SNR like in linescans or mappings was filtered for a reliable automatic detection of the Co white-lines. The spectrum post-processing involves several steps which are described in the following.

The PCA algorithm was implemented in a C++ program written by Meffert [87]. Automated processing of the whole data analysis is significantly improved by implementing the alignment of the spectra and peak fitting in the C++ program. Critical tasks like background subtraction and energy calibration are not necessary for the white-line distance determination.

In a first step, all spectra were aligned at the Ba-M_5 edge to compensate energy drift of the spectrometer during the acquisition time of the spectrum set of 5-10 h. In a

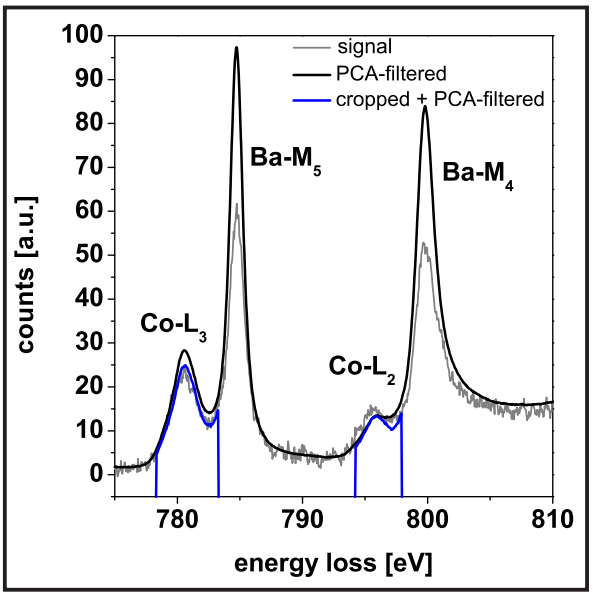

Figure 3.4: Effect of PCA-based noise reduction on EELS white-lines of a cubic BSCF region. The gray curve represents the original data. The black curve gives the filtered spectrum. The blue curve represents the PCA-filtered signal of cropped regions around the Co white-line which was used for data evaluation.

subsequent step the number of channels was increased by a factor of 4 to achieve a sub-channel accuracy for the peak position determination.

To illustrate the effect of PCA on a raw EEL spectrum (gray line in Figure 3.4), the whole spectrum was processed including a back-projection involving the first 15 principal components (Figure 3.4, black line). For automated data processing, the signal is cropped to the region around the Co-$L_{2,3}$ lines prior to PCA filtering to save computing time and to reduce the number of principal components required for a suitable description of the data. The PCA algorithm is then applied to the cropped signal (blue curve in Figure 3.4). The position of the maxima of the Co-$L_{2,3}$ white-lines are then automatically detected in the cropped and filtered spectra. The Co-$L_{2,3}$ line distance in Figure 3.4 amounts to 15.2 eV. For spectra with particularly low SNRs the exact peak position was determined by fitting a GAUSSIAN function employing the maximum of the signal as coarse start parameter for the fit.

As also discussed for the filtering of EDX spectra, Figure 3.4 illustrates that the Co-$L_{2,3}$ intensity ratio may be modified by the PCA. However, the distance between the lines is not affected which was tested by the evaluation of filtered and unfiltered spectra. PCA filtering is therefore applicable to EEL spectra in order to determine the white-line distance. It is not suitable for any evaluation based on the white-line ratio as the ratio might be influenced by the algorithm. As the cropped EEL spectra are very simple and do not change significantly overall the whole spectrum set, the first 2-3 principal components were used for back-projection.

3.7 Quantitative Energy-Dispersive X-ray analyses (EDXS)

The chemical composition of BSCF and secondary phases therein was determined by EDXS investigations. The current section describes the corresponding method for quantitative EDXS. For thin samples the Cliff-Lorimer ratio technique [88] can be used for quantitative analysis of the spectra, where:

$$\frac{C_A}{C_B} = k_{A,B}\frac{I_A}{I_B} \qquad \text{while} \qquad \sum_i C_i = 100\% \tag{3.2}$$

and C_i is the concentration of element i in the sample, I_i the peak intensity of the chosen characteristic X-ray line of element i. The Cliff-Lorimer equation therefore converts the measured integrated X-ray intensity ratio for elements A and B within the analyzed volume into an atomic fraction. The $k_{A,B}$ factor, also called sensitivity factor, depends on the measurement setup, the pair of elements under investigation, and the characteristic X-ray lines employed for analysis. EDXS evaluation software like the FEI TEM Imaging and Analysis (TIA) suite (version 4.3 build 904) has a database of $k_{A,Si}$ factors included for quantitative investigation. This database can be utilized to calculate the factors for any combination of elements, i.e.:

$$k_{A,B} = \frac{k_{A,C}}{k_{B,C}}. \tag{3.3}$$

To improve the accuracy of quantitative analyses, element-specific Cliff-Lorimer factors were experimentally determined from samples with well-known composition for every cation in the system BSCF. Stoichiometric titanates ($ATiO_3$) of all cations are available. $BaTiO_3$ and $SrTiO_3$ single crystal samples as well as $CoTiO_3$ and $FeTiO_3$ powder samples (purity 99.8 %) were prepared for TEM. The $k_{A,Ti}$ factors were calculated from spectra taken at different sample thicknesses. For lighter elements (Sr, Co and Fe) $K_{\alpha 1}$-lines were evaluated, while for the heavier Ba the $L_{\alpha 1}$-line was used for investigation. As the X-ray peaks of Ba (L_α) and Ti (K_α) are too close for an adequate separation, the additional standard $BaFe_{12}O_{19}$ was investigated. The Ba-content of this standard material was analyzed by gravimetric assay with H_2SO_4 to be 11.8 % compared to calculated 12.4 % for the stoichiometric material.

In order to correct for X-ray absorption which occurs in the samples in dependence of thickness, absorption-free $k_{A,B}$ factors for a extremely thin sample were extrapolated by a method developed by Horita et al. [89, source not checked] which is step by step explained by the same author [90]. Under the assumption that all X-rays are generated in the first half of the sample film, the Beer-Lambert law can be rewritten as:

mass-absorption coefficient $[\frac{cm^2}{g}]$	Ba-$L_{\alpha 1}$ (4.47 keV)	Sr-$K_{\alpha 1}$ (14.17 keV)	Co-$K_{\alpha 1}$ (6.93 keV)	Fe-$K_{\alpha 1}$ (6.40 keV)	Ti-$K_{\alpha 1}$ (4.51 keV)
$BaFe_{12}O_{19}$	163	-	-	118	-
$SrTiO_3$	-	23	-	-	292
$CoTiO_3$	-	-	120	-	124
$FeTiO_3$	-	-	-	147	115

Table 3.3: X-ray mass-absorption coefficients [91, 92] in standard material exponentially interpolated for the corresponding energy of the X-ray lines indicated in brackets.

$$ln\frac{I_A}{I_B} = ln\left(\frac{I_A}{I_B}\right)_0 + \Delta_{AB}t. \tag{3.4}$$

While t is the thickness of the sample, Δ_{AB} describes the thickness dependence of X-ray absorption and contains sample and experimental parameters like density, mass absorption coefficients, and take-off angle of the detector (FEI Titan^3 80-300: 14.6°). As the thickness of the sample is elaborate to determine, equation 3.4 can be further simplified introducing a modified thickness dependence of the X-ray absorption Δ^*_{AB} [90]:

$$ln\frac{I_A}{I_B} = ln\left(\frac{I_A}{I_B}\right)_0 + \Delta^*_{AB}I_x. \tag{3.5}$$

This equation is true under the assumptions that few electrons are backscattered, electrons loose a negligible fraction of their energy in the sample and that the electrons pass straight through the foil. All these requirements are met by a thin sample. In addition, the assumption must hold that the X-ray absorption of element x whose peak intensity I_x is used for calculation is small. Mass-absorption coefficients for the relevant X-ray energies for the standards under investigation are listed in Table 3.3 [91]. The data from the paper is available in an online database [92] and was interpolated exponentially for the exact X-ray energies of the corresponding line. As the standard samples were very thin, also larger X-ray absorption values are acceptable for the evaluation employing equation 3.5.

For each standard sample, spectra within areas with different thickness t were taken under the identical measurement conditions (illumination: spot size 6; 70 µm condenser aperture). The background subtraction was performed by fitting a 5$^{\text{th}}$ order polynomial to the signal in the chosen energy windows and by extrapolation under the characteristic peaks. Peak fitting was performed standard-less by fitting of GAUSSians to the characteristic peaks of the $K_{\alpha 1}$- and $L_{\alpha 1}$-lines of the background-corrected data.

cation	$k_{A,Ti}$ factor (this work)	$k_{A,Si}$ factor (TIA)
Ba	3.17	3.08
Sr	3.10	3.03
Co	1.27	1.44
Fe	1.08	1.36

Table 3.4: Experimentally determined $k_{A,Ti}$ factors for thin-foil approximation compared to $k_{A,Si}$ factors from TIA.

This method gives best results compared to other background subtraction techniques available in the TIA program. The fitting procedure was repeated until a reproducible result was registered, as the result may change during the first 5-10 fit iterations of the algorithm used in TIA.
In a second step TIA calculates the k-factors of each position (thickness) of the different standard spectra. Figure 3.5 shows the logarithms of the determined $k_{A,B}$ factors: a) $k_{Ba,Fe}$ for $BaFe_{12}O_{19}$, b) $k_{Sr,Ti}$ for $SrTiO_3$, c) $k_{Co,Ti}$ for $CoTiO_3$, and d) $k_{Fe,Ti}$ for $FeTiO_3$ in dependence on the peak intensities of the standard element with weakest X-ray absorption (see Table 3.3) at constant beam current. The TEM sample thickness cannot be directly determined. However, the extrapolation to zero intensity in these graphs (Figure 3.5) yields the $k_{A,B}$ factor for the thin-foil approximation. The intersection of the fitted straight lines (red curves in Figure 3.5) with the y-coordinate gives the logarithm of the absorption-free Cliff-Lorimer factor. The spread of the data points is maximum for the $BaFe_{12}O_{19}$ standard due to the significant difference in Ba- and Fe-composition. It is hard to find another stable standard for Ba as the material has to be easily accessible, preparable for electron microscopy, pure and stable under vacuum conditions and stable under electron irradiation. In BSCF the Fe content is also very small. For these reasons the rather poor quality of the $k_{Ba,Fe}$ data was accepted.
Table 3.4 shows the determined $k_{A,Ti}$ factors which were used for further evaluations compared to the $k_{A,Si}$ factors included in the TIA program. One has to remark that these k-factors yield compositions in weight percent. The value for $k_{Ba,Ti}$ is calculated on basis of $k_{Fe,Ti}$ and $k_{Ba,Fe}$ using equation 3.3. According to equation 3.3 the influence of the experimental Cliff-Lorimer factors can be considered by calculating $k_{Ba,Sr}$ and $k_{Co,Fe}$ for both sets of factors. While the effect on the quantification of the A-site cations Ba and Sr is negligible ($k_{Ba,Sr}$(this work)=$k_{Ba,Sr}$(TIA)=1.02), there is a significant change for the B-site cations Co and Fe ($k_{Co,Fe}$(this work)=1.18 vs. $k_{Co,Fe}$(TIA)=1.06).
All quantitative EDXS analyses presented in this study refer to cation concentrations and are normalized to a cation concentration of 100 %. The concentration of O-anions

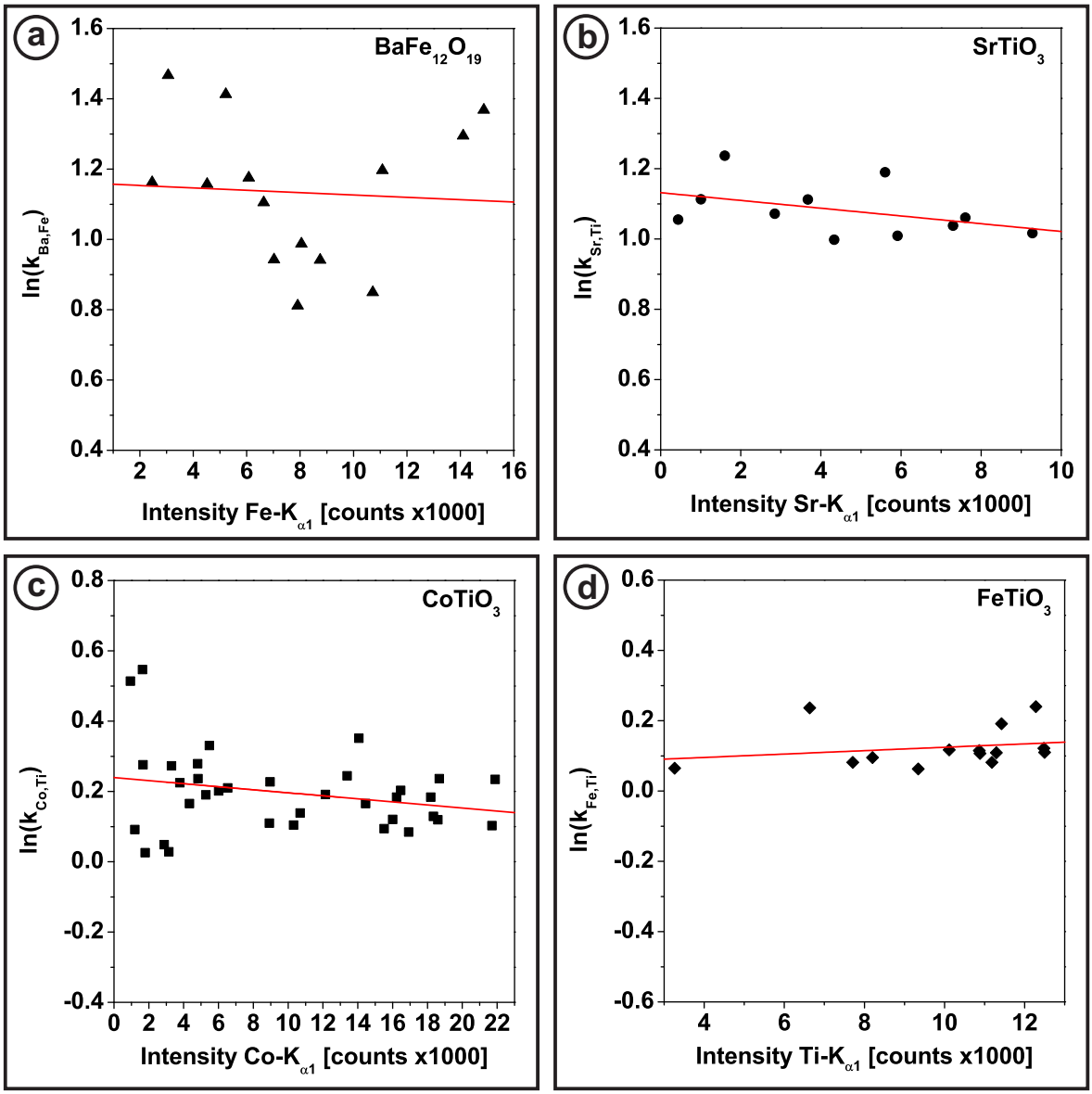

Figure 3.5: Plot of the CLIFF-LORIMER factors as a function of the element with the weakest X-ray absorption at the energy of the characteristic X-ray line for a) $BaFe_{12}O_{19}$, b) $SrTiO_3$, c) $CoTiO_3$, and d) $FeTiO_3$.

is not monitored as it may introduce a large error to the quantification due to the low X-ray yield expected for light atoms. Additionally, EELS investigations of this study indicate that the oxygen concentration of an MIEC may be subject of change under vacuum conditions in the electron microscope. For qualitative evaluations conducted for the investigation of composition mappings, the O-concentration was monitored and yielded an relatively homogenous concentration throughout distinct phases under investigation. According to Kriegel et al. [93], the oxygen deficiency d is expected to be in the range of 2.3-2.5. For a rough estimate of absolute atomic concentrations one can therefore assume oxygen concentrations of 50-60 at%.
In general, the error in determining the cation concentrations has a random and a systematic part. The systematic error results from imprecise background subtraction, peak-fitting, and absorption effects, as well as potential artifacts introduced by Ar^+-ion milling. Overall the remaining systematic error is estimated to be ± 3 at % and applies to all data presented in the study. The random error is determined by the standard deviation of the mean value of multiple measurements. Whenever multiple measurements were possible, the random error was calculated and presented in context with the data. Time-consuming measurements like line profiles and mappings could not be repeated due to duration and instability of the sample under permanent electron illumination.

3.8 Co-valence state determination by EELS

Electron Energy Loss Spectroscopy (EELS) is a very versatile analysis method in TEM, which is particularly sensitive to light-element detection. When electrons transmit a thin sample, there is a certain probability that they lose energy owing to inelastic scattering. By analyzing the energy loss of the electrons after interaction with the sample using a spectrometer, one therefore gains information on the chemical composition of the sample, on bonding and also on the chemical valence state of the contained elements.
Usually, two regions being different in energy are distinguished in a typical EEL spectrum. The low-loss region (0-50 eV) exhibits the zero-loss peak and plasmon or single-valence electron peaks depending on the electron structure of the material. Parameters like sample thickness and electronic properties like covalent bond excitations can be determined from the low-loss signal. The high-loss region (50-2000 eV) shows the element-specific ionization edges which are superimposed on a background that decreases exponentially with energy loss. For earth alkaline atoms and transition metals, the ionization edges are also called white-lines as they feature a steep, double-peak shaped rise of the signal.
The features of the high-loss spectrum give information on the chemical composition

of the sample. The fine structure of an ionization edge (Energy-Loss Near-Edge Structure (ELNES)) can be used to fingerprint different chemical bonds by probing the symmetry of the ligand field in a crystal. Furthermore, information on the valence-state of the element generating the ionization edge is accessible.
A modern spectrometer for EELS can be operated in a spectroscopic mode with parallel acquisition of all energy-loss channels (parallel EELS mode) as well as in an imaging mode enabling the registration of filtered images. The EEL spectrometer can be attached to a transmission electron microscope in two different ways:

- An in-column filter is incorporated into the microscope column below the diffraction lens. All electrons pass the filter during operation of the microscope. The filter is designed in a way that its influence on the resolution of the microscope is minimized. The advantage of an in-column filter is a very high count rate for energy filtered imaging and the availability of a filtered image and diffraction pattern on all image recording devices. However, image artifacts introduced by the spectrometer are also present for unfiltered applications.

- The second implementation is an additional device which is mounted at the end of the microscope column (post-column spectrometer). The filtered images and parallel EEL spectra are recorded by an additional camera behind the electron optics of the filter. The EELS system used for spectroscopy in the present study is of the post-column type.

A complete overview on EELS instrumentation and EELS techniques is presented, for instance, in the textbook edited by Ahn [94].
In the present study, EELS investigations mainly aimed to the determination of the Co-valence state in cubic BSCF and secondary phases. It is expected that the instability of the cubic phase is induced by a change of the Co-valence state towards higher oxidation with decreasing temperature [24, 28]. As the higher valence state goes along with a decrease of the ion radius of Co, the cubic phase may be unstable according to Goldschmidt [15]. A determination of the Co-valence in BSCF at nanometer resolution would therefore be highly desirable. As conventional valence determination by EELS is impeded in BSCF by overlapping Ba- and Co-signals, a new, enhanced evaluation method was developed in the course of this work (see section 3.8.2).

3.8.1 White-line ratio technique

For transition metals the transitions of 2p core electrons to unoccupied states near the Fermi level induce very intense peaks denoted as white-lines. They are a striking feature of the inner-shell ionization edges of the EEL spectrum, which is, apart from

the white-lines, dominated by absorption edges with a lower rise of the signal. Due to spin-orbit coupling, the 2p state splits into two different energy levels for j=$\frac{1}{2}$ ($2p_{1/2}$) and j=$\frac{3}{2}$ ($2p_{3/2}$). Therefore, a pair of white-lines in the case of Co denoted as L_3 and L_2 is generated [71]. Simple considerations lead to the assumption of an intensity ratio of 2:1 between the set of white-lines. This is motivated by theoretical calculations of the multiplicity m of the initial states associated with the white-lines Co-L_3 ($2p_{3/2}$; m=4) and Co-L_2 ($2p_{1/2}$; m=2). It was soon determined by theoretical studies of the branching ratio that a deviation from this simple behavior has to be expected [95, 96]. It was determined by EELS that the white-line intensity ratio changes as a function of the valence state suggesting that it is a well-suited property for the determination of the transition metal valence states. Pearson et al. describe a way how to evaluate the white-line ratio of appropriate EEL spectra [97]. For the determination of the Co-valence state the white-line ratio technique is well established and was applied by several groups [98, 99].

As described in section 2.3, the valence state of Co is the crucial factor for the stability of the cubic perovskite phase in BSCF. However, evaluating the Co-$L_{2,3}$ intensity ratio (Co-L_3 with an onset at an energy loss ΔE=779 eV, Co-L_2 at ΔE=794 eV) in BSCF is impeded by the presence of the Ba-$M_{4,5}$ white-lines (Ba-M_5 at ΔE=781 eV; Ba-M_4 at ΔE=796 eV) which are superimposed on the Co-$L_{2,3}$ edges.

To apply the EELS processing method by Pearson et al. [97], a set of reference spectra of materials with known valence state is required. Publications of energy loss spectra of Co depending on its valence states are rare [98] and the exact fine structure may depend on the particular acquisition system and data-analyzing procedure. Therefore, standard materials consisting of CoO (2+, 99.999 % purity), Co_3O_4 (2.66+, 99 % purity), $LiCoO_2$ (3+, 99.5 % purity), and $CoSi_2$ (4+, 99 % purity) powders were prepared for TEM and analyzed. In addition, metallic Co was prepared and investigated to check for possible preparation artifacts leading to a loss of oxygen of the other standards. To assure a certain repoducibility of the measurements performed on standards, a set of about 10 different crystallites in different samples was investigated to detect possible impurities or changes of the valencce state under the extreme conditions during electron irradiation.

EEL spectra were recorded in the STEM mode of the FEI Titan^3 80-300 microscope. The energy resolution was determined from the Full Width at Half Maximum (FWHM) of the Zero-Loss Peak (ZLP) yielding values as low as 0.7 eV. Spectrometer dispersions of 0.05 eV/channel and 0.1 eV/channel were chosen with a total channel number of 2048. The collection angle of the spectrometer was set to 13 mrad, the convergence angle of the electron probe was 17 mrad yielding a probe size $<$1 nm (spot size 6; 70 µm condenser aperture). Both collection angle and probe size influence the SNR of the EELS measurement. We do not expect any artifacts in the spectra due to the

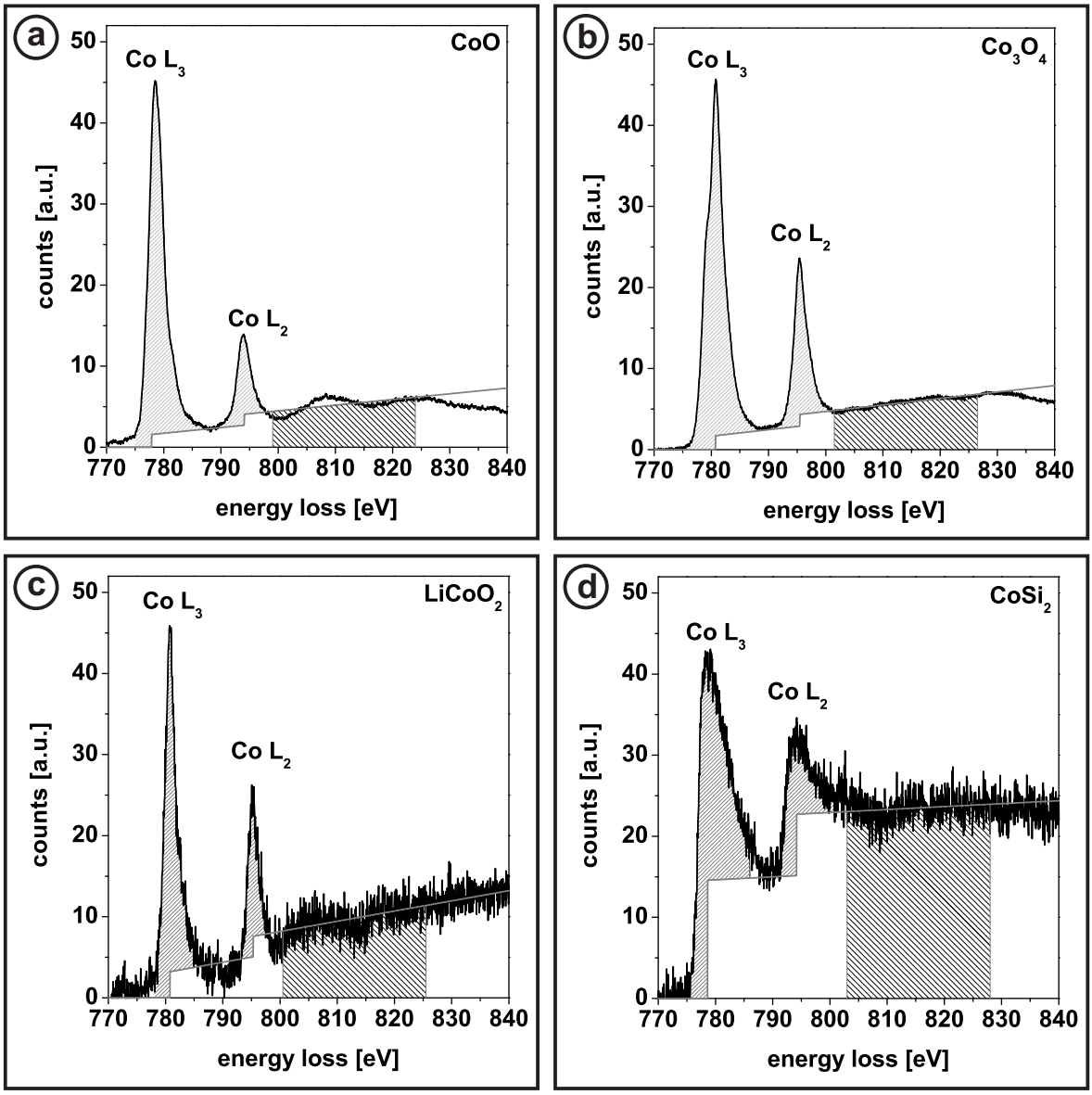

Figure 3.6: EEL spectra in the energy range of the Co-$L_{2,3}$ edge taken from reference samples a) CoO, b) Co_3O_4, c) $LiCoO_2$, d) and $CoSi_2$. The 25 eV background windows for a linear fit are shaded dark. The modeled background is indicated by the light gray curve. The evaluated peak area is shaded light gray. Dispersion: 0.05 eV/channel.

ratio between collection and convergence angle. The values were selected as reasonable compromise between signal quality, lateral resolution, and energy resolution. The experimental setup was kept constant for all EELS measurements presented in this study. The EEL spectra were processed using the Digital Micrograph (DM) software (version 1.71.38).

The method suggested by PEARSON et al. [97] was tested for its application to the Co-valence in BSCF which requires the determination of the Co-$L_{2,3}$ intensity ratio. This technique is sensitive to the sample thickness , i.e. due to the convolution of the core-loss signal with plasmon excitations. Artifacts can arise that influence the background determination at the high-loss side of the white-lines (see Figure 3.6). Therefore, the relative thickness was monitored by the log-ratio technique implemented in the DM software. This technique evaluates the ratio of the zero-loss intensity with respect to the total intensity of the EEL spectrum of a chosen sample region. The investigated sample regions were selected as thin as possible. If necessary, multiple-scattering effects were removed by the FOURIER-ratio deconvolution technique implemented in the DM software.

Figure 3.6 shows representative spectra of a) CoO, b) Co_3O_4, c) $LiCoO_2$, and d) $CoSi_2$ and demonstrates the analyzing procedure of the L_3/L_2 white-line ratio described by PEARSON et al. [97]. Due to damage of $LiCoO_2$ and $CoSi_2$ under high-energy electron irradiation (300 keV), the corresponding spectra c) and d) were taken at much shorter acquisition times and, therefore, are noisier.

To determine the white-line ratio, the background was subtracted by fitting a power law to an energy window of 10 eV selected in front of the Co-L_3 white-line. Figure 3.6 shows the residual spectra after background subtraction. Furthermore, it has to be taken into account that the Co-L_2 white-line is superimposed on the Co-L_3 white-line. The Co-L_3 intensity under the Co-L_2 white-line was subtracted by the following procedure. A window with an energy width of 25 eV (shaded areas Figures 3.6a)-c)) beyond the Co-L_2 white-line was selected, as it contains the contribution of both backgrounds. A linear fit (gray lines in Figures 3.6a)-c)) was calculated and extrapolated towards lower energy losses. A step at the maximum position of the Co-L_2 white-line is introduced with a ratio of 2:1. This is motivated by the different multiplicity m of the initial states. The energy boundaries of the white-line peaks for integration were chosen as indicated by the light gray background in Figure 3.6.

The values determined for the white-line ratios are listed in Table 3.5 including the Co-$L_{2,3}$ intensity ratio for metallic Co for comparison. The calculation of the Co-$L_{2,3}$ intensity ratio for $CoSi_2$ is only possible with a large error because the Co-L_2 white-line does not have a distinct line shape but rather an edge-like appearance. Reference data taken from WANG et al. [98] are also included in Table 3.5. Reference materials marked by an asterisk are different from the materials in our study. The white-line

Co-standard	valence	white-line ratio	white-line ratio [98]	white-line dist. [eV]
metallic		3.3		15.06 ± 0.06
CoO	2	4.8	4.5(*); 5.0(**)	15.41 ± 0.02
Co_3O_4	2.66	2.9	3.25	14.53 ± 0.04
$LiCoO_2$	3	2.5		14.46 ± 0.02
$CoSi_2$	4	(2.7)	2.0	15.40 ± 0.12

Table 3.5: Co white-line ratio and white-line distances determined for reference spectra with defined valence states [(*)$CoSO_4$, (**) $CoCO_3$]. Values in brackets are imprecise due to the shape of the spectrum. The presented errors for the white-line distances are the standard deviations of the average value of multiple measurements.

ratios for both, the values of this work and the values of Wang et al. [98] differ. This illustrates the dependence on the particular EELS system and measurement conditions. The Co-$L_{2,3}$ intensity ratio does not linearly depend on the Co-valence state. However, the dependence is monotone which is the basis for determining the valence state.
To apply the white-line ratio based evaluation method to spectra of BSCF, a deconvolution of the Ba-signal is necessary. To deconvolve the contribution of the Ba-$M_{4,5}$ white-lines, Multiple Linear Least Square (MLLS) fitting of standard spectra [100, 101] was applied. A set of CoO, Co_3O_4, and $BaTiO_3$ (single crystal) spectra, which were acquired under the same experimental conditions as the BSCF spectra, was carefully aligned and fitted before employing the MLLS algorithm of the DM software package. The Co-L_3 lines of CoO, Co_3O_4, and BSCF were aligned at 778 eV at the half-maximum intensity of the Co-L_3 white-line. As $BaTiO_3$ does not contain Co, the Ba-M_5 line of $BaTiO_3$ was separately fitted to the BSCF spectrum which results in a position of the Ba-M_5 line at 784.5 eV.
In Figure 3.7a), spectra of different phases (cubic phase-black; BCO-type phase-blue; hexagonal phase-red) in BSCF (see section 4.1.2) are compared. The spectra are aligned to the same Co-L_3 intensity. Differences in the white-line ratio can be directly distinguished prior deconvolution of the Ba white-lines. The spectrum presented in Figure 3.7b) represents the residual of the spectrum of a cubic region after the subtraction of the Ba fraction determined by MLLS fitting.
Despite prominent artifacts due to discrepancies of the Ba white-line shapes between the standard and BSCF, the white-line ratio determination can be accomplished after the deconvolution of the Ba-signal. The Co-$L_{2,3}$ intensity ratios were determined and are listed in Table 3.6. The values in Table 3.6 clearly disagree with the values of the reference materials in Table 3.5 and do not allow the assignment of the Co-valence. This can be explained by artifacts in the EEL spectra resulting from the Ba white-line subtraction.

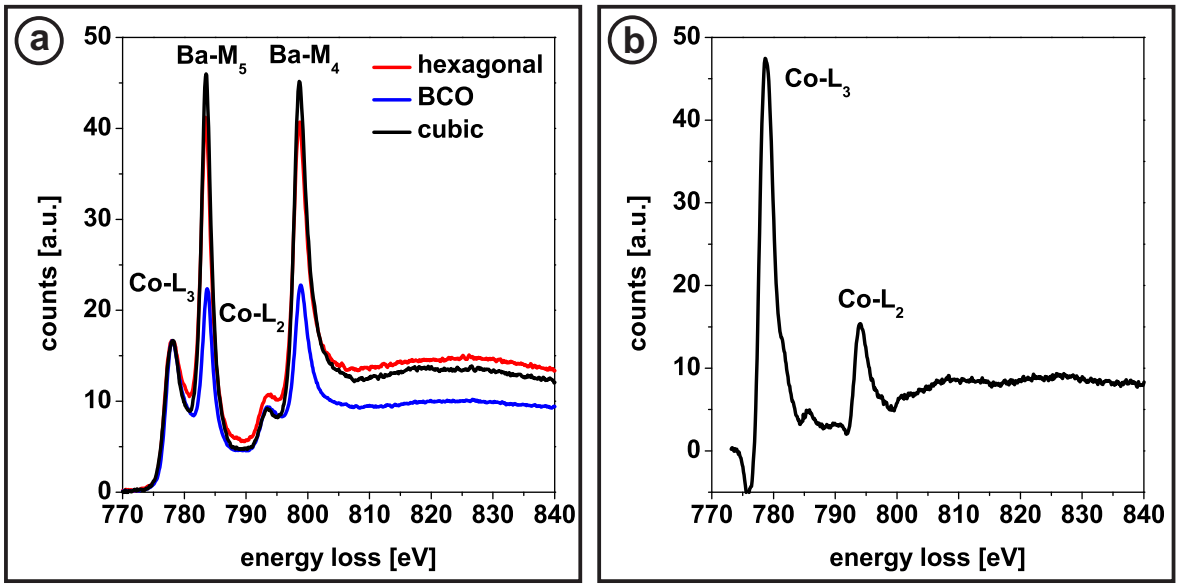

Figure 3.7: a) EEL spectra of different BSCF phases scaled and aligned to the same Co-L_3 white-line intensity, b) residual of the spectrum of a region with cubic structure after the subtraction of the Ba-fraction determined by MLLS fitting.

phase	Co-$L_{3,2}$ ratio	Ba [at%]	Sr [at%]	Co [at%]	Fe [at%]
cubic	6.9	28	28	33	11
cubic	6.6	29	27	34	10
hexagonal	6.9	28	20	51	1
hexagonal	6.8	31	21	47	1
BCO-type	6.7	21	4	70	5
BCO-type	7.1	14	4	79	3

Table 3.6: Co-$L_{2,3}$ intensity ratios after subtraction of the Ba-$M_{4,5}$ lines and cation composition of different BSCF phases in at% based on EDXS measurements at two different positions.

In addition to accuracy issues, the technique is very time-consuming. It is also difficult to automate MLLS fitting which makes the determination of intensity ratios for a large number of spectra from EELS maps clearly not feasible. Moreover, an excellent SNR is required that cannot be achieved for short recording times during the acquisition of EELS linescans and maps. For this reason, other features of the Co-$L_{2,3}$ edges have to be considered allowing the fast quantitative determination and mapping of the Co-valence state. In the course of this study, a new method for Co-valence determination was developed. It is presented in the next section 3.8.2.

3.8.2 White-line distance technique

Based on studies by Arnold et al. [28] and Efimov et al. [24] it will be shown in the following that the distance between the maxima of the Co-L_3 and Co-L_2 lines allows the assignment of Co-valence states. The determination of the Co-valence in BSCF is based on the data of the reference materials in Table 3.5. The distance between the white-lines was determined by fitting Gaussians to the white-lines. The energy window for the fit was chosen in a way that the residual after the fit was minimal for a window of ± 0.5 eV around the highest white-line intensity. This was necessary because of the different shapes of the white-lines depending on the valence state. The presented errors are the standard deviations of multiple evaluations.
For valences between 2+ and 3+ a distinct assignment of the white-line distance to the valence state is possible as the distances decrease monotonously from 15.41 eV to 14.46 eV, suggesting a correlation between the Co-valence state and the Co-$L_{2,3}$ line distance. Spectra of Co 4+ which might cause an ambivalent assignment have to be excluded.
If one assumes a monotone dependence between the white-line distance and the Co-valence state, one can interpolate between the measurements on standards and directly determine the Co-valence in an unknown sample by EELS analysis. Figure 3.8 demonstrates the interpolated reference data for the valence state assignment based on the white-line distance. Valences between 2+ and 3+ can be assigned. The error bars correspond to the standard deviations listed in Table 3.5 and an additional error of ± 0.2 eV which accounts for the inaccuracy of the peak determination and systematic error contributions of the GIF system.
As a fundamental physical relation describing the dependence of the white-line distance from the valence state is not available, several functions were fitted to the data. The linear fit (black curve) and the exponential fit (blue curve) result in nearly the same dependence. Furthermore, a 2^{nd} order polynomial was fit to the data (red curve). A linear interpolation between two pairs of measurements is represented by the green curve.

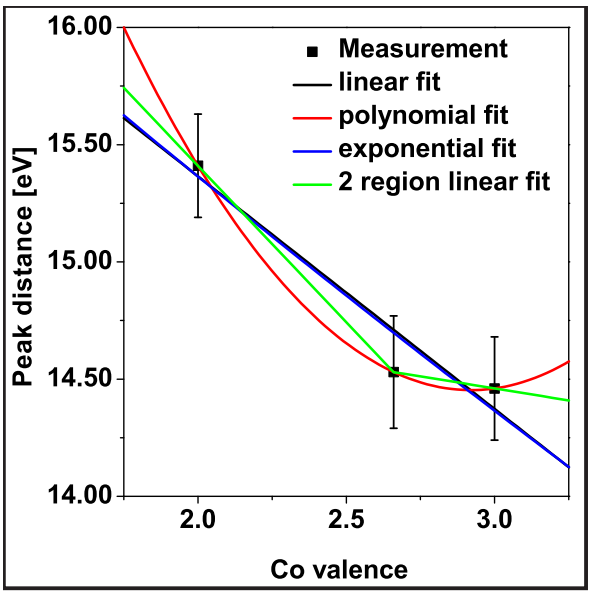

Figure 3.8: Valence state assignment in dependence of Co white-line peak distance. The error bars are due to the standard deviations listed in Table 3.5 and a cumulated error of 0.2 eV accounting for inaccuracies of the peak determination and the systematic error of the GIF system.

white-line distance [eV]	linear	polynomial	exponential	2-region linear	standard deviation
15.56	1.80	1.93	1.81	1.88	0.06
15.46	1.90	1.97	1.90	1.96	0.04
15.37	2.00	2.02	2.00	2.03	0.02
15.27	2.10	2.07	2.10	2.11	0.02
15.17	2.20	2.13	2.19	2.18	0.03
15.07	2.30	2.18	2.29	2.26	0.05
14.97	2.40	2.25	2.39	2.33	0.07
14.87	2.50	2.31	2.49	2.41	0.09
14.77	2.60	2.39	2.59	2.48	0.10
14.67	2.70	2.48	2.69	2.55	0.11
14.57	2.80	2.60	2.79	2.63	0.11
15.47	2.90	2.79	2.89	2.94	0.06

Table 3.7: Comparison of different dependences between white-line distance and valence state for typical white-line distances measured in BSCF. The standard deviation of the fits describes the uncertainty introduced by the lack of a theory describing the relationship.

Table 3.7 gives the valence states calculated from typical white-line distances according to the different dependences. The standard deviation listed in the last column of Table 3.7 demonstrates the uncertainty of the different results depending on the white-line distance. For large white-line distances, i.e. low valence number, the different fits hardly change the result of the assignment. The systematic error due to the assignment was therefore estimated to a maximum of ± 0.1. For smaller white-line distances (higher valences) the standard deviation of the valence state due to the different assignments was calculated to be larger than 0.1. The maximal systematic error was therefore assumed to be ± 0.2. The Co-valence assignment was tested based on all fit functions. The Co-valence determination in the present study was performed on the basis of the linear fit as it is the most simple model.
The presented evaluation method was used to determine the Co-valence state of secondary phases in BSCF. The results are presented in section 4.1.8. A more profound overview on the physical models explaining the shift of the white-line distance and the errors of this evaluation method is given in the discussion in 3.8.3.

3.8.3 Discussion

In the present subsection the electronic effects which may lead to a change of the white-line distance used for valence determination of the Co-cation are discussed. Furthermore, the accuracy of the presented evaluation method for the Co-valence is estimated. As suggested by Arnold et al. [28] we assume that individual Co-cations have intermediate Co-valence states as opposed to a mixture of Co-cations with different integer valence states. The assumption is justified because the cubic and hexagonal BSCF phases comprises only one indistinguishable Co-site in the lattice and therefore accommodate only one indistinguishable type of cations.
Calculated and measured EEL spectra of other groups give insight into the electronic effects which cause a the change of the white-line distance for standard samples with integer valence states caused by the symmetry of the ligand field in the materials crystal structure. Unfortunately, simulations concentrate on valence states with integer number rather than intermediate values. Fink et al. [102] calculated the 2p to 3d transition probability for transition metals and demonstrated that the L_3 white-line can be resolved into a sub-structure which presents a possible explanation for a correlation between white-line distance and Co-valence. The theoretical study by De Groot et al. [103, 104] suggests that the energy splitting of the L_3 white-line is caused by a multiplet structure of the final transition states. De Groot et al. [103, 105] also show spectra of materials containing Co-cations with a valence state of 2+ and 3+ displaying

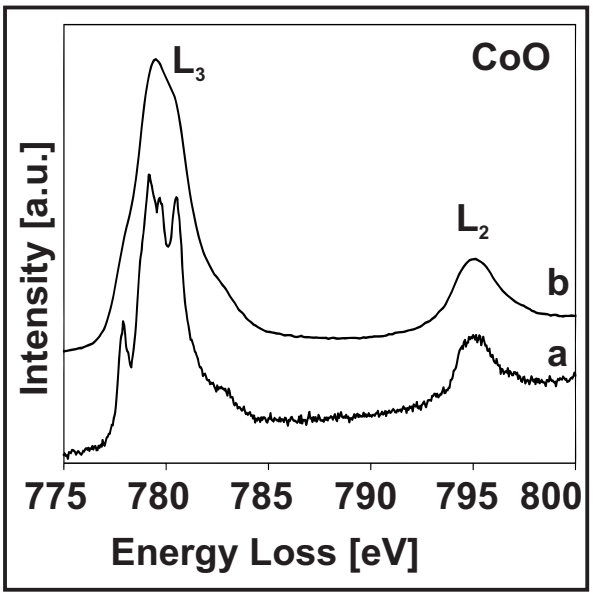

Figure 3.9: Fine structure of the Co 2+ L_3 white-line measured on a CoO standard by MITTERBAUER et al. [107].

a significant change in the L_3 white-line sub-structure. A change of the Co-valence is expected to appear as an overall shift of the white-lines to higher energies (chemical shift).

ABBATE et al. [106] present simulated spectra for Co 2+, 3+, and 4+ which verify the chemical shift effect. In addition to an overall shift of the white-lines as a function of the valence state, a multiplet structure of the Co-L_3 line is predicted which changes in dependence on the valence state. However, the white-line distance is predicted to be constant (15.2 eV) by this work. The simulation apparently does not include all relevant physical effects.

MITTERBAUER et al. [107] recorded EEL spectra of CoO with an energy resolution of 0.15 eV using a monochromated FEG as electron source. The published data is presented in Figure 3.9. Curve a) shows the data recorded with high energy resolution in contrast to spectrum b) which was taken at a resolution being comparable to that in the present study. The Co-L_3 white-line is composed of 4 overlapping sub-peaks, while a sub-structure of the L_2 white-line was not observed despite of the high energy resolution. Differences in the fine-structure of 2p transitions were reported by ZAANEN and SAWATZKY [108] due to an additional COSTER-KRONIG decay affecting the high energy-loss white-lines.

In the present study the monochromator equipped to the Titan^3 80-300 microscope was not used due to the tremendous intensity loss in the EELS signal. Nevertheless, indications of the Co-L_3 sub-structure can also be recognized, e.g., in the spectrum of Co_3O_4 (Figure 3.6 b)) where a distinct shoulder is recognized for the Co-L_3 white-line. The explanation of the multiplet structure of the L_3 white-line is complex and may in-

volve COULOMB exchange interactions between p and d electrons [107]. A crystal-field multiplet model describes the Co-$L_{2,3}$ edges of CoO [104, 107] well.
The change of the Co-$L_{2,3}$ white-line distance used for the valence determination may be interpreted in the following way. Different Co-valence states may change the intensities of the different sub-peaks of the L_3 multiplet because screening of the Co-nucleus is reduced for higher valences. As the peak sub-structure is not resolved without monochromator, the different intensities of the sub-peaks lead to a shift of the maximum of the whole peak resulting from the overlap of the sub-peaks. This was demonstrated by spectra from standard materials with known Co-valence. The position of the white-line onset is constant for different valence states. Only the different shoulders of the peaks lead to a shift of the white-line maximum. While the L_3 white-line is affected by this shift, the L_2 white-line does not experience an energy shift due to the lack of a sub-structure [107]. To further substantiate this hypothesis, the energy split of the multiplet was determined from the experimental data of MITTERBAUER et al. [107] to be 1.33 eV, 0.51 eV, and 0.84 eV, respectively. The energy difference of 0.84 eV between the two lines with highest intensities agrees rather well with the difference of the white-line distances of 0.95 eV determined from the Co 2+ and Co 3+ standards (Table 3.5).
In 2009, ARNOLD et al. [28] recorded high-resolution EEL spectra of CoO and Co_3O_4 which were energy-calibrated with an error of ± 0.1 eV using Ba-$M_{5,4}$ as internal standard. An energy shift between the Co-L_3 maximum of both spectra was discovered which was used by EFIMOV et al. [24] to distinguish between different Co-valence states. The disadvantage of this method is that it requires an internal standard for energy calibration.
The accuracy of the valence-state determination depends on several delicate evaluation steps:

- The current understanding of the electronic effects leading to a white-line shift does not indicate a physical dependence which could be employed for the interpolation of measurement points determined from standards. The interpolation is necessary to assign non-integer valence states as they occur in BSCF. The used assignment of the valence state is based on a linear dependence from the white-line distance (Figure 3.8). According to Figure 3.8 and Table 3.7, the systematic error depends on the valence state itself. It was estimated to ± 0.1 for low valences (cubic phase) and ± 0.2 for high valences (hexagonal phase).

- The PCA algorithm facilitates the determination of peak positions with an accuracy of 0.2-0.3 eV dependent on signal quality. Different fit models to the standard data also yield different assignments of valence states to white-line distances. The error is believed to be negligible for data with very good SNR. For

mappings with a large set of individual measurements the standard deviation for the valence state of each phase was calculated. For the cubic phase the statistical error was determined to be ± 0.2. As the hexagonal phase contains more Co, the signal is usually less noisy and the statistical error is smaller (± 0.1).

The overall accuracy of the valence state assignment for spectra with sufficient SNR is therefore estimated to be ± 0.2. For EEL spectra with a particularly low SNR, larger errors up to ± 0.3 have to be accepted.
Systematic differences in the valence state for different samples may also be introduced by annealing as the valence state of Co in BSCF depends on the temperature. Furthermore, the loss of oxygen in the microscope due to electron irradiation could lead to an overall underestimation of the valences.

4 BSCF for oxygen separation membranes

The following chapter contains the results on doped and undoped BSCF bulk samples as well as thin-films. Bulk samples were investigated to determine the microstructure and secondary phases of BSCF after annealing. In a subsequent step, the suppression of the formation of secondary phases was studied on Sc-, Y- and Zr- doped samples. Furthermore, thin-films were prepared and studied to understand the formation of secondary phases at the surface. An LSC-based functional layer was coated on top of the thin-films to stop the formation of secondary surface phases and to improve oxygen exchange.
In addition to microstructural investigations the newly developed white-line distance based EELS evaluation (see section 3.8) was applied to determine the Co-valence state of cubic BSCF and the hexagonal secondary phase and to identify the degradation mechanism.

4.1 Bulk BSCF material

4.1.1 Material fabrication of bulk BSCF

Undoped BSCF bulk material and most of the doped BSCF bulk material was prepared using commercially available powder produced by the Fraunhofer Institut für Keramische Technologien und Systeme, Hermsdorf, Germany (IKTS) by the mixed-oxide procedure. The particle size was determined to be 2-3 µm. Green powder compacts were fabricated by cold isostatic pressing at 250 MPa. Subsequent sintering in air at 1100 °C or 1150 °C for 12 h depending on the dopant resulted in the desired BSCF bulk material.
Some BSCF bulk material was produced at the laboratory of our cooperation partner Institut für Werkstoffe der Elektrotechnik, KIT, Karlsruhe, Germany (IWE), also applying the mixed-oxide route. Stoichiometric amounts of $BaCO_3$, $SrCO_3$, Co_3O_4, Fe_2O_3, Y_2O_3, Sc_2O_3 and ZrO powders (Merck, Darmstadt, Germany) were mixed for 24 h and calcinated at 950 °C, 1050 °C or 1130 °C for 10-12 h in air. In a second step, the calcinated material was ground by ball billing for 24 h to a particle size of about 1-3 µm using zirconia balls. BSCF compacts were obtained by isostatic pressing at 250 MPa and subsequent sintering at 1100 °C for 12 h. Heating and cooling rates were programmed to be 5 K/min.

sample	powder source	powder size	calcination conditions	sintering conditions	heating rates	annealing conditions
undoped BSCF	IKTS	3.1 µm	proprietary	1000 °C; 12 h	5 K/min	650-1000 °C; 10-100 h
undoped BSCF	IKTS	2.4 µm	proprietary	1000 °C; 12 h	5 K/min	800 °C; 10-1350 h
3 % Zr-doped BSCF	IKTS	1 µm	proprietary	1100 °C; 12 h	5 K/min	700-1000 °C; 100 h
3 % Zr-doped BSCF	IWE	1 µm	1130 °C	1100 °C; 12 h	5 K/min	700-1000 °C; 100 h
3 % Sc-doped BSCF	IKTS	1 µm	proprietary	1100 °C; 12 h	5 K/min	700-1000 °C; 100 h-125 h
3 % Y-doped BSCF	IKTS	1 µm	proprietary	1100 °C; 12 h	5 K/min	700-1000 °C; 100 h-125 h
3 % Y-doped BSCF	IWE	0.16 µm	1050 °C; 2x10 h	1150 °C; 12 h	5 K/min	730-760 °C; 100 h-125 h
1 % Y-doped BSCF	IWE	0.4 µm	1050 °C; 2x10 h	1150 °C; 12 h	5 K/min	700-1000 °C; 100 h-125 h
10 % Y-doped BSCF	IWE	0.24 µm	1050 °C; 10 h	1150 °C; 12 h	5 K/min	700-1000 °C; 100 h-125 h

Table 4.1: Production parameters for BSCF bulk material.

To simulate application-conditions, the BSCF bulk material was subjected to annealing treatments. In advance of any annealing step, annealing at 1000 °C was performed for 10 h to 24 h to assure that BSCF is present in the cubic phase. The temperature was then reduced to the desired annealing condition, without removing the sample from the furnace.

The composition of the atmosphere during annealing (partial pressures of CO_2 and O_2) is known to influence the stability of BSCF [19, 46–48]. Most samples were annealed in air, while an additional series of samples was annealed in a pure N_2 atmosphere to ensure low O_2 partial pressures during temperature treatment. The cooling rate after annealing was chosen as fast as possible. Therefore, samples were quenched in water directly after removing them from the furnace. The phase composition at the desired annealing temperature is preserved by the fast cooling process and can be investigated at room temperature.

The fabrication parameters for all samples discussed in this work are summarized in Table 4.1. Data marked as “proprietary” is based on the experience of the external manufacturers and is therefore not disclosed.

4.1.2 Phases in BSCF as a function of temperature

The phase composition of BSCF was studied as a function of annealing temperature, gas atmosphere and time. Annealing in an atmosphere with low oxygen partial pressure (N_2-atmosphere) in the temperature range 650 °C-1000 °C did not lead to the decomposition of the cubic BSCF phase [109]. Conditions with extremely low oxygen partial pressure are not compatible to any application but contribute to the understanding of the degradation mechanism of BSCF. For annealing in ambient air, it was already known that the BSCF-system forms at least one secondary hexagonal phase [22–24]. The microstructure and amount of this secondary phase is strongly dependent on annealing conditions and can be well detected by electron microscopical techniques.
These studies involve the investigation of a large set of different samples. Information on the phase composition was, therefore, obtained by the fast phase mapping technique described in section 3.3. Three different morphologies of the hexagonal phase were discovered in the BSCF-system:

- Grains of the hexagonal phase at triple points and grain boundaries.
- Plate-like hexagonal and cubic polytypes (in the further course of this text denoted as *plate-like regions*) which contain thin lamellae of cubic, hexagonal and $Ba_{n+1}Co_nO_{3n+3}(Co_8O_8)$ (BCO)-type phases (see section 4.1.4) with a thickness of only a few nanometers.
- Crystallites of the hexagonal phase, which form in the vicinity of the plate-like regions: They are distinguished from the lamellae of the hexagonal phase in the plate-like regions by a much larger size.

Additionally, cobalt oxide precipitates were detected in the samples that also act as nucleation center for hexagonal transitions. Electron diffraction and chemical composition analysis by EDXS both identified the impurity in bulk material as cobalt monoxide (CoO). Figure 4.1 shows the different phases which occur after 100 h annealing in the temperature range between 700 °C and 1000 °C. Figure 4.1a) shows a sample after annealing at 1000 °C which contains only the cubic BSCF phase. The two large particles with bright contrast correspond to CoO precipitates. As not all microstructural features are visible in the SEM images Figures 4.1a)-d), the microstructure is schematically illustrated in Figures 4.1e)-h) which summarize the evaluation of numerous SEM images and the investigation of grain boundary regions by TEM. The colors of the cubic and hexagonal phase in these schemes are chosen with respect to their typical contrast in SEM images. After annealing at 900 °C (Figures 4.1b,f)) large plate-like regions with sizes of several micrometers are formed at grain boundaries. After annealing at 800 °C (Figures 4.1c,g)) the hexagonal phase is formed in addition to the

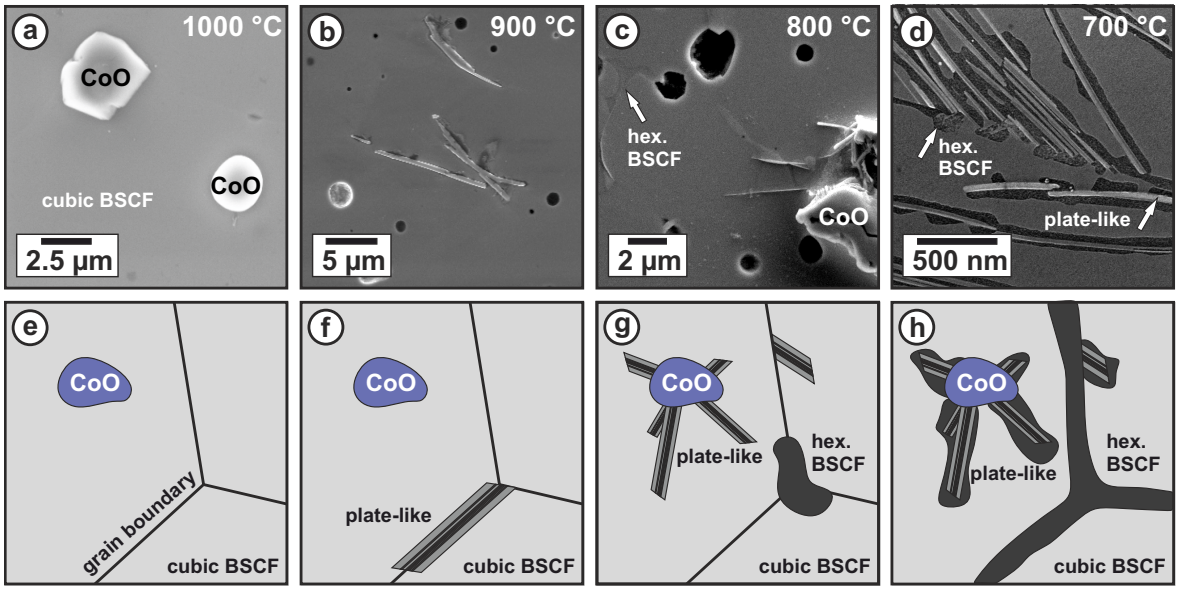

Figure 4.1: SEM images with corresponding schemes which illustrate the formation of secondary phases in BSCF after 100 h annealing at a),e) 1000 °C, b),f) 900 °C, c),g) 800 °C and d),h) 700 °C in ambient air.

plate-like regions. This finding is in good agreement with the results of Niedrig et al. [34]. The precipitation of the hexagonal phase typically occurs at triple points of grain boundaries. A typical hexagonal region with a slightly darker contrast compared to the surrounding cubic phase is marked in Figure 4.1c). Smaller plate-like regions nucleate at CoO particles and at grain boundaries. At 700 °C (Figures 4.1d),h)) the formation of plate-like regions is even more pronounced by the presence of fishbone-like structures. Furthermore, the hexagonal phase may completely decorate grain boundaries and occupies a large volume fraction in the vicinity of CoO particles and plate-like regions.

As the formation of the plate-like regions seems to be strongly correlated with the degradation of BSCF, the formation conditions were investigated. Figure 4.2 shows the content of the plate-like regions in dependence of the annealing time at 800 °C (Figure 4.2a)) and annealing temperature after 10 h of temperature treatment (Figure 4.2b)). The data was extracted from representatively chosen SEM images of polished samples by manually marking the plate-like regions. Automated image analyzing methods involving threshold-based particle detection, which are implemented in image processing software like imageJ [110] fail due to both, significant contrast variations caused by sample charging at low magnification imaging conditions and significant contrast variations at pore regions. The different phase volumes were corrected for the fraction of pores in the different samples. Due to the manual evaluation method, error bars are estimated to ± 2 vol %.

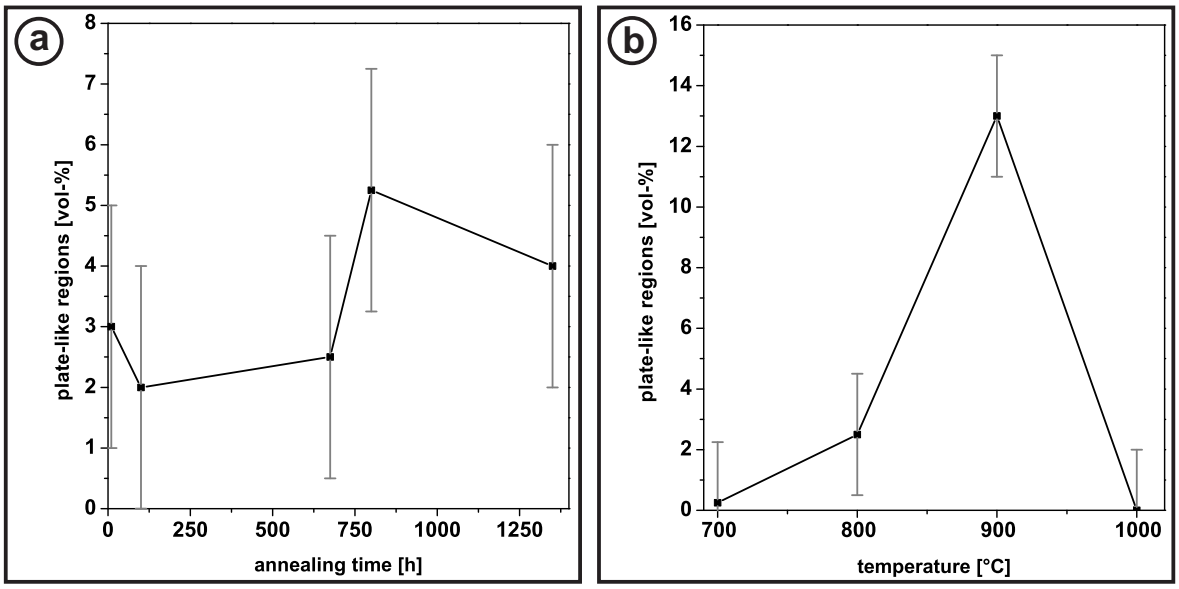

Figure 4.2: Content of plate-like regions in dependence of a) annealing time at 800 °C and b) annealing temperature after 10 h of annealing.

The fraction of the plate-like regions does not significantly change for annealing times larger than 10 h (Figure 4.2a)). Variation of the annealing temperature significantly changes the volume fraction of the plate-like regions (Figure 4.2b)). For the temperature range between 700 °C and 900 °C, a steep rise of the volume fraction was observed. This rise can be explained by the large size (of few) plate-like regions at 900 °C, leading to an increased volume fraction compared to samples annealed at lower temperatures. Overall, the number of plate-like regions is larger for lower temperatures. At 1000 °C no plate-like regions were detected.

Additionally, the amount of plate-like regions in dependence of the distance to the bulk surface was determined for a 3 % "Zr-doped" sample annealed at 800 °C in the course of the bachelor thesis of Haeberle [109] by the same manual evaluation technique. As outlined in section 4.1.6, Zr-cations in this sample were not successfully solved in the BSCF lattice and therefore do not have any influence on the depth dependency of the amount of secondary phases. Although the samples can be considered as undoped BSCF, the overall amount of secondary phases was much higher compared to the time and temperature dependent results (see Figure 4.2) for this sample due to different powder and fabrication batches. The homogenity of the distribution of secondary phases in the bulk material is necessary for representative TEM investigations, because it is hard to control the exact position of a TEM sample with respect to the bulk with conventional preparation techniques. The total sample thickness for this investigation was 1700 µm. Figure 4.3a) shows representative SEM images of a cross-section sample taken at different distances to the bulk surface.

The volume fraction (Figure 4.3b)) of plate-like regions at the surface is smaller than at

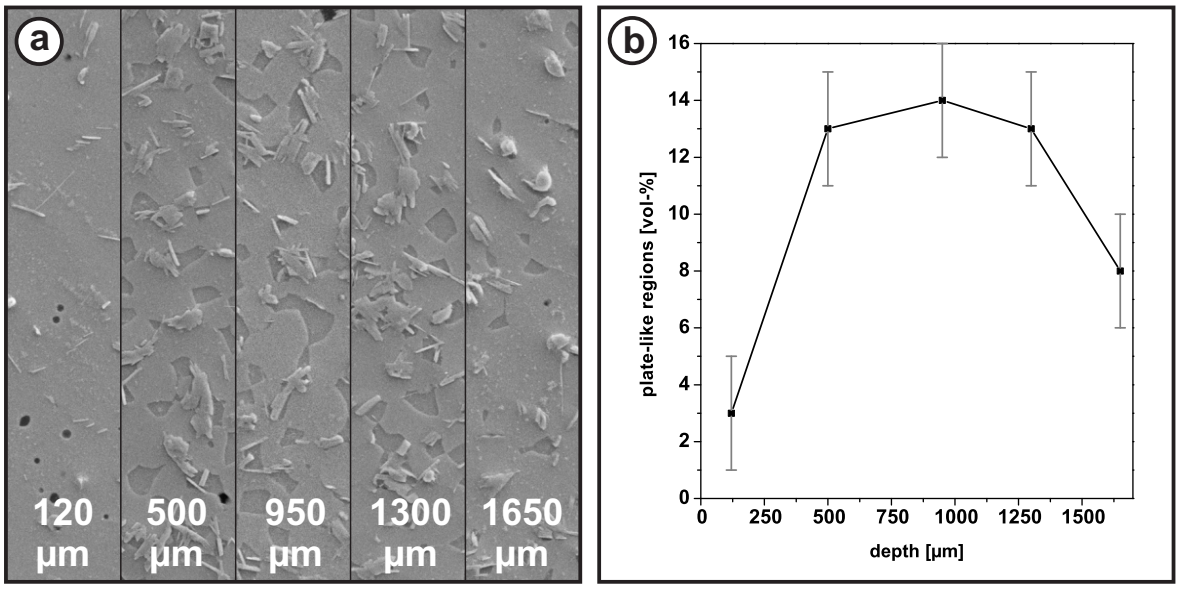

Figure 4.3: Content of plate-like regions in dependence of the distance to the bulk surface after annealing at 800 °C. a) SEM micrograph of different regions; b) volume fraction of plates. The total width of the sample is 1700 µm [109].

the center of the bulk sample, where a broad region of constant content was observed. All samples for TEM and SEM were prepared from material of this inner bulk region with constant volume fraction due to the preparation process which involves grinding of several 100 µm of the sample surface. The difference between the volume fraction determined for opposite surfaces (120 µm and 1650 µm in Figure 4.3a)) may stem from the orientation of the sample in the furnace. The surface with contact to the crucible (presumably right part of Figure 4.3a) may be different compared to the surface on top. Like the inner parts of the sample, the lower surface does not have a direct contact to the surrounding atmosphere during annealing.

4.1.3 Microstructure of the plate-like regions in BSCF

As the plate-like regions play a fundamental role in BSCF degradation in ambient air, the structure of the plate-like regions was investigated in detail by HRTEM and STEM. While the plate-like morphology can be directly imaged by SEM (for example Figures 4.1a)-c) or Figure 4.3a)), TEM bright-field images show a lamellar sub-structure of the plate-like regions. Figure 4.4 shows TEM images (Figures 4.4a,c)) and a scheme (Figure 4.4b)) of a typical plate-like region after annealing at 700 °C for 100 h. The overview bright-field TEM image Figure 4.4a) visualizes plate-like regions (indicated by dashed white boxes) and the hexagonal phase in the vicinity. The assignment of phases is based on SAED and CBED as reported in section 3.5, as well as Fourier-analysis of high-resolution TEM images (Figures 4.4c,d)). The plate-like regions consist of a lamellar sub-structure (inside white frames in Figure 4.4a)) which is schematically visu-

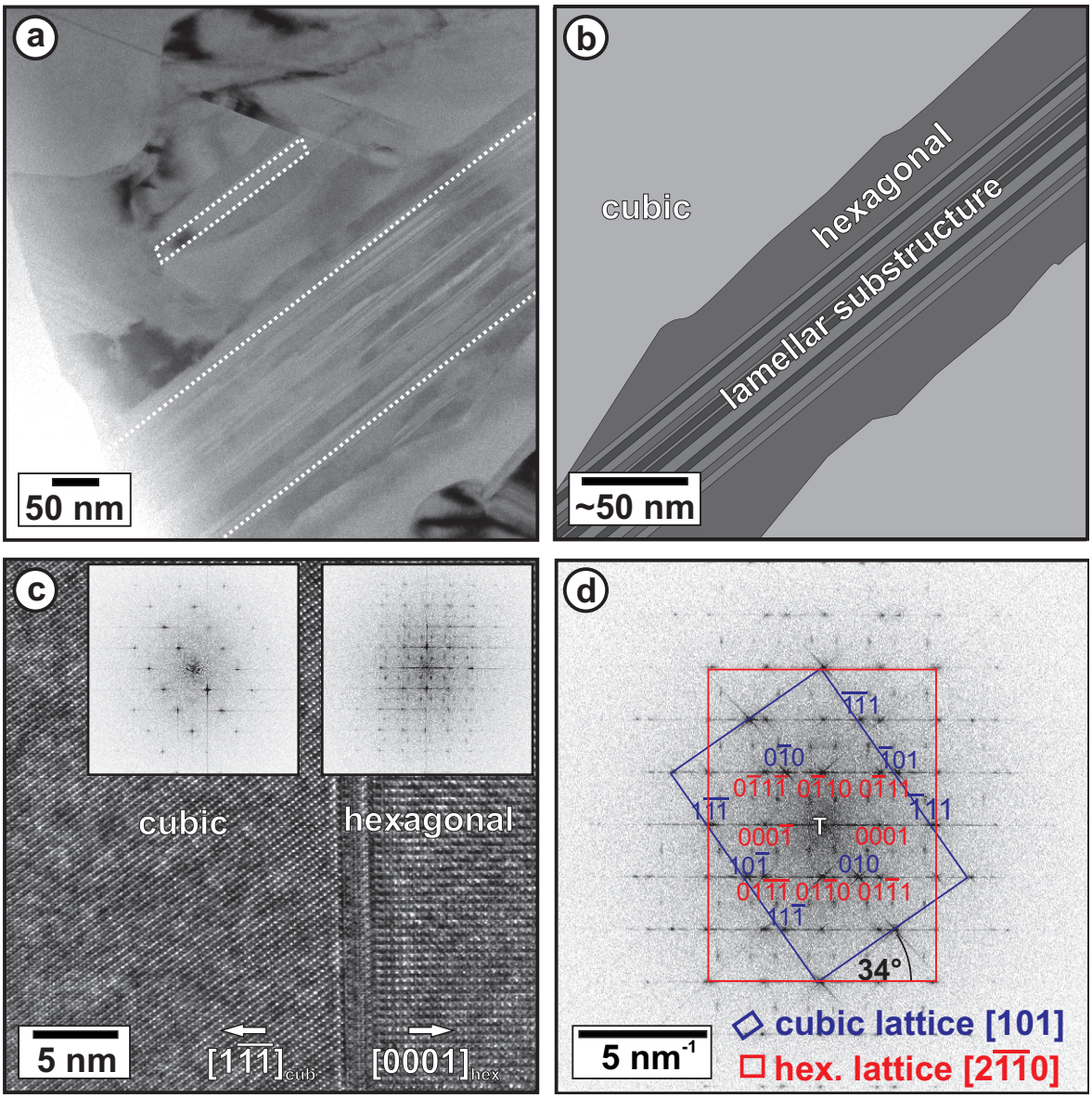

Figure 4.4: a) Overview bright-field TEM image of a sample after annealing at 700 °C for 100 h, b) scheme of the microstructure of plate-like regions, c) high-resolution TEM image of an interface in a plate-like region containing a cubic and a hexagonal lamella with corresponding diffractograms (insets), and d) diffractogram of the complete image shown in c). The cubic phase is observed along the [101]-zone axis with reflection indices indicated in blue. The hexagonal phase is viewed in [2$\bar{1}\bar{1}$0]-orientation (red). The rotation of 34 ° between the two lattices is emphasized by colored boxes.

alized in the scheme 4.4 b). The plate-like regions are often embedded in the hexagonal phase also shown in the scheme. The color scheme in Figure 4.4b) is chosen according to the typical image intensities of the cubic and hexagonal phases in SEM images.
The HRTEM image Figure 4.4c) reveals the structure of a plate-like region in detail. It shows the interface between two lamellae which are embedded in a larger region containing exclusively the hexagonal phase. The identification of the phases is accomplished by calculating the FOURIER-transform of the HRTEM image denoted as diffractogram in the following. The diffractogram of each lamella is presented in the insets of Figure 4.4c) which can be assigned to the cubic phase (left) and the hexagonal phase (right). Figure 4.4d) presents the diffractogram of the whole interface region shown in Figure 4.4c). Comparisons with simulations of the crystal structure [75] show that the cubic lattice is oriented in [101]-, and the hexagonal phase in $[2\bar{1}\bar{1}0]$-zone axis. The corresponding indexes are indicated in blue for the cubic phase and red for the hexagonal phase. The orientation relationship between the two phases can be derived from Figure 4.4d) which shows that the {111}-cubic and (0001)-hexagonal lattice planes are oriented parallel to each other. The projected elementary cells are rotated by an angle of 34 ° against each other as indicated by the colored boxes for the cubic (blue) and hexagonal lattice (red). The diffractogram of the hexagonal phase contains streaks along the [0001]-direction, which are related to planar defects (stacking faults) at the interface between cubic and hexagonal phase. Additional reflections are visible in the diffractogram of the hexagonal phase (Figure 4.4c)), which cannot be assigned to the defects at the interface. The additional reflections were also observed in other hexagonal regions and may occur due to damage of the phase during TEM sample preparation or by the electron beam.
A more detailed analysis of the crystal structure of thin lamellae in a plate-like region is performed by high-resolution HAADF STEM. The evaluation is explained on basis of the high-resolution HAADF STEM image presented in Figure 4.5a). The clarity of the contrast is impaired by amorphization and contamination of the sample due to electron-beam irradiation during the investigation in the transmission electron microscope and due to damage in the course of the Ar^+-ion etching process. The columns of the heavier A-site cations Ba and Sr show bright contrast in the image and are marked by large green dots in the model of Figure 4.5b). The lighter B-site cations (smaller blue dots) are not detected, because the electrons are scattered only with a small probability in large angles. B-site cations generate a weaker intensity on the HAADF segment of the detector. Furthermore a low SNR is caused by contamination and amorphization. A 2-dimensional model of the atomic stacking in the imaged region is presented in Figure 4.5b). In the perovskite structure, the O-anions form octahedrons (marked in red; see also Figure 2.2). Considering the 3-dimensional alignment, the octahedrons are corner-sharing in the cubic phase and face-sharing in the hexago-

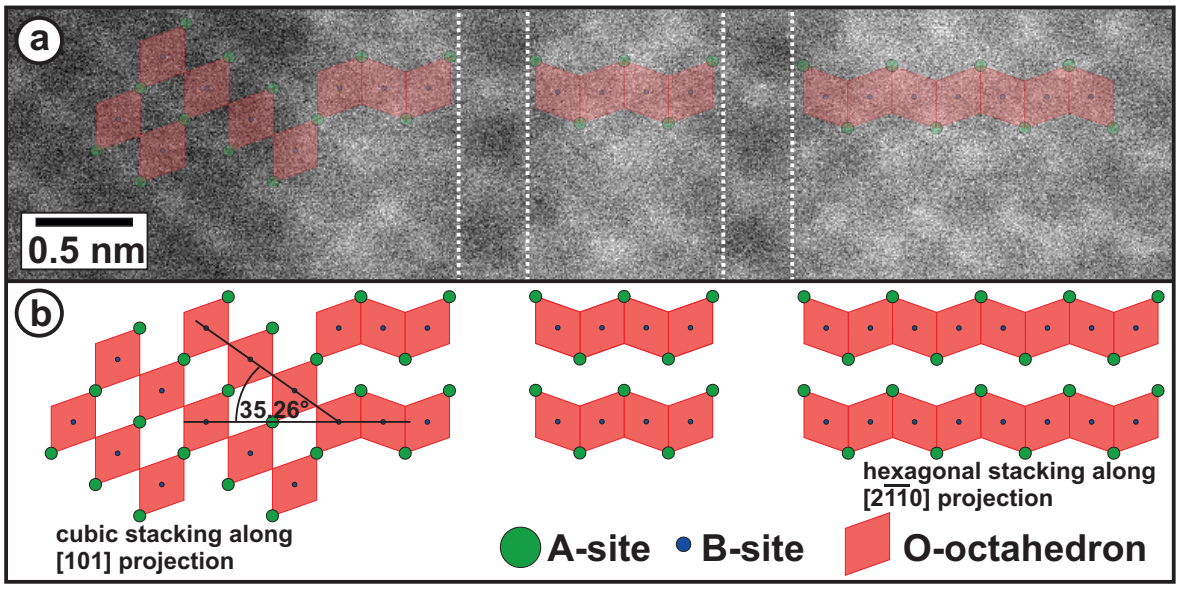

Figure 4.5: a) HAADF STEM image of thin lamellae in a plate-like region and b) corresponding structure models of cubic stacking (viewed along the [101]-projection) and hexagonal stacking (viewed along the [2$\bar{1}\bar{1}$0]-projection). The cubic phase consists of O-octahedrons (red) in corner-sharing configuration, while the hexagonal phase contains face-sharing octahedrons. Regions which cannot be assigned to any of the two phases are located inside the dashed boxes in a).

nal phase. In the scheme of Figure 4.5b) the alignment of the O-octahedrons therefore allows the distinction between cubic stacking viewed along the [101]-cubic direction and hexagonal stacking in [2$\bar{1}\bar{1}$0]-hexagonal direction. As indicated in Figure 4.5b), the cubic {010}-planes and hexagonal {01$\bar{1}$0}-planes form a theoretically calculated angle of 35.26 ° at the interface. This matches well with the rotation of 34 ° measured in the diffractogram in Figure 4.4d). It is noted that some regions, which are located inside the white dashed boxes in Figure 4.5a), can be assigned neither to the cubic nor the hexagonal phase. The investigation of these regions is subject of the following section 4.1.4.

4.1.4 BCO-type phases in BSCF

While most of the plate-like regions show stacking of cubic and hexagonal lamellae as described in section 4.1.3, the regions in Figure 4.5, which could be assigned to neither the cubic nor the hexagonal phase, give first hints that the model of the face- and corner-sharing octahedrons has to be supplemented. In the course of detailed HAADF STEM investigations, another phase with a different structure and composition was identified. Figure 4.6 shows high-resolution HAADF STEM images of a plate-like region in a sample, which was annealed at 800 °C, with the corresponding 2-dimensionally projected structure models presented in two different zone axes ([2$\bar{1}\bar{1}$0]-zone axis in Fig-

ures 4.6a)-c) and [10$\bar{1}$0]-zone axis in Figures 4.6d)-f)). Heavy A-cation columns appear with high intensity in the HAADF STEM images, while B-columns show a weaker intensity. The intensity of the B-site columns is not identical for all columns. As explained later, the density of some atomic sites along the projection is different. The projected structure models along the two zone axes are presented in Figures 4.6c),f) where A-columns are marked in green, B-columns in blue and O-columns in red.
The structure models [13, 29, 73] shown in Figures 4.6c),f) are derived from a phase described by Sun et al. [29] and David et al. [30] which is denoted in the following as BCO-type phase. The phase is similar to the R15 phase described by Efimov et al. [24]. The structural details of the phase will be explained in context with Figure 4.7. In the center of Figures 4.6a),d) a defect is observed which consists of 17 {111}-planes with cubic stacking order. The structure models displayed in Figures 4.6c),f) perfectly describe the experimental images apart from a 3 ° tilt in Figure 4.6e) compared to the structure model in Figure 4.6f). The tilt of 3 ° compared to the corresponding model was also determined for the zone-axis presented in Figure 4.6b). It can be explained either by drift during the image acquisition (the scan direction is tilted with respect to the presented image orientation) or by distortions due to a different chemical composition compared to the phase used for the simulation [29].
Figure 4.7 contains the projected structure of the BCO-type phase described by Sun et al. [29] along the [2$\bar{1}\bar{1}$0]-direction. It consists of a periodic arrangement of two {111}-planes of O-octahedrons with cubic stacking order and three planes with a CdI_2-type structure and two interface planes. The cubic planes are separated from the other planes by dashed black lines in Figure 4.7. The 3-dimensional CdI_2-type structure is characterized by an edge-sharing configuration of O-octahedrons. Sun et al. describe a whole series of different oxides ($Ba_{n+1}Co_nO_{3n+3}(Co_8O_8)$ (BCO)). The overall composition of the most common BCO-type phase in BSCF is $Ba_3Co_{10}O_{17}$ (n=2). The two cubic unit cells are composed of $Ba_2Co_2O_6$, leaving a composition of $BaCo_8O_{11}$ for the two interface planes and the CdI_2-plane. In contrast to the cubic and hexagonal structure, the CdI_2-plane violates the ABO_3 perovskite stoichiometry since it does not contain A-site cations. As the O-octahedrons are packed more densely in the CdI_2-plane, the corresponding B-site columns show a brighter contrast in Figures 4.6a)-e) compared to the other B-sites. Furthermore, the interface planes introduce additional B-sites (blue atomic sites beyond the octahedrons) located in tetrahedral gaps. It has to be noted that the BCO-type phase can also occur as lamella beside cubic and hexagonal lamellae in plate-like regions. Moreover, single CdI_2-type planes are occasionally found in plate-like regions with non-periodic arrangements of cubic and hexagonal stacking sequences, which explain regions with unidentified stacking in Figure 4.5b).
The model of the different alignments of the oxygen octahedrons describing the secondary phases in BSCF can, therefore, be expanded: corner-sharing octahedrons de-

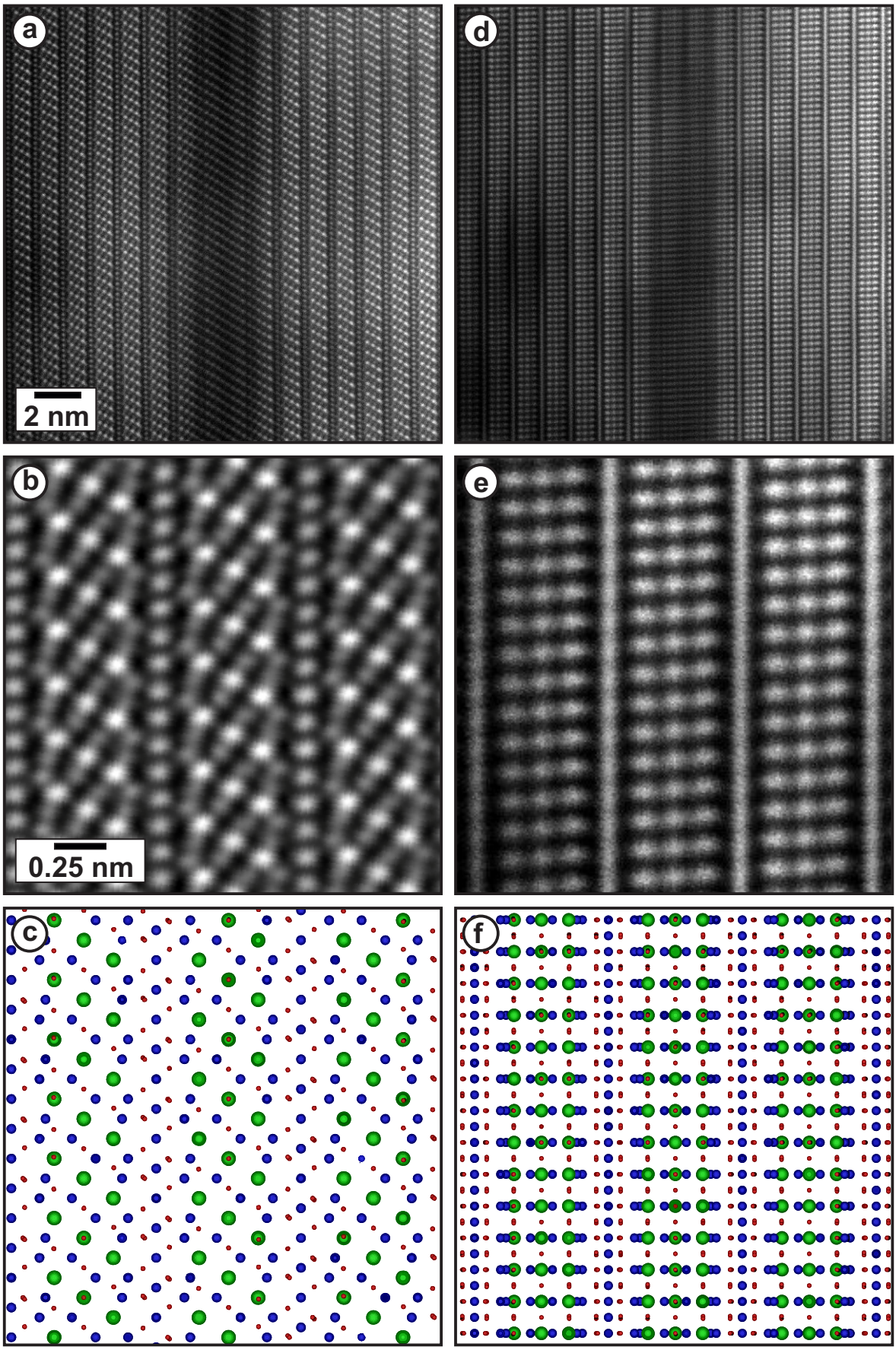

Figure 4.6: HAADF STEM micrographs and projected structure models of a sample after annealing at 800 °C along the a), b), c) $[2\bar{1}\bar{1}0]$-zone axis and d), e), f) $[10\bar{1}0]$-zone axis of the BCO-type phase. A-site cations are marked in green, B-site cations in blue and oxygen in red in c), f).

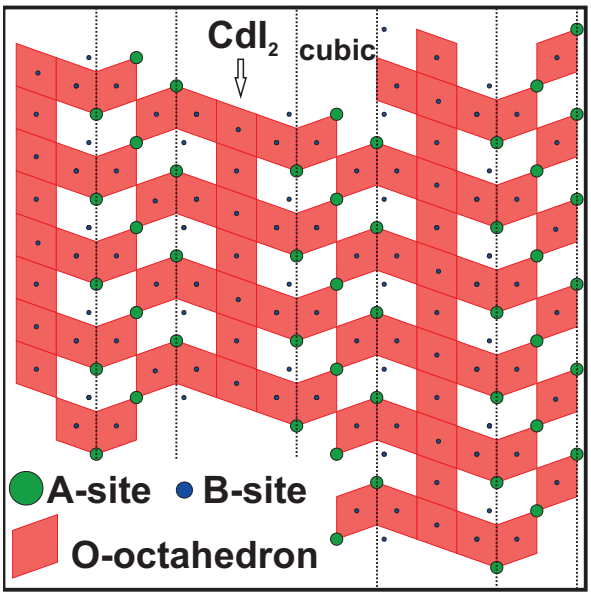

Figure 4.7: Projected structure of the BCO-type phase along the $[2\bar{1}\bar{1}0]$-direction containing a periodic arrangement of two {111}-planes with cubic stacking and three planes consisting of a plane with CdI_2-structure and two interface planes. The cubic planes are separated from the new stacking sequence by black dashed lines.

scribe the cubic perovskite phase, face-sharing octahedrons describe the hexagonal phase and the BCO-type phase is described by a periodic alignment of corner-sharing, face-sharing and edge-sharing octahedrons. Beside the well defined BCO structure following the formula $Ba_{n+1}Co_nO_{3n+3}Co_8O_8$ with n=2, any combination of lamellae of cubic, hexagonal and BCO-type phases (with different values for n) seems to be possible in the plate-like regions. As n describes the number of planes within cubic stacking in the BCO-type phase, lamellae with a large n contain broad cubic regions of several nanometer width as shown in Figures 4.6a),d). The chemical composition of the plate-like region is complex due to the different combinations which can occur by varying lamella thickness, and phase composition (cubic, hexagonal and BCO-type phase for different n). EDXS studies dealing with the composition of plate-like regions are presented in the next section 4.1.5.

4.1.5 Chemical composition of BSCF phases

The chemical compositions were determined by EDXS. The quantification of EDX spectra was performed on the basis of experimentally determined $k_{A,B}$ factors as outlined in section 3.7. Line-scans with one full EDX spectrum per pixel over regions with different phases were taken in the FEI Titan^3 80-300 microscope operated in STEM mode. The different phases were distinguished by electron diffraction. The chemical

phase	Ba	Sr	Co	Fe
$Ba_{0.5}Sr_{0.5}Co_{0.8}Fe_{0.2}O_{3-\delta}$ (BSCF)	25	25	40	10
cubic	26 ± 1	25.5 ± 1.5	40 ± 1.5	8.5 ± 1
hexagonal	30 ± 1	27 ± 1.5	42 ± 1	1 ± 0.5
BCO-type phase	21.5± 3	3 ± 1	67.5 ± 2.5	8 ± 1

Table 4.2: Concentrations of Ba, Sr, Co and Fe in at% for the different observed BSCF phases determined by EDXS compared to the nominal (intended) composition of cubic BSCF (first line). The errors are the standard deviations of the average values of up to 200 spectra recorded for the same phase.

compositions of the different phases are listed in Table 4.2 in at % after averaging up to 200 spectra for each phase. The errors correspond to the standard deviations of the average values. Like for all compositions presented in the present study, an additional systematic error of ± 3 at % has to be added to the statistical error (section 3.7).
All phases can be clearly distinguished by their chemical composition. The composition of the cubic phase only shows small deviations from the intended BSCF composition of $Ba_{0.5}Sr_{0.5}Co_{0.8}Fe_{0.2}O_{3-\delta}$ (first line in Table 4.2). The hexagonal phase is characterized by the absence of Fe. However, the chemical composition is close to the ABO_3 stoichiometry of the perovskite structure with a slight excess of A-site cations. The composition of the BCO-type phase strongly deviates from the other phases with respect to the A/B-ratio due to a strongly enriched Co-content and the absence of Sr. Plate-like regions consisting of lamellae of all three detected phases (cubic, hexagonal and BCO-type phase) show average chemical compositions which depend on the volume fraction of the different lamellar phases and show therefore significant composition variations (see Figure 4.9).
The absence of Sr and different A/B-ratio (compared to the perovskite structure) in the BCO-type phase agree well with the series of barium cobaltate phases described by Sun et al. [29], which correspond to a series of structures with the chemical formula $Ba_{n+1}Co_nO_{3n+3}(Co_8O_8)$. For n=2 the simulated cation positions well explain the HAADF STEM images presented in section 4.1.4. Nevertheless, the phase observed in this work does not exactly agree with the phase described by Sun et al. [29] because Fe is present. According to Sun et al. and David et al. [29, 30] the valence state of the Co-cations in BCO strongly differs on different Co-sites. As there are positions with low Co-valence states (+2.15 on average), these sites can also accommodate (larger) Fe-cations. The phase reported in this work therefore contains Fe and Co on B-sites. Figures 4.6e),f) in section 4.1.4 reveal a 3 ° tilt of rows of A- and B-cation sites compared to the originally proposed structure. This distortion may either result from the addition of Fe compared to pure BCO or from sample drift during the acquisition of the STEM image. The A/B-ratio for the BCO phase for n=2 is expected to be 1:3.3 com-

pared to 1:3 determined in this work. This may be partially caused by inaccuracies of the EDXS analyses but also by an intermixing of different members of the BCO series. If more than two cubic perovskite planes (n>2) are present in the stacking sequence, the A/B-ratio may be shifted towards 1:3. Such a region with larger number of cubic perovskite planes is imaged in Figures 4.6a) and 4.6d) where n=17 planes with cubic stacking are observed in the center of the image.

For the cobalt oxide crystallites observed by SEM and discussed in section 4.3.2, a ratio of Co:O = 52:48 was determined. This clearly matches with the CoO phase in agreement with the evaluation of diffraction patterns.

For a fast distinction of different phases, EDXS mappings were evaluated. For every pixel of a mapping, an X-ray spectrum is recorded and evaluated. In a subsequent step a false color image is derived. High color intensities correspond to a high concentration of the element under investigation. Image intensities are separately scaled for each element. Dark regions represent the lowest concentration but not necessarily the complete absence of the element. Figure 4.8a) shows a bright-field TEM image of BSCF annealed at 700 °C for 100 h containing cubic and hexagonal phase around a plate-like region. The inset (orange) is an EDXS mapping of the Co-concentration. The corresponding maps of Ba (green), Sr (blue), Fe (red) and O (yellow) are shown in Figure 4.8b).

One has to remark that for light elements like oxygen X-ray yield in the electron microscope is small. Due to the low SNR the EDXS technique is therefore not as precise as for the heavier cations. PCA filtering (see section 3.6) can reduce the noise in the signal (Figures 4.8c) and d)). The evaluation of filtered spectra, using the first 3 principal components for the back projection, indicates slight changes in the concentrations for different secondary phases. Especially for O-concentrations features suppressed by the enormous noise get visible due to the data processing. Concentration distributions presented in Figures 4.8c) and d) may not be interpreted quantitatively as the algorithm may influence intensity ratios of the X-ray signal.

The cubic regions show a constant intensity in the mapping corresponding to a stable chemical composition throughout the whole cubic crystallites. Hexagonal regions are mainly characterized by an increased Co-concentration compared to the cubic phase and a depletion of Fe. The regions are marked by a dashed white line in the Co and Fe mapping. The plate-like regions inside the grains of the hexagonal phase show, as expected, a much more complex behavior. As the BCO-type phase is characterized by the absence of Sr, corresponding regions can be located inside the plate-like region in the Sr map. These regions are marked by white arrows in Figure 4.8. The chemical composition of the plate-like regions will be shown in more detail in context with Figure 4.9. The O-concentration does not show a significant change over the whole mapping.

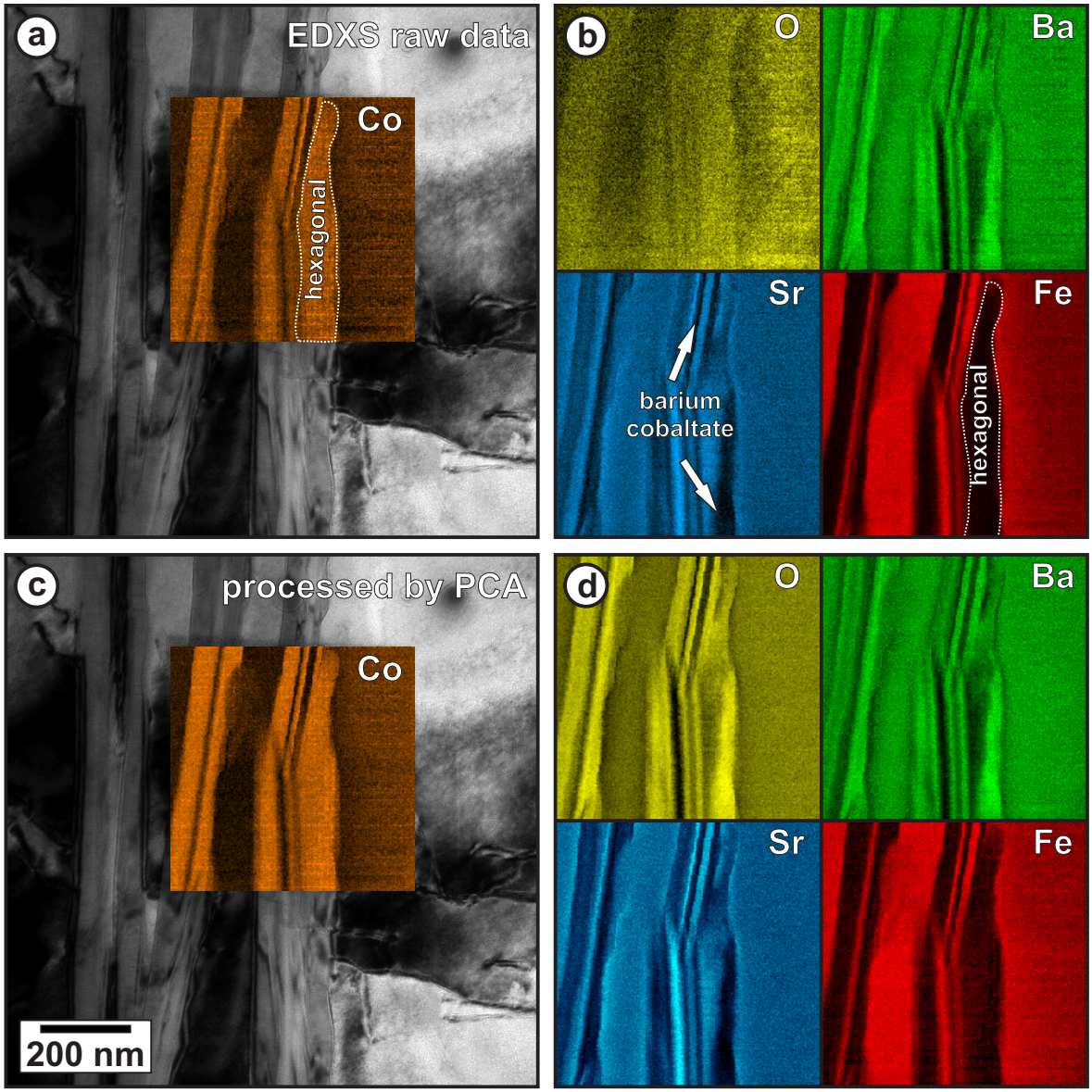

Figure 4.8: a) Bright-field TEM image of BSCF containing the cubic grains and crystallites of the hexagonal phase and a plate-like region. The inset is a qualitative EDXS-mapping of the Co-content in the corresponding sample region. Mappings of the other element concentrations are shown in b). The hexagonal phase is marked by a white-dashed line, the BCO-type phase characterized by the absence of Sr is marked by white arrows.

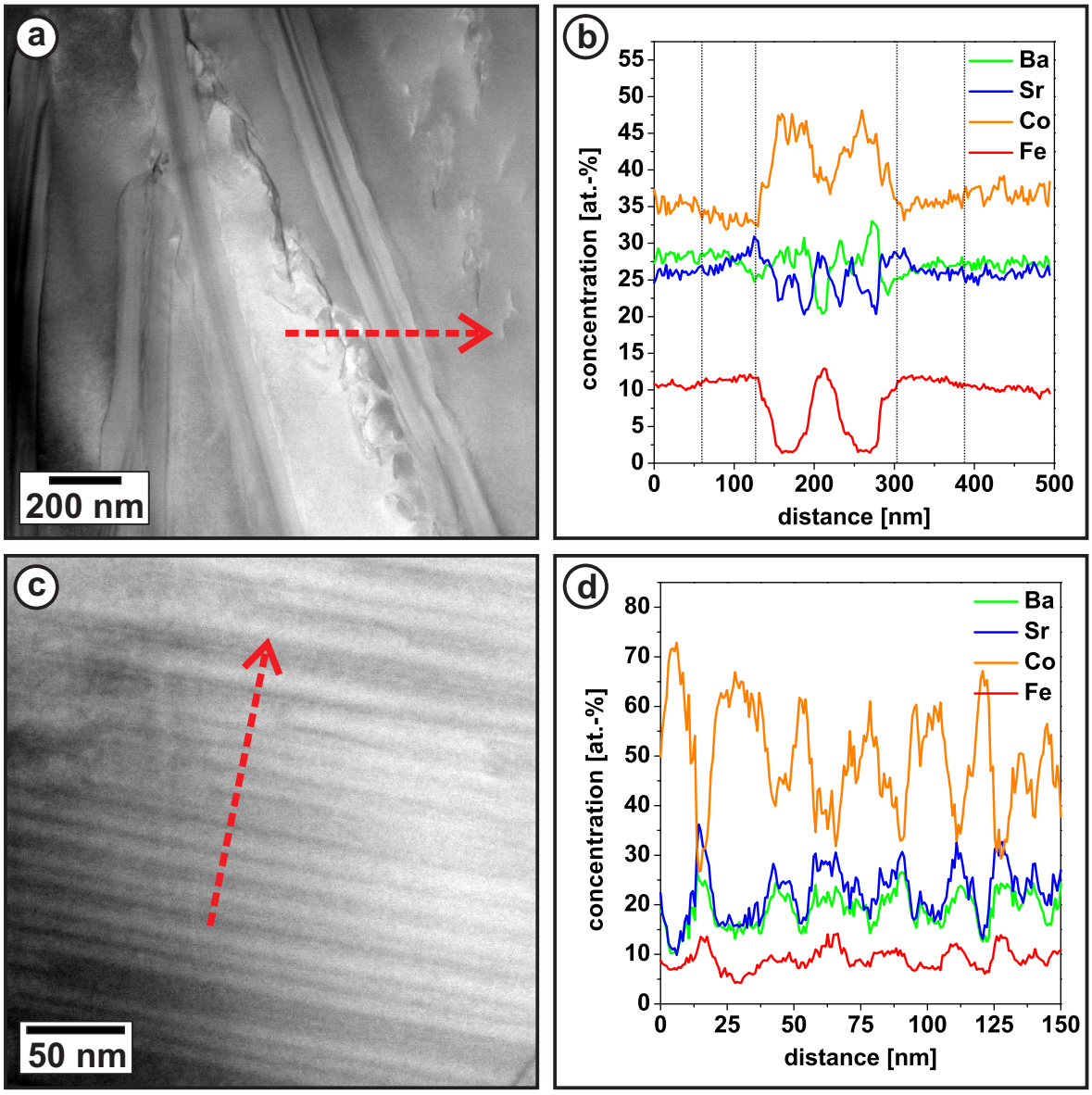

Figure 4.9: a), c) HAADF STEM images and b), d) corresponding EDXS linescans at positions indicated by dashed red arrows in the HAADF STEM images. Regions of the cubic phase inside the black lines in (b) contain composition gradients.

The complex chemical composition of a plate-like region, which consists of lamellae of cubic, hexagonal and BCO-type phases, is demonstrated in Figure 4.9. The HAADF STEM images in Figures 4.9a,c) were taken from a sample that was annealed at 700 °C for 100 h. The positions and acquisition directions of the EDXS linescans are indicated by red dashed arrows. Figure 4.9b) shows the composition of a plate-like region embedded in the cubic phase along the linescan in 4.9a). The hexagonal phase is characterized by the absence of Fe (red curve in Figure 4.9b)) and can directly be distinguished from the other phases. The composition of the region in the center of the linescan is determined by the average composition of thin lamellae of the different phases, which are not resolved. The linescan also demonstrates that the surrounding cubic phase accumulates the cations which are present in low concentration in the hexagonal phase (Fe) and BCO-type phase (Sr). Corresponding composition gradients are observed in the cubic phase in the regions inside the black dashed lines in Figure 4.9b). These regions are also depleted of Co-cations which are enriched in the hexagonal and BCO-type phase. Figure 4.9d) shows an EDXS linescan with high spatial resolution from a plate-like region. While a clear identification of the phases in the thin lamellae is still not possible for all regions due to the probe size in the range of 0.5-1 nm) and distance between individual measurements (0.75 nm). The significant oscillation of the Co-concentration and the overall low Fe-content indicates that the lamellae consist of the cubic, hexagonal and the BCO-type phase.
These results support the assumption that the plate-like regions are formed by thin lamellae of all three secondary phases. These regions therefore reflect the different possibilities of the stacking of the oxygen octahedrons. The thickness of the lamellae ranges from one single unit cell (0.46 nm) up to the micrometer scale.

4.1.6 Effect of doping

The effect of B-site doping of bulk BSCF material was also investigated in detail to explore whether the decomposition of the cubic BSCF phase can be prevented or, at least, retarded. Zirconium ($Ba_{0.5}Sr_{0.5}(Co_{0.8}Fe_{0.2})_{0.97}Zr_{0.03}O_{3-\delta}$ (BSCF3Zr)), scandium ($Ba_{0.5}Sr_{0.5}(Co_{0.8}Fe_{0.2})_{0.97}Sc_{0.03}O_{3-\delta}$ (BSCF3Sc)), and to the largest extent yttrium ($Ba_{0.5}Sr_{0.5}(Co_{0.8}Fe_{0.2})_{0.97}Y_{0.03}O_{3-\delta}$ (BSCF3Y)), were evaluated as dopants by Meffert [87] in the course of his diploma thesis. The dopants were chosen due to their fixed valence state and their ion radii (Table 2.1). The ion radius is a critical property for the stability of the BSCF phases [15]. For each dopant element and concentration a series of samples annealed at 700 °C, 800 °C, 900 °C and a sample without additional annealing (1000 °C) were investigated (see also Table 4.1). Like for the analysis of undoped material, SEM images of polished and etched samples were evaluated with regard to phase composition and microstructure as described in section 3.3.

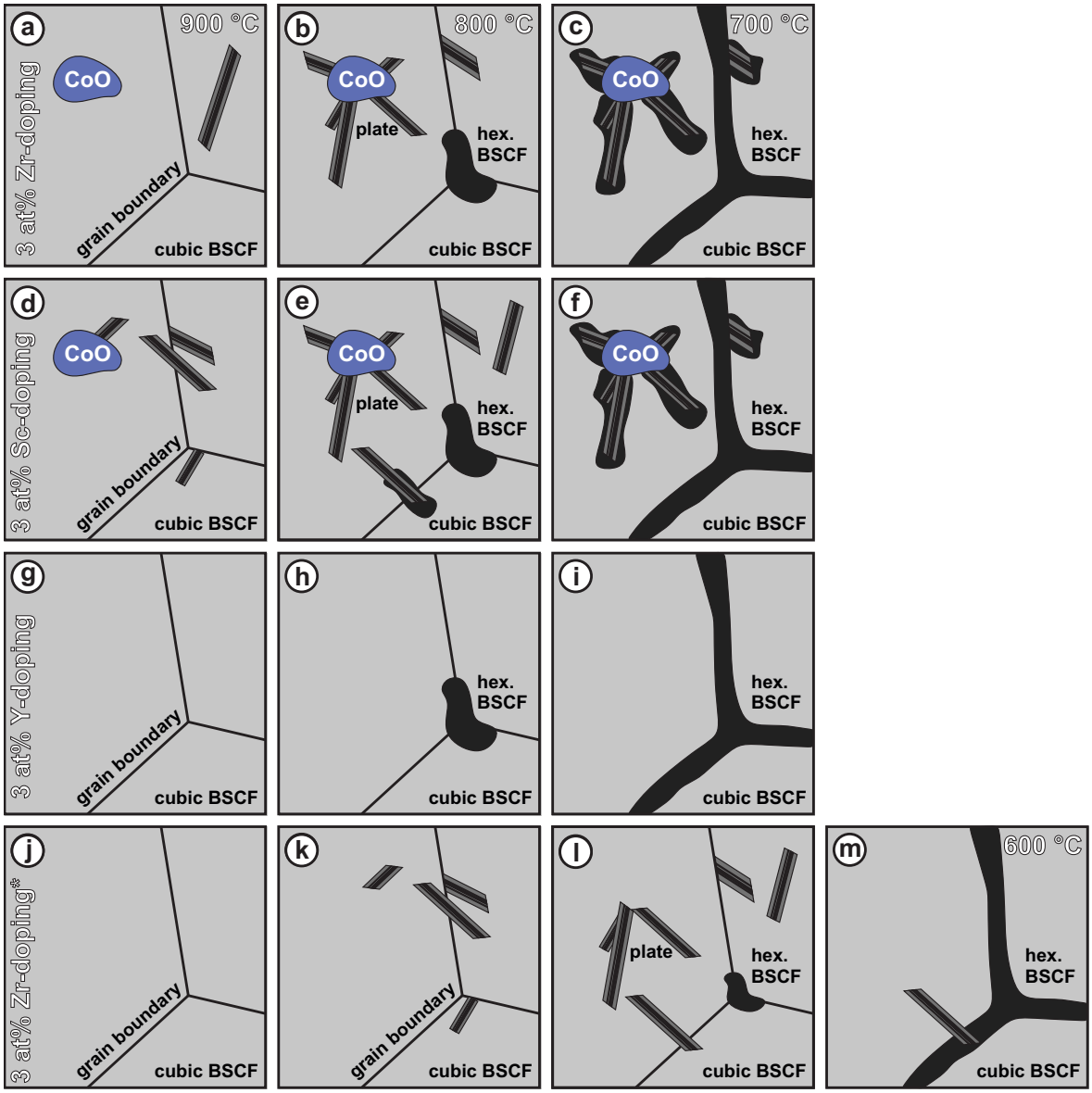

Figure 4.10: Schematic representation of phases in bulk BSCF in the temperature range 600 °C-900 °C for (a)-c)) Zr-, (d)-f)) Sc- and (g)-i)) Y-doped samples. Zr- and Sc-doped samples do not show a significant change compared to undoped BSCF, while Y-doping prevents the formation of plate-like regions in the whole temperature range. j)-m) Zr-doped samples prepared by spray pyrolysis show a significant effect on secondary phase formation.

Figure 4.10 presents a schematic overview of the observed phases for 3 % B-site doping. For Zr- and Sc- doping the decomposition after anneling is comparable to pure BSCF. The formation of plate-like regions was observed at temperatures at and below 900 °C and the formation of the hexagonal phase at temperatures below 840 °C (see section 4.1.2). For Y-doping a significant improvement of the stability of the cubic phase is observed, because the formation of plate-like regions is strongly suppressed. The transition to the hexagonal phase apparently is not suppressed by Y-doping. It is also noted that CoO precipitates are missing.
Figures 4.10j)-m) show the effect of Zr-doping for a series of samples that was fabricated differently. In this case, BSCF starting powders were prepared by spray pyrolysis at the University of Trondheim, Norway. Bulk material was prepared and annealed at the University of Twente, Netherlands (Prof. Dr. H.J.M. Bouwmeester and Dr. C.-Y. Yoo) [43]. A significant effect of Zr-doping was detected, leading to the conclusion that the Zr-doping of the in-house samples failed (Zr is not solved in the BSCF lattice). The effect of Zr-doping in the samples prepared by spray pyrolysis can be summarized as a shift of the formation temperature of secondary phases by about 100 °C towards lower temperatures. Both Y- and Zr- doped samples with improved stability have in common that the formation of CoO precipitates is suppressed. While the reasons for a stabilization of the perovskite by Y-doping were investigated by TEM in detail in the work of Meffert [87] and summarized in this section, the effect of Zr-doping is an interesting topic for future studies.
As the Sc-doped samples do not show an improvement of the stability of the cubic phase, EELS measurements were performed to check whether Sc can be detected. For this purpose EEL spectra of the Sc-$L_{2,3}$ white-lines were recorded (edge onsets 402 eV and 407 eV) [87]. The Sc-edge is clearly visible in the high-loss spectra of cubic regions. This can be considered as evidence that the Sc-cations are solved in the lattice. Therefore, any problems arising from the production process of the material can be excluded as reason for the instability of the cubic phase. Sc does obviously not stabilize the cubic BSCF phase.
To further investigate the positive effect of Y-doping in the BSCF lattice, EDXS-mappings were recorded to resolve the cation distribution in a sample region composed of both, the cubic and hexagonal phase after annealing for 125 h at 700 °C. Figure 4.11a) shows a HAADF STEM image of a cubic region containing a grain boundary which is decorated with hexagonal phase. The EDX spectra were filtered using the PCA algorithm introduced in section 3.6 to reduce noise. For EDXS, this method can only be applied for qualitative evaluations, because the total intensities of the X-ray lines in the spectra might be slightly changed due to the filtering. As more features occur in the EDX spectra compared to EEL spectra, a relatively large number of principal components in the order of 10 was used for the reconstruction. Figures 4.11b)-f)

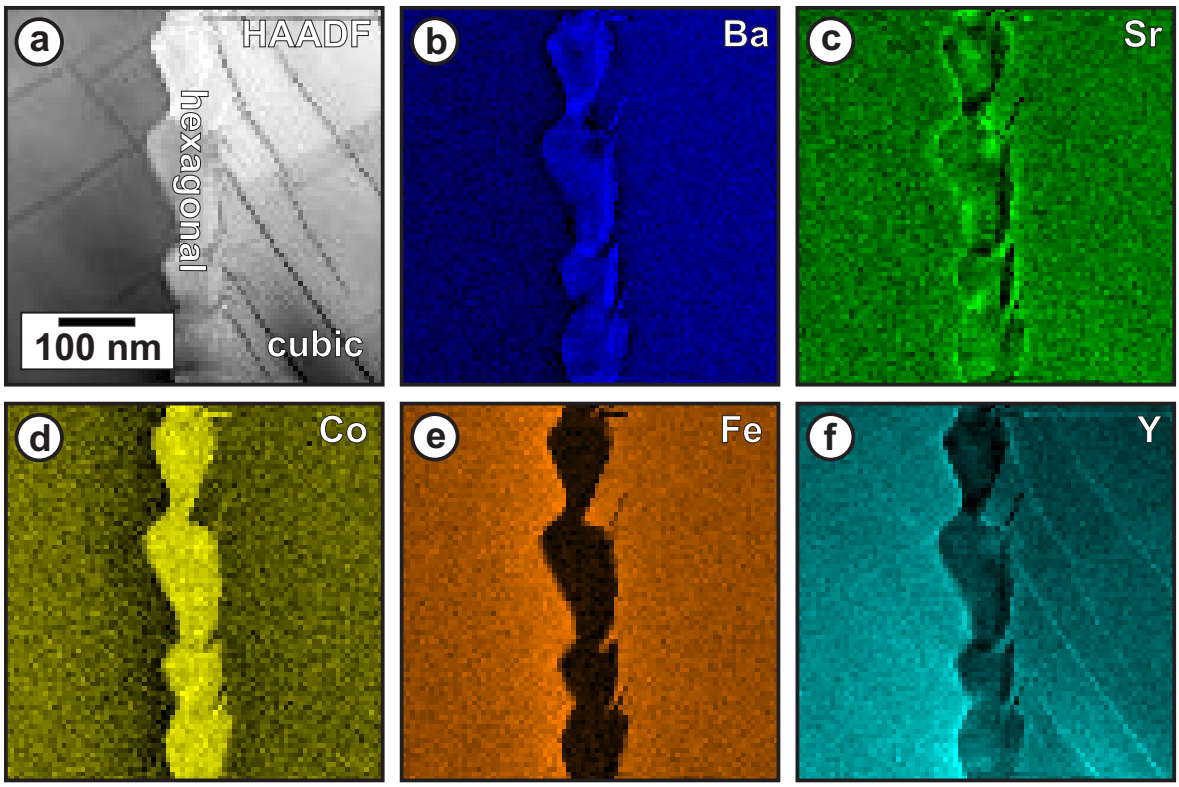

Figure 4.11: a) HAADF STEM image of the investigated sample region of an Y-doped sample after annealing at 700 °C for 125 h. b)-f) Mappings of the cation distribution [87]. The HAADF STEM image and the elemental mappings show a hexagonal region embedded in the cubic BSCF phase.

show the cation distribution in BSCF3Y. While for Ba, Sr, Co and Fe the distribution is as expected (Fe-depletion and Co-enrichment in hexagonal phase), Figure 4.11f) qualitatively demonstrates a lower Y-concentration in the hexagonal phase. This indicates that the formation of secondary phases may be suppressed because Y first has to diffuse out of the cubic phase. The formation of plate-like regions containing a significant amount of hexagonal phase therefore may also be suppressed inside cubic grains. Further effects leading to stabilization of BSCF3Y are discussed in section 4.3.5.

The formation of the hexagonal phase in BSCF3Y was investigated by SEM in the temperature range of 700 °C-800 °C. Due to the absence of plate-like regions, BSCF3Y is suited to study the nucleation of the hexagonal phase at grain boundaries. Figure 4.12 shows SEM images after 100 h of annealing at a) 700 °C, b) 730 °C, c) 760 °C, and d) 800 °C. At lower temperatures (700 °C-730 °C) the hexagonal phase decorates the whole grain boundaries. In contrast, nucleation of the hexagonal phase occurs mainly at triple points of the grain boundaries at 800 °C. At temperatures higher than 840 °C the material is purely cubic. Grain boundaries which are not decorated with hexagonal phase are marked by white dashed lines in Figures 4.12c) and d).

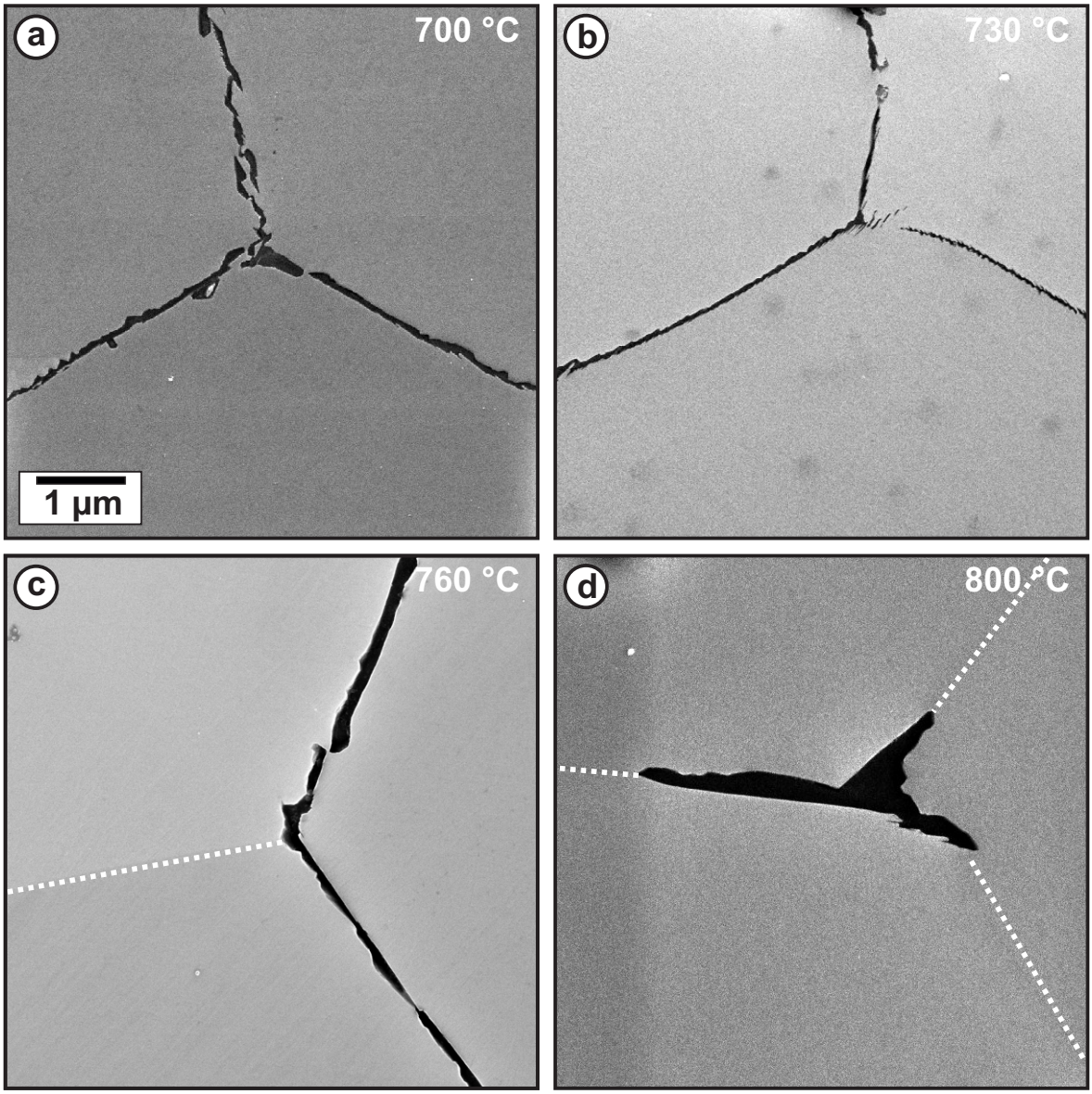

Figure 4.12: Formation of the hexagonal phase in dependence of the temperature after annealing for 100 h at a) 700 °C, b) 730 °C, c) 760 °C and d) 800 °C [87].

4.1.7 Electrical characterization

The effect of annealing and doping on the performance of BSCF as membrane material was tested by conductivity measurements at the IWE. According to equation 2.2 both electron and ionic conductivity contribute to the oxygen flux through a membrane. While the determination of the ionic conductivity requires a complex permeation measurement setup, the electric conductivity can be easily determined.

Figure 4.13 shows conductivity data in dependence of time and temperature for undoped, Zr-, Y- and Sc-doped BSCF. The measurement was conducted in a chamber furnace. Starting at 900 °C the temperature was decreased after 700 h to 800 °C and after 1500 h to 700 °C. A current is applied using a Keithley 224 programmable current

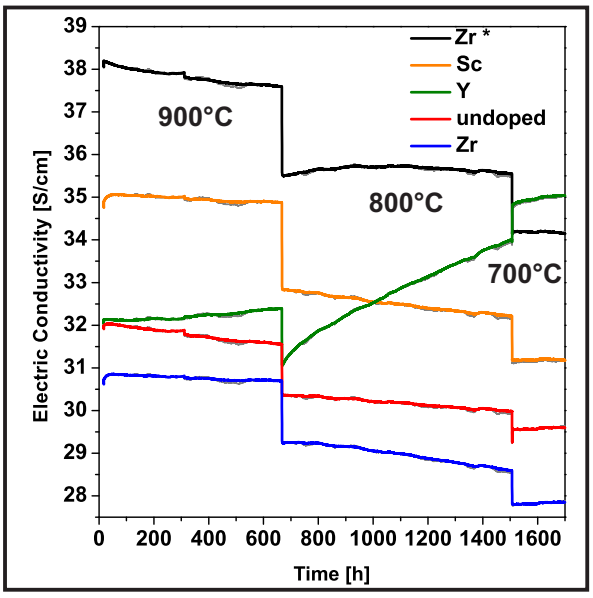

Figure 4.13: Time and temperature depending electric conductivity of doped and undoped BSCF bulk material. (*) Zr-doped sample prepared by spray pyrolysis provided by University of Twente, Netherlands [43].

source (Keithley Instruments Inc., Cleveland, Ohio, USA). The voltage drop for each samples was determined using a Keithley 2000 multimeter (Keithley Instruments Inc.). The measurement setup is comparable to the setup described by Niedrig et al. [34]. The conductivity degradation of undoped BSCF shows the same long-term oxygen flux degradation as reported elsewhere [12, 111]. At all temperatures under investigation (700 °C-900 °C) degradation was observed. An influence of the electric current on the degradation was excluded by additional test samples which were not measured sequentially. Stability of the electric conductivity therefore is a good indicator for a stable oxygen conductivity.

As the measurement was conducted at ambient air, and the conductivity depends on the oxygen concentration gradient (equation 2.2), the data depends on the ambient air pressure. The primary data (gray curves under the colored curves) was corrected using air pressure data obtained from Institute for Meteorology and Climate Research (IMK), KIT, Germany. Different offsets of the curves may stem from an overall different conductivity, but are also influenced by the quality of the electrical contacts, sample dimensions and pore concentration. For this reason only the time dependent behavior is suited for the interpretation of differences between the samples.

Sc-doping shows a similar degradation behavior as undoped BSCF as expected from the development of the phase composition after annealing (section 4.1.6). For Zr-doping the preparation route seems to influence the stability. While the Zr-bulk material of this work also degrades similarly to undoped BSCF, the Zr-doped sample from the University of Trondheim, Norway prepared by spray pyrolysis (data published by

Yakovlev et al. [43]) shows less or a delayed degradation at 800 °C. Y-doped samples are most promising, with an improvement of the conductivity in the whole temperature range for the entire time period. The significant improvements of the electric conductivity are even observed at low temperature where the mobility of oxygen ions is decreased. This suggests an additional effect decoupled from the ionic conductivity.

4.1.8 Co-valence in different BSCF phases

Based on the evaluation methods introduced in section 3.6 and 3.8, the valence state of Co was monitored in different secondary phases of BSCF and BSCF3Y. It was observed that doping does not influence the Co-valence state in cubic BSCF within the limits of accuracy of our evaluation method. Therefore, results from both doped and undoped samples are presented in this subsection.

Figure 4.14a) shows a mapping of the Co-valence illustrated in false colors of a sample annealed for 115 h at 760 °C. The region contains the cubic and hexagonal phase (Figure 4.14b)). For each image pixel an EEL spectrum was filtered and evaluated according to the procedure described in section 3.6. For the back projection the first 2 principal components were used resulting in the noise-reduced dataset. The white-line distance was assigned to a valence state according to the diagram shown in Figure 3.8 using the linear fit to the reference data. One can clearly distinguish the two phases by different average Co-valences. For the cubic BSCF phase, an average valence state of 2.0+ (± 0.3) (blue color) was determined. The hexagonal phase is characterized by a higher valence of 2.6+ (± 0.3) in average (yellow color). The errors comprise the standard deviation of the average value in each phase and the estimated systematic error due to the linear interpolation of the reference data. The standard deviation was calculated to be ± 0.2 for the cubic phase and $< \pm 0.1$ for the hexagonal phase. In contrast, the systematic error for high valences as in the hexagonal phase is larger (± 0.2) than for lower valences as in the cubic phase (± 0.1) leading to the same total error of ± 0.3. The reason for the smaller standard deviation in the hexagonal phase is its higher Co-concentration, with higher white-line intensities and better signal quality. The interface between both phases shows a steep change of the Co-valence state. This is an additional indication that the linear assignment of the white-line distance to the valence state does not lead to artifacts.

Figure 4.15 shows the combination of both, an EDXS composition profile b) and an EELS linescan c) of a sample which was annealed for 100 h at 650 °C. The sample region which was investigated is indicated in the HAADF STEM image Figure 4.15a) by a red dashed arrow. The chemical composition was evaluated according to the procedure described in section 3.7 and 4.1.5. Regions with a low Fe-content are characteristic for the hexagonal phase. The Co-valence state in hexagonal region is 2.8+ (± 0.2), compared

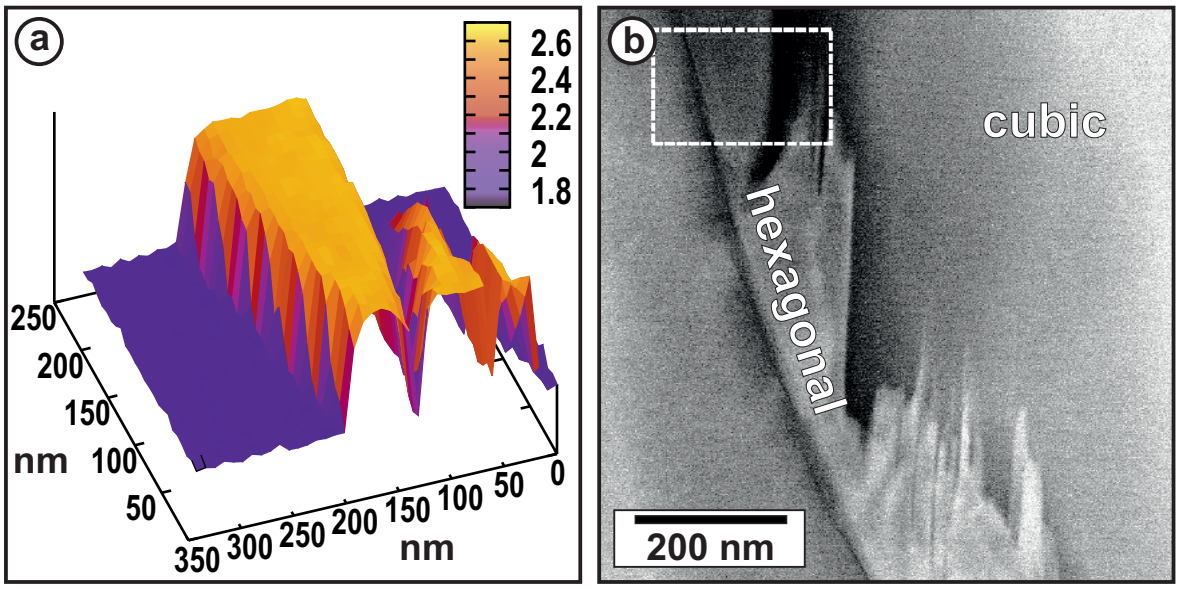

Figure 4.14: a) Mapping of the Co-valence state of the cubic and hexagonal phase illustrated in false colors. The region of the measurement is indicated by the dashed box in the HAADF STEM image b). The sample was annealed for 115 h at 760 °C.

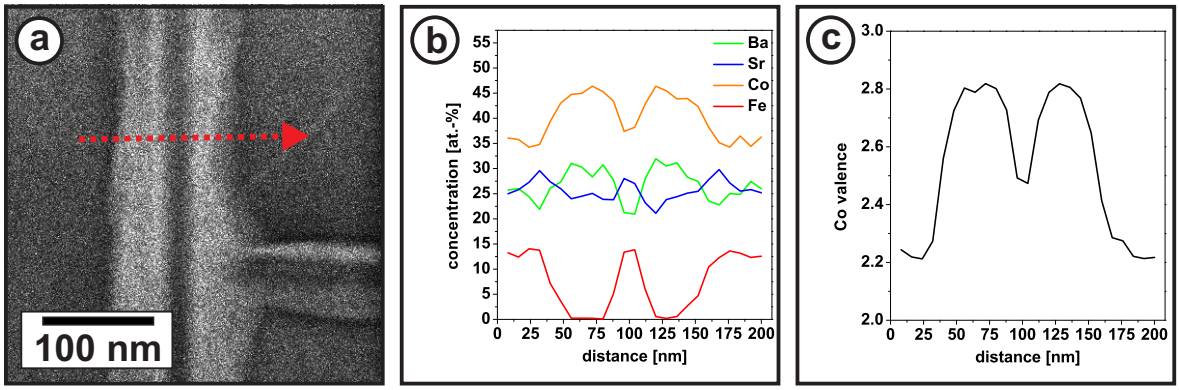

Figure 4.15: a) HAADF STEM image of a BSCF sample annealed for 100 h at 650 °C with the position of EDXS and EELS line profiles indicated by the red arrow, b) chemical composition and c) Co-valence stete. The hexagonal phase is indicated by the absence of Fe.

to 2.2+ ($\pm$ 0.2) for cubic regions. The accuracy of single measurements is increased compared to Figure 4.14a) due to an improved SNR. The phase between the two hexagonal regions cannot be identified. The composition of the sample region between the hexagonal lamellae indicates the presence of the cubic phase. Microstructural considerations would rather suggest a plate-like region. However, the Co-valence state of 2.5+ is higher in the thin lamella than in the embedding cubic phase. This effect could be related to the distance of 8 nm between individual EEL spectra which is not small enough to resolve the valence state in thin lamella with sufficient accuracy.
The Co-valences determined from the mapping (Figure 4.14) are by 0.2 lower than the values in the linescan (Figure 4.15). This can be partially attributed to the annealing temperature (760 °C compared to 650 °C). According to Arnold et al. [28] and Kriegel et al. [93] a lower overall valence state is expected at 760 °C, which is estimated to amount up to 0.1. Moreover, oxygen loss due to electron irradiation during the long acquisition time for the EELS map cannot be completely excluded, which would result in a reduced Co-valence state.
The influence of the Co-valence state on the stability of the material system is discussed in section 4.3. The limitations of the white-line distance based assignment of the Co-valence state are discussed in section 3.8.3.

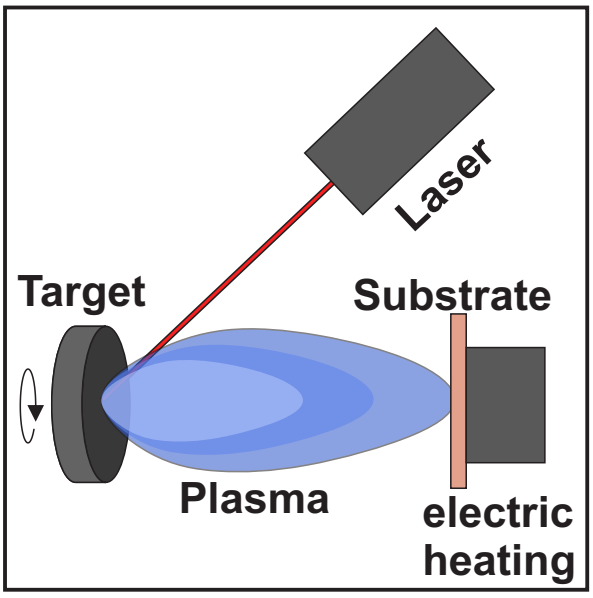

Figure 4.16: Scheme of the PLD process.

4.2 BSCF thin-films

4.2.1 Thin-film fabrication

BSCF thin-films were prepared by both, Pulsed Laser Deposition (PLD) and Electron Beam Physical Vapor Deposition (EBPVD) on $NdGaO_3$ (NGO) (LSC coated samples) and LSAT (samples without LSC coating) substrates. Both substrates are suitable for BSCF epitaxial layers. NGO was chosen because of its isolating character, which is important for measurements of the electric conductivity of the thin-films.
Figure 4.16 shows a scheme of the PLD deposition process. This method was chosen because of its potential to deposit stoichiometric material even of complex material systems. A high-energy laser beam is focused on a sintered target of the desired material. The evaporation of the material causes a plasma plume. The heated substrate is positioned in the center of the plume. As the laser is operated in a pulsed mode, the number of the pulses is proportional to the layer thickness. The target is rotating to achieve uniform abrasion of the material and to cancel potential chemical impurities. The substrate is heated electrically to assist epitaxial crystal growth. Important parameters during deposition are laser energy E_L, laser repetition frequency F_L, number of depositions (laser pulses) n, substrate temperature t_S, oxygen partial pressure during deposition $P_{O_2,d}$ and oxygen partial pressure during cool down $P_{O_2,c}$. The best values for BSCF and doped BSCF were determined by checking the epitaxial layer quality (especially mosaic spread) after deposition by XRD. For a substrate temperature of 700 °C a FWHM of 0.07 ° of the Bragg reflections was achieved indicating an acceptable quality of the epitaxial growth. The starting deposition parameters were taken

from previous work by Burriel et al. [112]. The deposition parameters are listed in Table 4.3.
The growth rate was determined by TEM on cross-section samples to be 0.12 nm per pulse. Some uncoated samples were annealed at temperatures of 650 °C, 700 °C, 800 °C and 900 °C to study the decomposition under application-relevant conditions and to investigate the influence of the small film thickness on the formation of secondary phases. Some PLD samples were coated with a nano-crystalline, nano-porous $La_{0.6}Sr_{0.4}CoO_{3-\delta}$ (LSC64) film. The layers were deposited using a sol-gel-based technique by first spin-coating the LSC sol (1-10 % cations in stoichiometric composition solved in propanoic acid). The rotation rate of the coater was controlled to 2000 rpm-5000 rpm for 90 s depending on the desired film thickness (50-120 nm) LSC sols with 5-10 % cation concentration were found to yield best results in terms of homogenity of the coating. In a subsequent step, baking at 170 °C for 10 min in air was performed to remove the organic solvent. The samples were then annealed in air in a ceramic tube furnace up to 700 °C at 3 K/min directly followed by cooling at the same rate to initiate the growth of nano crystals. The thermal history of LSC-coated samples can therefore be summarized as: 1.8 h annealing at temperatures > 500 °C, thereof 0.9 h at temperatures > 600 °C.
LSC-coated samples were also annealed in the course of electric measurements (compare to section 4.1.7). An annealing in air was applied according to a programmed sequence which can be summarized by: 19.4 h annealing at temperatures > 500 °C, thereof 11.2 h annealing at temperatures > 600 °C. The annealing procedures for LSC-coated and uncoated samples are summarized in Figure 4.17.
Figure 4.17a) shows a typical temperature characteristic of a long-term annealing treatment for 100 h at 700 °C, which is similar to the annealing of bulk samples (section 4.1.1). Quenching was not possible for thin-films because of possible delamination from the substrate. Figure 4.17b) shows the typical temperature history of a sample due to LSC coating. As this temperature treatment is necessary for material production and cannot be avoided, samples treated only by this short annealing step are considered as not annealed. Samples which were treated according to Figure 4.17c) are considered as annealed in the next chapters.

4.2.2 Phase determination and composition

The PLD layers were investigated by TEM and SEM as-prepared to control coating quality and phase purity. Figures 4.18a,b) shows an overview and high-resolution cross-section image of a BSCF layer on an LSAT substrate. No hints of secondary phases were detected. Epitaxial PLD layers are distorted at the interface due to the lattice parameter mismatch between LSAT substrate (0.387 nm) and BSCF (0.3983 nm). The interface region is marked by the white dashed line in Figure 4.18. The layer thickness

parameter	value
E_L	450 mJ
F_L	5 Hz
n	1000
t_S	700 °C
$P_{O_2,d}$	0.3 mBar
$P_{O_2,c}$	0.5 Bar

Table 4.3: Deposition parameters for PLD process.

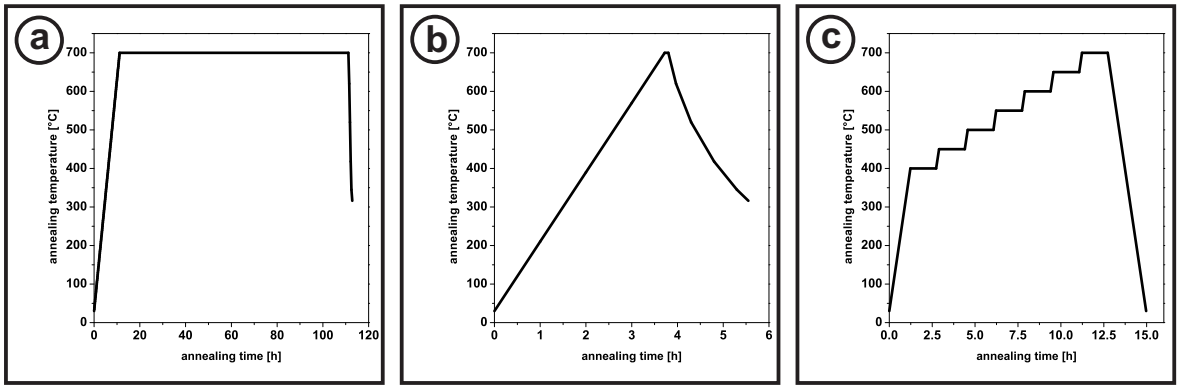

Figure 4.17: Annealing procedures for (LSC-coated) PLD samples. a) Long-term annealing of uncoated PLD samples at 700 °C, b) annealing in the course of LSC coating denoted as not annealed in the following, c) annealing in the course of electric measurements. One has to consider the different time scales. Annealing was conducted in ambient air.

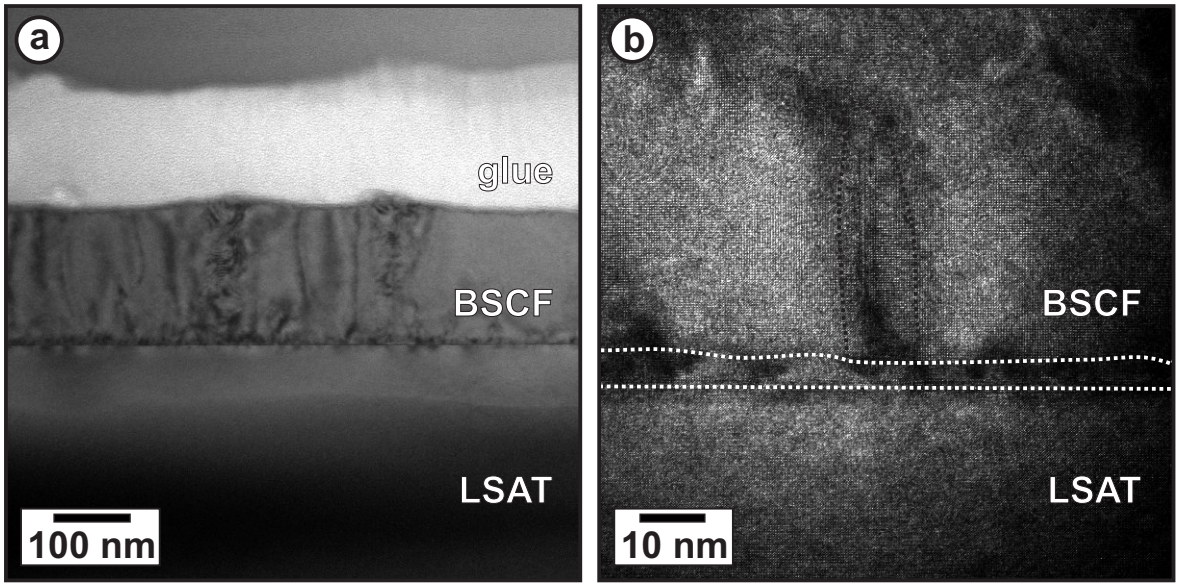

Figure 4.18: a) Overview bright-field and b) high-resolution TEM image of a BSCF PLD layer on LSAT. The dashed lines in b) mark a defective interface region between the substrate and the epitaxial layers.

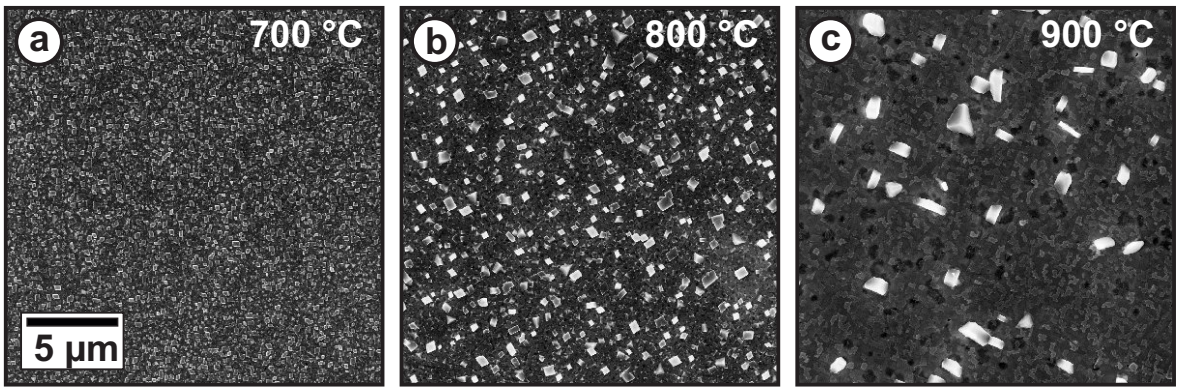

Figure 4.19: SEM plan-view images of PLD layers after annealing for 100 h at a) 700 °C, b) 800 °C and c) 900 °C.

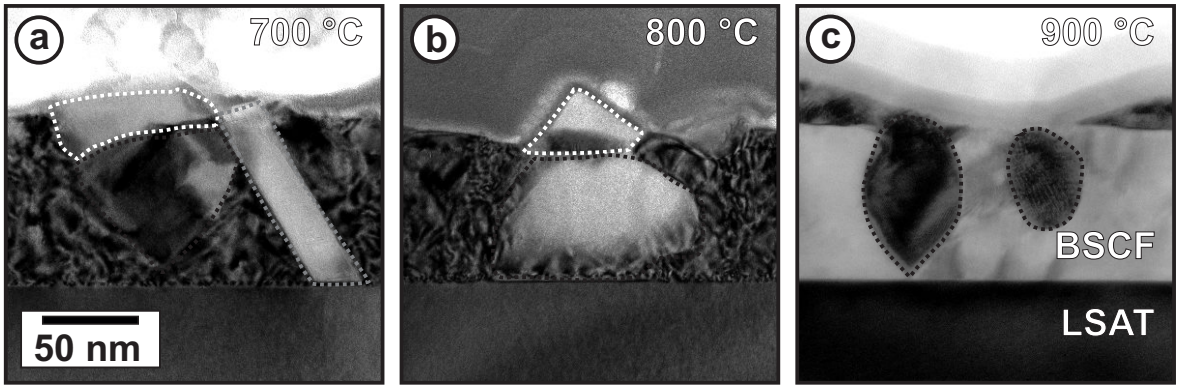

Figure 4.20: TEM bright-field cross-section images of PLD thin-films after 100 h of annealing at a) 700 °C, b) 800 °C and c) 900 °C.

was measured to be about 150 nm. Some distortions extend the whole layer thickness (marked by the black dashed line in Figure 4.18) and indicate slight orientation variations in the epitaxial layer leading to the mosaic spread which was measured to be 0.07 ° by XRD for as-prepared samples.

To investigate destabilizing surface effects and potential stabilizing effect of the epitaxial stress on phase stability of the BSCF epitaxial layers, the samples were annealed analogous to the bulk samples at 650 °C, 700 °C, 800 °C and 900 °C for 100 h in a ceramic tube furnace in ambient air (Figure 4.17a)). SEM plan-view images (Figure 4.19) show secondary phases at the surface over the whole temperature range 650 °C-900 °C. The size of the crystallites increases with annealing temperature. In contrast to the BSCF bulk material, the volume fraction of secondary phases does not decline with increasing annealing temperature. EDXS measurements in the scanning electron microscope yield insufficient results because of strong signal from the substrate. The secondary phases were investigated in detail by TEM including EDXS on cross-section samples.

Figure 4.20 shows a compilation of TEM images of the thin-films after annealing (700 °C-900 °C) with secondary phases. Plate-like regions (marked by a gray dashed

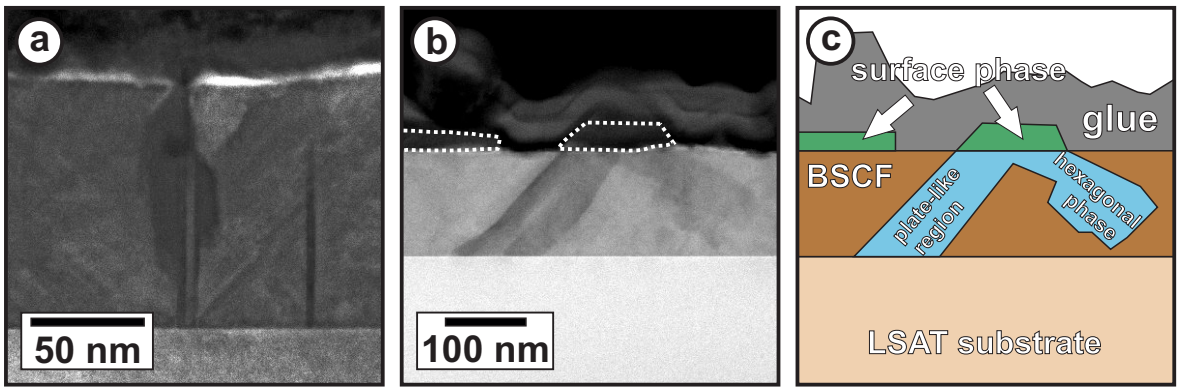

Figure 4.21: HAADF STEM micrographs of cross-sections of PLD thin-films annealed for 100 h at a) 650 °C and b) 700 °C with corresponding scheme of the microstructure c).

line in Figure 4.20a)) were observed and investigated in detail. They grow preferentially perpendicular to the surface or under an angle of 45° or 60°, indicating a specific orientation relation with respect to the cubic phase which was also found for plate-like regions in bulk samples [87]. The spherical-shaped crystallites (black dashed lines) were investigated by SAED and compared to simulated CoO [113] and Co_3O_4 [114] DEBYE-SCHERRER diffraction pattern using the Gatan Digital Micrograph plugin PASAD-tools v0.1 [115] and JEMS. The secondary phase in this sample series does not fit to common Co-oxides and could not be identified by electron diffraction. Furthermore, it also occurs in samples annealed at temperatures above 900 °C. The surface phase (white dashed line in Figures 4.20a,b)) corresponds to the surface phase also detected by SEM investigations (Figure 4.19).

HAADF STEM images of samples annealed at low temperature 650 °C (Figure 4.21a)) and 700 °C (Figure 4.21b)) show dark contrast around plate-like regions corresponding to a depletion of heavy elements. EDXS investigations of the sample regions in Figures 4.21a)-b) (data not shown) reveal both, an increasing amount of Co and a depletion of Fe in the regions with darker contrast, which is indication for the formation of the hexagonal phase also reported for bulk BSCF. The dark contrast cannot be explained by a change of the mean atomic number in these regions. The hexagonal phase typically appears with a higher image intensity in HAADF STEM images (compare to Figures 4.9a), 4.14b) and 4.15a)) due to a slightly increased amount of heavy A-site cations. In the present case, the darker contrast could be related to a change of the sample thickness due to different Ar^+-etching rates during sample preparation.

Figure 4.21c) presents a schematic overview of the phases in the annealed thin-films for the example of the region shown in Figure 4.21b). The additional phases on top (green color) correspond to the surface phases observed by SEM (Figure 4.19) and TEM (white dashed lines in Figures 4.20a),b) and Figure 4.21b)). EDXS investigation

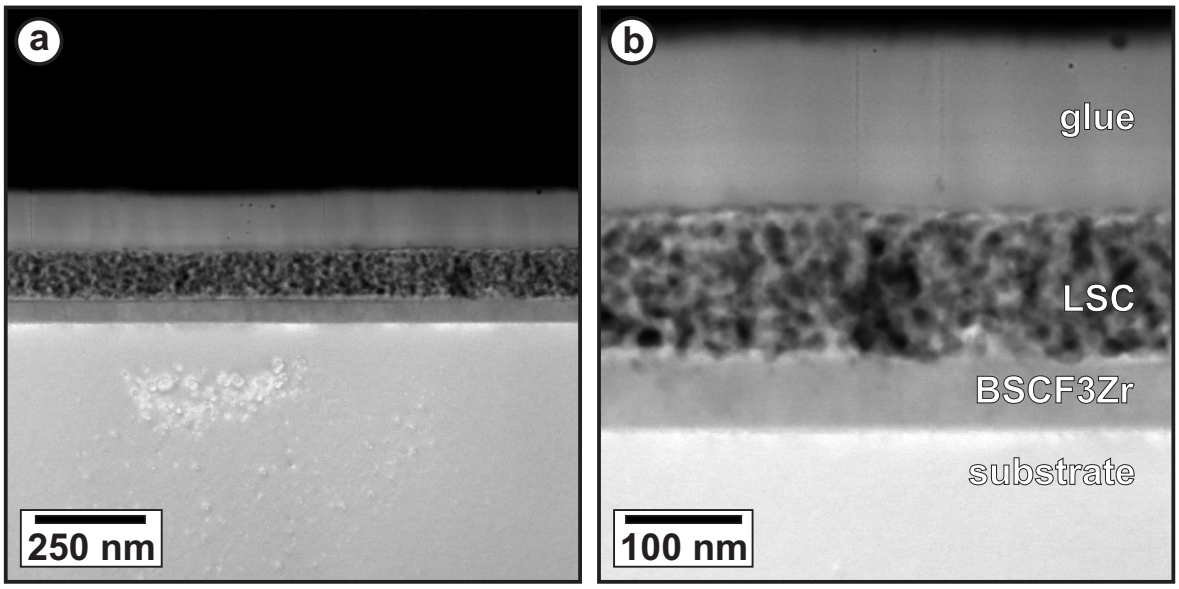

Figure 4.22: a) Overview and b) high-magnification HAADF STEM micrographs of as-prepared LSC on a Zr-doped BSCF thin-film (BSCF3Zr).

of the surface phase yield a high amount of A-site cations in these regions, indicating that carbonates of the A-site earth alkali cations ($BaCO_3$ and $SrCO_3$) could have been formed on the top of the thin-film. This assumption can neither be proved by EDXS as carbon is always present due to contamination, nor by electron diffraction, as these crystallites are very small and unstable under electron irradiation.

4.2.3 Effect of surface coating of epitaxial BSCF layers

As reported in section 4.2.2, epitaxial growth of thin-films on suitable perovskite substrates does not adequately stabilize the cubic perovskite structure of BSCF as plate-like regions and hexagonal phases occur. Furthermore, additional secondary phases on the surface (carbonates) are detected. Plate-like regions and crystallites of the hexagonal phase were observed after annealing at temperatures $\leq 900\,°C$. An yet unidentified phase with spherical precipitates was observed after annealing at temperatures of 700 °C, 800 °C and 900 °C. Furthermore, the formation of $BaCO_3$ and $SrCO_3$ surface phases significantly reduces the active surface for oxygen exchange.
To improve the active surface and to impede the formation of surface phases, samples with an additional, nano-crystalline and nano-porous surface layer were prepared and investigated in detail by TEM in the course of the diploma thesis of Albrecht [116]. LSC64 was chosen as coating material, due to its good stability and oxygen exchange performance [51]. Like for the bulk samples undoped as well as Zr- and Y-doped PLD layers were investigated to further increase stability.

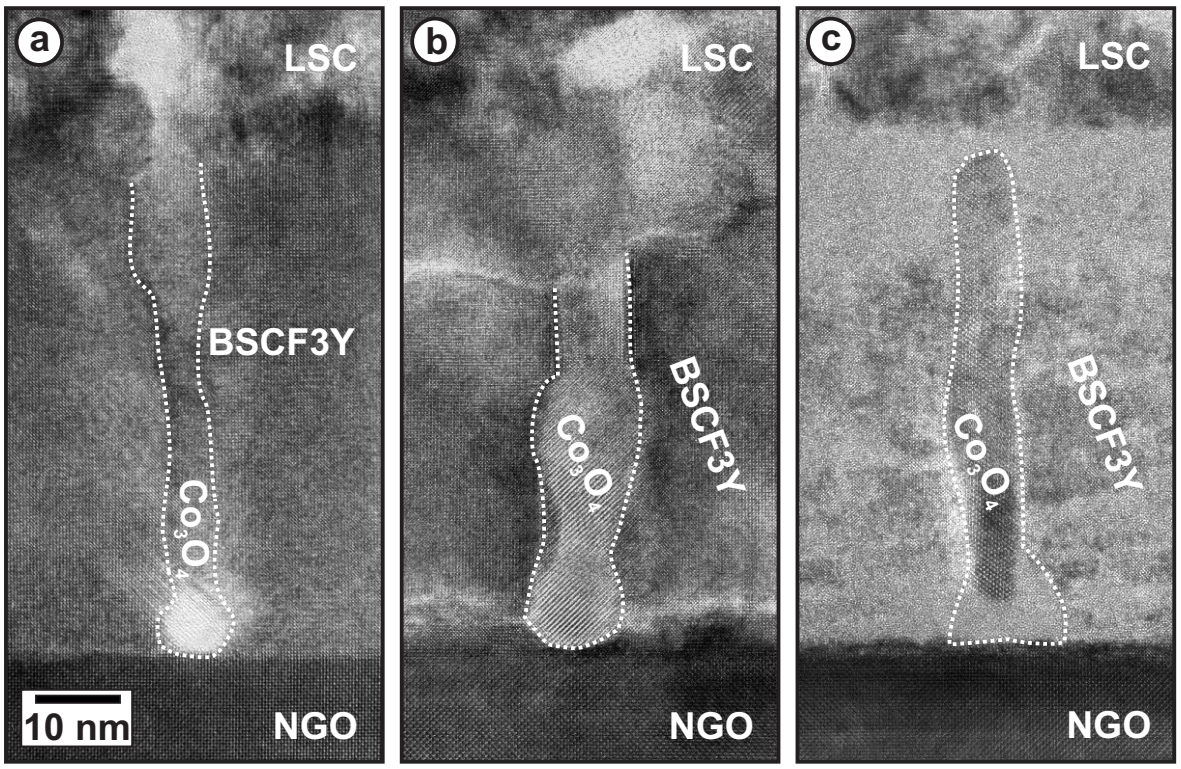

Figure 4.23: Secondary Co_3O_4 phase (marked by white dashed line) in LSC coated BSCF3Y thin-films oriented in a), b) [112]-zone axis and c) [101]-zone axis [116].

Figure 4.22 shows an HAADF STEM image of a cross-section sample of an as-prepared PLD thin-film with LSC coating. The layer system consists of the NGO substrate at the bottom followed by the Zr-doped BSCF thin-film (BSCF3Zr) an the LSC layer on top. In addition, the TEM cross-section images show a layer of glue on top due to the preparation process. The epitaxial PLD layer has a thickness of about 50-65 nm. The thickness of the LSC coating depends on the preparation conditions and the sol concentration. The aim was to produce the coating as thin as possible. Typical values of 50-120 nm were obtained. Figure 4.22b) shows the nanoscaled porosity of the LSC layer, which significantly increases the surface for oxygen exchange.

The samples were also characterized by electric measurements involving heating of the sample. In the course of these measurements the samples were heated in air according to a programmed sequence (see Figure 4.17c)). According to the experiments on uncoated thin-films, one would expect a degradation of the BSCF material after this treatment. The samples were investigated by TEM and EDXS after the annealing by Albrecht [116]. The results of this study are shortly summarized in this section for the example of LSC coated, Y-doped BSCF films which showed the best stability of the cubic phase.

Figure 4.23 shows typical secondary phases in BSCF3Y prior to annealing. The samples were only exposed to the temperature treatment necessary for the LSC coating accord-

ing Figure 4.17b). The analysis of diffractograms calculated from the high-resolution TEM images in combination with EDXS investigations yield Co_3O_4 as only secondary phase in these samples. The regions marked by the white dashed line in Figure 4.23 show the Co_3O_4 phase in [112]-zone axis orientation (Figures 4.23a) and b)), and in [101]-orientation (Figure 4.23c)). The [112]-orientation of Co_3O_4 is preferred for the crystallite growth on BSCF oriented in [001]-direction, because the lattice plane distances of the {220} planes of Co_3O_4 (0.286 nm) fit well to the {110} planes of BSCF (0.282 nm). For the [101]-orientation of Co_3O_4 the {020} and {220} plane distances (0.404 nm and 0.286 nm) are similar to the {001} and {110} plane distances of BSCF (0.398 nm and 0.282 nm). The Co_3O_4 secondary phase is nucleated at the interface between BSCF3Y and substrate and forms a rod-shaped precipitate throughout the whole epitaxial layer.

The chemical composition of the samples was studied by EDXS line profiles on cross-section samples. Figure 4.24 shows the chemical composition of LSC-coated BSCF3Y prior to (Figures 4.24a,b)) and after annealing (Figures 4.24c,d)) along line profiles. The interfaces between NGO/BSCF3Y and BSCF3Y/LSC are indicated by the black dashed lines.

The composition profiles before and after annealing according to Figure 4.17c) do not differ significantly, indicating that interdiffusion between BSCF3Y and LSC is not pronounced. A Sr-enrichment at the interface between BSCF3Y and LSC and between BSCF3Y and NGO can be identified in both linescans. This may be an artifact from carbonate surface phases which formed prior to the LSC coating or may indicate the formation of a perovskite phase with an increased Sr-concentration on the A-site. As after annealing no further enrichment of Ba and Sr at the interface of BSCF3Y and LSC was detected. One can assume a stabilizing effect of the LSC coating. Apart from that, the concentrations in the different layers are relatively homogeneous. Strong changes in the Sr and Co-concentration at the surface of LSC indicate the formation of a Co-rich surface phase after annealing. The influence of possible Co-rich surface phases on the performance was not studied in this work. However, Dieterle et al. reported on small Co_3O_4 precipitates close to the surface of LSC layers which seem to even improve the material performance because of its high oxygen-reduction activity [51, 52]. The LSC coating can be expected to improve the stability of the system and to increase the oxygen surface exchange due to its nanoporous microstructure and its phase composition.

Sintering of the LSC coating during a potential application may be a limiting factor. Dieterle et al. [51] narrowed the temperature range for applications to temperatures below 700 °C. The microstructure of the LSC coating was monitored in the study by Albrecht [116] after annealing according to the temperature characteristics demonstrated in Figure 4.17c) (11.2 h at temperatures above 600 °C). Figure 4.25a) shows a

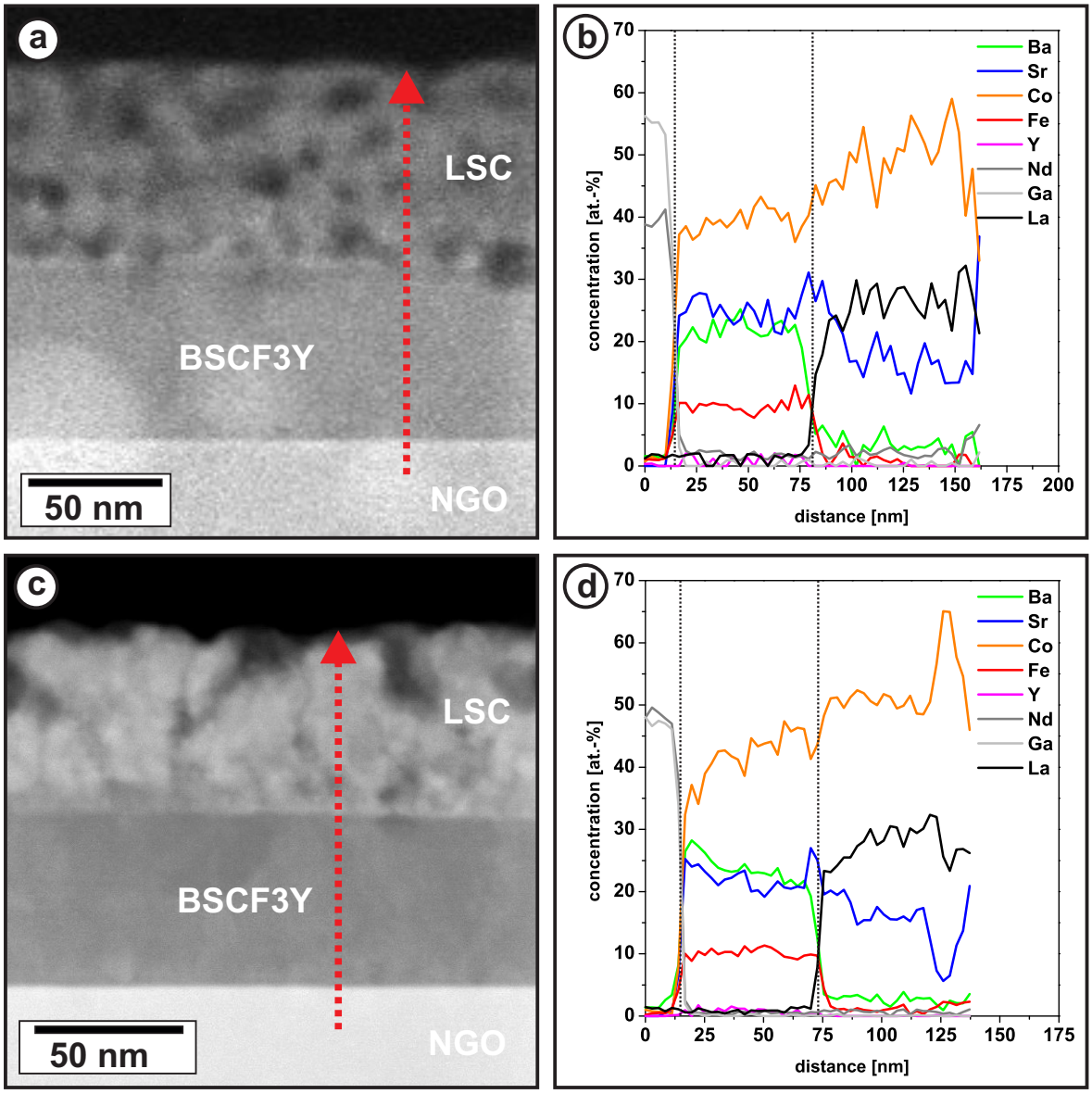

Figure 4.24: Chemical composition of LSC-coated BSCF3Y thin-films a), b) before and c), d) after annealing according to Figure 4.17c) [116]. The position of the linescans is indicated by the red dashed arrows. The interfaces NGO/BSCF3Y and BSCF3Y/LSC are indicated by the black dashed lines.

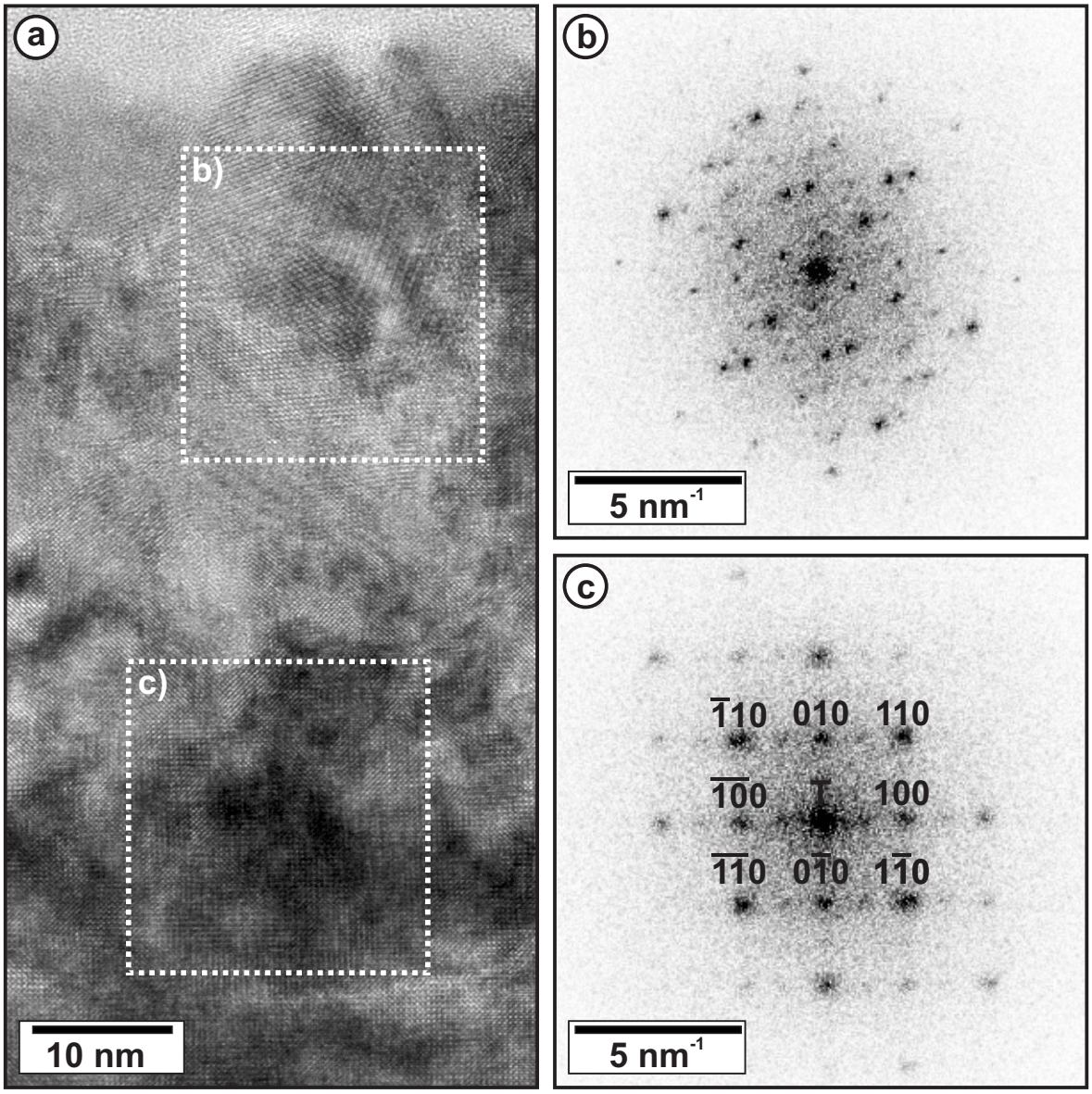

Figure 4.25: Microstructure of the LSC layer after annealing according to Figure 4.17c). a) High-resolution TEM image. White boxes indicate the sample regions of the diffractograms b) and c). The upper part of the LSC coating shows a polycrystalline microstructure. The part closer to BSCF3Y is monocrystalline. [116].

bright-field micrograph of a cross-section of the LSC layer. The white boxes indicate the sample regions which were investigated by FOURIER-analysis. The investigation confirms a polycrystalline structure at the surface of the LSC coating even after annealing (Figure 4.25b)) indicated by the formation of DEBYE-SCHERRER rings arising by diffraction from several differently oriented crystallites. However, the polycrystalline character is lost in regions closer to the BSCF3Y interface due to sintering of the LSC crystallites. Figure 4.25c) shows a difractogram of monocrystalline LSC in [001]-zone axis. The LSC therefore adopts its crystal structure to the BSCF3Y substrate. It is expected that for longer annealing times the monocrystalline region will grow at the expense of the polycrystalline coating.

4.3 Discussion

In the course this work, numerous samples were studied to understand the decomposition of the cubic BSCF and to investigate possible means to stabilize the cubic phase. The discussion is divided into subsections dealing with the formation of each secondary phase separately (subsection 4.3.1 to 4.3.4). The efforts on stabilization of BSCF are discussed in subsection 4.3.5 and 4.3.6. The present work sheds more light on the mechanisms leading to a degradation of the oxygen conductivity. The theories are discussed in subsection 4.3.7.

4.3.1 Stability of the cubic BSCF phase

The temperature dependence of the stability of the cubic BSCF phase in oxygen-containing atmospheres was first investigated by integral methods like XRD and by long-time permeation measurements yielding indirect indication for secondary phases. Shao et al. already reported in their first publication in the year 2000 on a reversible phase formation at temperatures below 825 °C which resulted in a slow decay of permeation performance [12]. Further X-ray analyses were motivated by this publication. As many end members of the BSCF system are either hexagonal or form hexagonal phases at application relevant temperatures, it was expected that the additional phase is hexagonal. After the discovery of a phase transition into a hexagonal phase in BSC [117], the phase was also identified as hexagonal by Švarcová et al. [22] for the first time. Further investigations in this work and by other groups [22, 23, 34] determined the cubic-hexagonal transition temperature to ≤840 °C. As the formation of the hexagonal phase seems to be very slow under the application-relevant conditions slightly below 800 °C, studies of the long-term behavior were started. Mueller et al. [31] reported on a coexistence of both phases with an extrapolated final composition of about 50 % of each phase measured by XRD. According to the data of Mueller et al. 90 % of this phase separation is completed after $t_{90} = 1120$ h. This result was confirmed by Niedrig et al. [34]. Therefore, for microstructural investigations after long-time annealing (see Figure 4.2), a duration well above the t_{90} time (1350 h) was chosen.

XRD is a fast but imprecise method for the determination of volume fractions. Further insight on the decomposition of BSCF were therefore gained in this work by microscopic techniques. As shown in Figure 4.1 the formation of the hexagonal phase at temperatures below 840 °C was verified by SEM. Furthermore it was observed that the hexagonal phase requires a nucleation center for formation. According to the microstructure analyses reported in section 4.1.2, these nucleation centers can be either secondary phases (mainly CoO), triple points, grain boundaries or plate-like regions (see also sec-

tion 4.3.3). At temperatures slightly below 840 °C, the nucleation of hexagonal phase starts at triple points of grain boundaries and secondary phases. It completely decorates grain boundaries at temperatures of 700 °C and below. The nucleation of the hexagonal phase also significantly depends on doping and the grain size (see section 4.3.5) as these parameters influence the amount of the nucleation centers at the grain boundaries.

The formation of plate-like regions is the second effect which has to be studied to understand BSCF degradation. Due to the structure of the plate-like lamellae which mainly consist of a stacking of cubic and hexagonal regions, the plate-like regions cannot be distinguished from larger cubic grains and crystallites of the hexagonal phase by XRD. This led to a late discovery of these structures by electron microscopy contemporaneous by this work and by other groups [24]. Due to the failure of XRD, the temperature and time dependence of the formation of plate-like regions is more difficult to investigate. This work presented the first results reported in early 2012 [118]. Figure 4.2 a) shows the volume fraction of the plate-like regions normalized to a pore-less sample in dependence of annealing time at 800 °C. As no significant change of the fraction was detected, one can deduce that the formation of plate-like regions is very fast and might already be completed after 10 h of annealing. The formation of plate-like regions can therefore explain the accelerated degradation at the beginning of the conductivity measurements reported by several groups [12, 34, 46]. Furthermore the formation of plate-like regions could be so fast that most published conductivity data do not show the possibly negative effects of plate-like regions.

The volume fraction of plate-like regions depending on annealing temperature (700-1000 °C) was also investigated (Figure 4.2 b)). One can see a significant temperature dependence with the largest fraction of plate-like regions at 900 °C. At 1000 °C no additional phases were observed. The size of the plate-like regions also changes with temperature. At 900 °C predominantly large plate-like regions in the order of 1 µm contribute to a relative large volume fraction. At lower temperatures smaller plate-like regions occur in high density.

As shown in Figure 4.3 the volume fraction of hexagonal phase and plate-like regions depends on the distance from the samples surface. While a comparably small volume fraction is discovered close to the surface, inside the bulk material a broad region with an equally distributed high volume fraction of plate-like regions and hexagonal phase was observed. This behavior has to be put in context with the findings of the samples annealed in nitrogen and the results of Liang et al. [111] who reported on a different distribution of hexagonal phase and plate-like regions between permeate and feed side of a membrane. While the authors explain the behavior by oxygen migration paths which correlate with the formation of hexagonal phase, different oxygen partial pressures also play a role in the degradation process. Low oxygen partial pressures stabilize

the cubic phase as demonstrated in section 4.1.2 and reported by Ovenstone et al. [19]. Low oxygen partial pressures correspond to a loss of oxygen in the lattice. This leads to a low valence state of the B-site cations which stabilizes the cubic structure (compare to section 4.3.7). This process also takes place on the permeate side of the membrane and presumably near the surface during annealing, which explains the stabilization on the surface.
Furthermore CO_2 in the annealing atmosphere is reported to change the chemical composition as well as the phase composition up to the depth of several 10 µm [46]. Surface phases of BSCF were studied in detail on epitaxial films (see section 4.2.2). Carbonates were indirectly detected by an enrichment of A-site cations on the surface over the whole investigated temperature range. A yet unidentified phase with spherical morphology was detected in the whole temperature range. The phase could not be assigned to common Co-oxides. Nevertheless, investigations of Albrecht [116] yielded Co-oxides in doped BSCF thin-films and a Sr-enriched perovskite phase which was formed due to an improved adaption of the lattice parameter to the substrate after annealing at 700 °C.
Both hexagonal phase and plate-like regions have a influence on BSCF performance as separation membrane (section 4.3.7). Investigations on temperature and time dependence of BSCF-stability by investigation of the microstructure, therefore resulted in the following temperature ranges for secondary phase formation:

- Plate-like regions form at temperatures at and below 900 °C.
- The hexagonal phase forms at plate-like regions and other nucleation sources like grain boundaries and Co-precipitates at temperatures ≤ 840 °C
- Secondary carbonate phases form at the surface of BSCF in the temperature range 700-900 °C in CO_2-containing atmospheres
- Co-oxides form at the surface in the temperature range under investigation after annealing at 700 °C (no further annealing temperatures were investigated)

Stable operation conditions for undoped BSCF therefore are limited to temperatures above 900 °C. The stability of BSCF in dependence of temperature and doping is summarized in Figure 4.27 in section 4.3.5.

4.3.2 Cobalt oxide precipitates

Co-oxide precipitates were found in all undoped bulk BSCF samples as well as thin-films even for unannealed samples sintered at 1000 °C (see Figure 4.1). In bulk BSCF samples CoO precipitates dominate, while in thin-films mainly Co_3O_4 precipitates were observed. The structure of the Co-oxide is correlated with the temperature during the

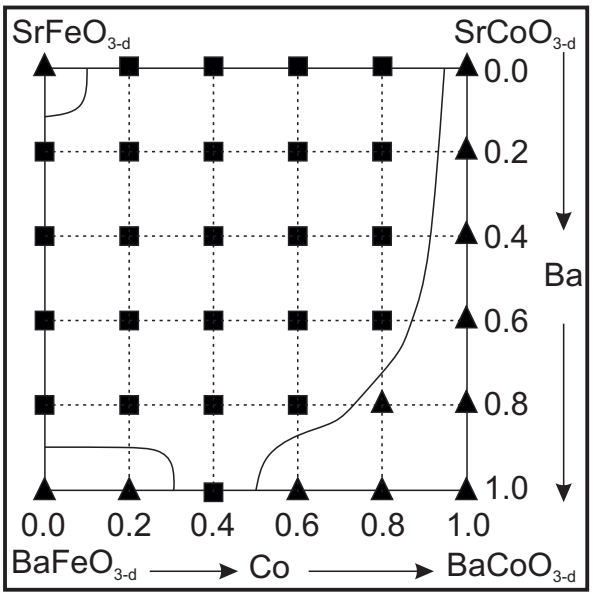

Figure 4.26: Phase diagram of the system Ba-Sr-Co-Fe-O at 1000 °C published by YÁNG et al. [33]. Squares mark the stability region of the cubic perovskite phase, triangles indicate a mixture of cubic and secondary phases.

production process. During sintering of massive samples at 1000 °C CoO precipitates are forming, while Co_3O_4 nucleates at lower temperatures (700 °C) like they occur in the PLD production process.

Few information on the phase diagram of the system Co-O is published. FISHER and TANNHAUSER show phase diagrams of Co-O and state that Co_3O_4 is not stable at temperatures above 920 °C for $p_{O_2} \leq 1$ atm [119]. CHEN et al. [120] report on a mixture of CoO and Co_3O_4 under conditions comparable to BSCF. OKU and SATO [121] studied surfaces by X-ray Photoelectron Spectroscopy (XPS) at low p_{O_2} partial pressures (10^{-3} Pa). They observed a large temperature range (100 °C-600 °C) where both Co-oxides coexist. At temperatures >600 °C CoO is stable.

The formation of CoO in bulk BSCF material and Co_3O_4 in thin-films therefore is consistent with the literature data.

The reason for the nucleation of Co-oxide precipitates can be discussed in context with the phase diagram of the system Ba-Sr-Co-Fe-O published by YÁNG et al. [33] (see Figure 4.26). The authors investigated the composition of the system Ba-Sr-Co-Fe-O by in-situ XRD at 1000 °C. According to their findings, the Co-amount of 80 % on the B-site is at the very edge of the stability region of the cubic phase in the phase diagram. CoO precipitates in the bulk material and Co_3O_4 grains in thin-films form to compensate the Co-excess. CoO precipitates act as nucleation center for the formation of the hexagonal phase.

As discussed in the following subsection 4.3.3 the hexagonal phase itself consists of an increased amount of Co and therefore consumes excessive Co from the cubic phase.

Surface regions of bulk samples were demonstrated to exhibit a lower amount of secondary phase. The stabilization of this region could be caused by a slightly decreased Co-concentration as the Co could be consumed by Co-oxides which were reported as surface phase of thin-films [116]. For application as oxygen conductor, one would choose a stable composition with a maximized Co-amount for best performance.

4.3.3 Formation mechanism of hexagonal phases in BSCF

The hexagonal phase in BSCF can be described by a change of the stacking of the oxygen octahedrons which switch from a corner sharing configuration (cubic) to a face sharing configuration (hexagonal). This mechanism is explained in Figure 4.5. Each twin boundary in the cubic phase introduces a hexagonal layer. Therefore, the hexagonal phase can be considered as a cubic phase with equidistant twin boundaries. Furthermore, the structure of the plate-like regions can be described by this model as they consist of a frequent change between hexagonal and cubic stacking (see Figures 4.4 and 4.5).
Investigations of the BSCF microstructure suggest that the hexagonal phase in the investigated temperature range preferentially nucleates at defects. These nucleation centers were observed to be secondary phases like Co-oxides and grain boundaries. Two mechanisms were observed:

- Plate-like regions start to grow at CoO and Co_3O_4 precipitates and grain boundaries. At temperatures below 840 °C these regions also act as nucleation centers for the hexagonal phase. The hexagonal phase therefore often surrounds plate-like regions, which is observed in Figure 4.4 b).

- The hexagonal phase forms on grain boundaries at temperatures below 840 °C. At temperatures slightly below the formation temperature, the hexagonal phase only forms at grain boundary triple points. For temperatures around 700 °C all grain boundaries are decorated with hexagonal phase.

Rutkowski et al. [122] show SEM images of BSCF samples annealed at 750 °C, 800 °C, 850 °C and 950 °C showing exactly the same temperature dependence of the BSCF microstructure as reported in this work. However no further interpretation of the images is presented. Liang et al. [111] investigated BSCF membrane material after oxygen conductivity tests and detected a significant variation of the microstructure between permeate and feed site of the membrane. At the permeate site, consistent with our results, phase transitions mainly took place at the grain boundaries. At the feed side, secondary phases were found inside crystallites. This was explained by the migration paths of the oxygen which is incorporated into the material at the whole surface, while the O^{2-}-current is collected at the grain boundaries. According to the authors,

O-diffusion destabilizes the perovskite due to the influence of the local O-deficiency and B-site valence state.

The determination of the Co-valence state of annealed BSCF samples further improves the understanding of the complex decomposition of BSCF into the hexagonal phase. It was suggested by several groups [24, 26, 28, 32] that a change of the Co-valence state towards higher values, coupled with a change of the spin state leads to the formation of the hexagonal perovskite phase. The change of the Co-valence is induced by the change of the oxygen deficiency as a function of temperature. Kriegel et al. [93] measured a large oxygen deficiency at high temperatures (1000 °C; d=0.7) and a smaller value at room temperatures (d=0.5). Charge balance is achieved by a valence change of the multi-valent B-site cations (mainly Co). The formation of the hexagonal phase is therefore facilitated if the temperature-dependent Co-valence state in the system falls below a distinct threshold. This temperature was experimentally determined to be 840 °C by Niedrig et al. [34].

As shown in section 4.1.5, the hexagonal phase is enriched in Co, while Fe is not on the B-site. The chemical composition of the hexagonal phase can be explained by the different stacking of the oxygen octahedrons. The distance between B-sites in the hexagonal phase is only about 94 % of the cubic spacing. According to Efimov et al. [24], Co therefore can further increase its valence state corresponding to smaller cations (see table 2.1 [16]). Fe apparently does not change its oxidation state of 3+ as easyly as Co [2] and is too large to be accomodated in the hexagonal structure. Harvey et al. [26] found no transition of Fe 3+ in the application-relevant temperature range to other Fe oxidation states. These findings can be explained by measurements of Teraoka et al. [27] who investigated the cation valence states in $LaCoO_3$ and $LaFeO_3$. While the transition from Co 3+ to Co 2+ was observed at temperatures above ≥ 900 °C, the transition from Fe 3+ to Fe 2+ was observed at temperatures ≥ 1450 °C.

The increased valence state of Co of 2.8+ (± 0.2) in the hexagonal phase compared to 2.2+ (± 0.2) for the cubic phase after annealing at 650 °C was observed experimentally by EELS and reported in section 4.1.8. EDXS profiles as shown in Figure 4.9 also indicate an Fe-cation excess in the vicinity of the hexagonal phase. Moreover, Co-cations from the vicinity of the hexagonal phase diffuse in and occupy the vacancies left by the Fe-cations causing Co-depletion in the vicinity of the hexagonal phase.

Co can therefore be contained in the cubic and hexagonal phases and facilitates the transition from the cubic to the hexagonal BSCF phase. Because of the required cation demixing, the hexagonal phase forms at a slow rate in BSCF.

4.3.4 Microstructure and formation mechanism of plate-like regions

Complex metal oxides with stacked structures were already described in the 1960ies by Katz and Ward [123]. Yvon and Parthé worked on the notation and categorization of complex oxide and carbide structures [124, 125]. TEM on Ba-containing polytypes was performed by Hutchison and Jacobson [126] as well as Landuyt et al. [127]. Boulahya et al. [128–131] and others [132] report on several ordered barium cobaltates with complex hexagonal stacking. However the described oxides cannot explain the deviation from the ABO_3 composition detected in some plate-like regions. Sun et al. [29] and others [30] finally report on ordered barium cobaltites with a chemical composition which is consistent with the EDXS results. Efimov et al. [24] independently reported on structures similar to those reported by Sun et al. in annealed BSCF samples. They also found regions with different chemical compositions and a deviation from the ABO_3 composition. However, due to insufficient crystallographic data, they could not directly verify the identical crystal structure of the phase found in BSCF and the barium cobaltate described by Sun et al. [29].

As described in section 4.1.3 and 4.1.4 two types of plate-like regions occur in BSCF. The first type of plate-like regions consists of thin lamellae of cubic and hexagonal stacking. The different lamellae can be described by a change of the orientation of oxygen octahedrons from corner-sharing to face-sharing. This phase transformation is impeded by the absence of Fe in the hexagonal structure which was demonstrated to diffuse out of the hexagonal regions into the surrounding cubic phase (Figure 4.9 b)).

The second type of plate-like regions contains an additional secondary phase denoted as BCO-type phase. It was described by an ordered cubic stacking of oxygen octahedrons, as well as an edge-sharing configuration of the octahedrons as it is observed in the CdI_2 structure. The formation of this secondary phase involves even more pronounced cation diffusion, as the ABO_3 composition is violated.

Both types of plate-like regions were found to occur separately but also in mixed settings of regions with lamellae of cubic, hexagonal and BCO-type phase. In principle any layer sequence of cubic, hexagonal and BCO-type phase could be formed because only a change from corner- to face- or edge-sharing orientation of oxygen octahedra is required. In addition, the amount of cubic layers n inside the BCO-type phase was also demonstrated to vary rendering the sequence of lamellae in plate-like regions even more complex.

The chemical composition of the BCO-type phase detected in this work deviates from the composition described by Sun et al. [29] as additional Fe cations share the B-site. According to David et al. [30] who report on different oxidation states of Co in the phase, Fe-cations can occupy the B-sites. While the mean valence was determined to

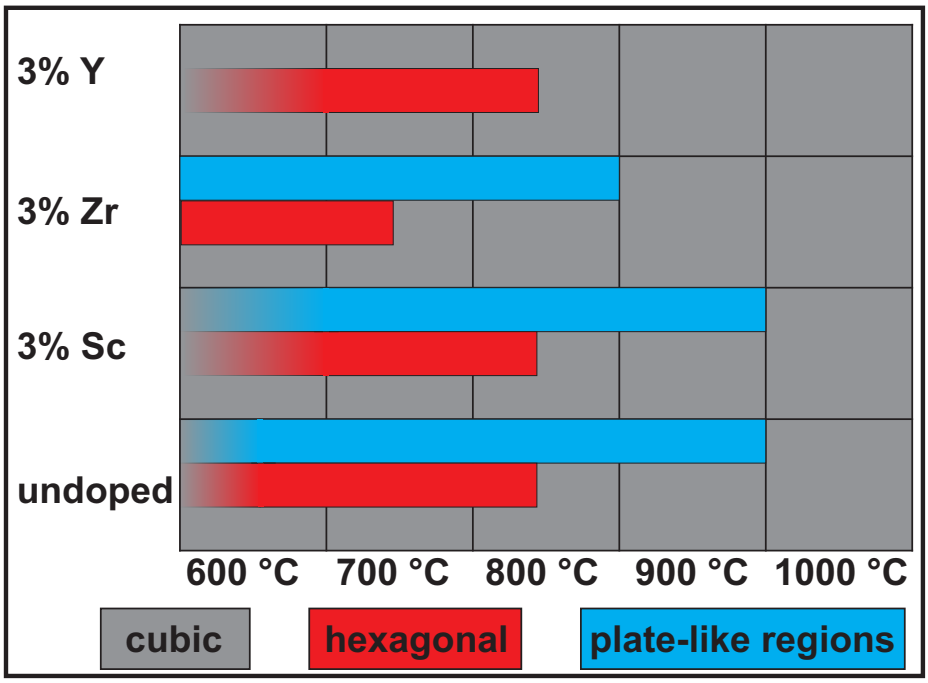

Figure 4.27: Overview of phase composition depending on annealing temperature (600 °C-1000 °C) and doping with Zr, Sc and Y.

be +2.7, depending on the exact atomic site the Co-valence state switches between Co^{2+}(HS), Co^{3+} (LS) and Co^{3+}(HS). According to Table 2.1 the Co-radius varies depending on the oxidation state between 54.5 pm and 74.5 pm. This means that cations of all possible Fe valences fit into gaps between octahedra and can therefore be interchanged with Co.

Plate-like regions were detected after annealing at temperatures of 900 °C and below. Since the hexagonal phase was reported [34] to form at temperatures below 840 °C, one can conclude that plate-like regions observed after annealing at temperatures above 840 °C mainly consist of the BCO-type phase. EDXS linescans and mappings recorded in the course of the present study support this assumption. Plate-like regions after annealing at 850 °C are characterized by the absence of Sr and the increased amount of Co, which are typical for the BCO-type phase. After annealing at temperatures below 840 °C plate-like regions additionally contain hexagonal lamellae. As the hexagonal phase was found to form at defects like grain boundaries and precipitates, the BCO-type phase acts as additional nucleation center for the hexagonal phase.

4.3.5 Effect of doping on performance and stability

Figure 4.27 summarizes the effect of doping of the BSCF material in terms of phase composition after annealing for 100 h. Both Y- and Zr-doping resulted in a significant improvement of the microstructure. While Y-doping successfully prevents the forma-

tion of plate-like regions, doping with Zr was found to increase the stability region of cubic BSCF towards lower temperatures. Sc-doping, in contrast, did not improve the microstructure although the verification of traces of the dopants in the sample was qualitatively achieved by EDXS and EELS.
To correlate any improvement of the microstructure with a particular dopant, one has to rule out effects observed by Ge et al. [133, 134] who investigated stabilizing effects of a 3 % A-site or B-site deficiency. While A-site deficiency showed negligible effects on stability, for B-site deficiency no significant degradation of the electrical and ionic conductivity after annealing at 850 °C for 350 h was observed. Furthermore, no significant performance drop compared to conventional BSCF was reported.
B-site deficiency can be eventually caused by Y-doping. While Sc and Zr are expected to occupy the B-site because of their small ion radius, Y has a larger ion radius and was reported to also occupy the A-site of the perovskite structure [135]. In this case a B-site deficiency would be directly introduced by doping as Y was introduced into the starting powder at the expense of B-site cations.
The effect of B-site doping therefore may be accredited to the deficiency of the B-site cations Co and Fe. However, this effect can be ruled out by the behavior of the Sc-doped samples, where stabilizing effects were not observed despite of successful doping. Suitable dopant cations therefore have a direct influence on the material stability.
Several potential effects of doping may contribute to the observed improvement of the microstructure the performance:

- The formation of the hexagonal phase and plate-like regions was found to be facilitated at defects like precipitates and grain boundaries (see also Meffert et al. [87]). Doping with suitable cations could improve the sintering process leading to larger grain sizes and therefore an overall smaller number of nucleation centers for secondary phases. Ge et al. [133, 134] discuss improved sintering for both A- and B-site deficient BSCF. Ran et al. [136] investigated the effect of several foreign oxides on sintering. CoO and Co_2O_3 were demonstrated to significantly increase the grain size. Co_2O_3 also led to a significant improvement in electrical and ionic conductivity, which can be correlated with the larger grain size. Detailed investigations dealing with the influence of doping on the microstructure are currently conducted.

- It was observed that dopants do not occur in the hexagonal phase and plate-like regions. Secondary phase formation is therefore always accompanied by diffusion of the dopants. This effect could decrease the speed of possible phase transitions. The cations for doping were chosen to be single-valent. It was shown by EELS investigations conducted in the course of the present study that the formation of secondary phases involves a change of the valence of the B-site cations (especially

Co). The dopants therefore could behave like Fe-cations which also do not tend to change their oxidation state in BSCF and therefore have to diffuse out of the hexagonal phase.

- The microstructural findings suggest that Y-doping significantly suppresses the formation of plate-like regions containing the BCO-type phase. This effect may be based on the significantly larger ion radius of Y compared to the other B-site cations distorting the perovskite structure in a way that the CdI_2-type stacking is not possible. The suppression of the BCO lamellae further reduces the number of nucleation centers for the hexagonal phase leading to an overall absence of plate-like regions.

- Although direct stabilizing effects introduced by B-site deficiency were ruled out, B-site doping indirectly lowers the Co-concentation in the perovskite. As discussed earlier (e.g. see Figure 4.26), this could prevent the formation of Co-oxide precipitates acting as nucleation center for secondary phases. For Y-doping Co-precipitates could not be detected.

The influence of the improved microstructure on the performance of doped BSCF was not investigated by this study. However it delivers an explanation for the results of Yakovlev et al. [43] and Haworth et al. [44, 45] who reported on improved long-term stability of the O-permeation for Zr and Y-doped BSCF.

4.3.6 Effect of surface coating on performance and stability

BSCF thin-films were prepared and annealed to investigate phase transitions at the surface and the influence of thin-films on phase stability (section 4.2.2). Epitaxial growth on suitable perovskite substrates with small lattice parameter mismatch was not found to improve phase stability significantly. Furthermore, surface effects led to additional phases after annealing. Beside a significant increase of surface phase formation with annealing temperature (Figure 4.19) no significant dependence of the microstructure on the annealing temperature was observed. This indicates that for small sample dimensions additional effects compared to bulk material occur. One has also to state that the investigated sample volume in TEM cross-section samples is much smaller for thin-films and therefore leads to worse statistics with respect to phase distribution. Plate-like regions form perpendicular to the substrate or under angles of 45° and 60°. As in bulk samples, the hexagonal phase is observed in the vicinity of the plate-like regions. Overall, the formation of the hexagonal phase is suppressed due to the lack of nucleation centers at grain boundaries.

The hexagonal phase in thin-films which nucleates at plate-like regions was found to be additionally depleted of A-site cations. Since the chemical analyses indicate an increasing amount of alkaline earth cations at the surface, one would suggest that these elements diffuse from the thin-film to the surface. As the samples were annealed in ambient air, the formation of carbonates ($BaCO_3$ and $SrCO_3$ or $Ba_xSr_{1-x}CO_3$) is highly probable. The formation of carbonates was also reported by several other groups investigating the surface of BSCF bulk material [46–48]. The degradation induced by CO_2 are reported to be dominantly of mixed carbonates $Ba_xSr_{1-x}CO_3$. The transformation was found to be reversible in helium atmospheres [46]. Large CO_2 concentrations can completely stop oxygen permeation due to a dense reaction layer of several µm in thickness. Modest CO_2 concentrations in ambient air only reduce the performance. This is in good agreement to the surface structure observed by SEM on our samples, which only covers a part of the BSCF surface.

Ge et al. [134] report on the formation of hydroxides ($Ba(OH)_2$ and $Sr(OH)_2$) in B-site deficient BSCF in contact with water. EDXS could only demonstrate the enrichment of alkaline earth elements on the surface, as carbon is always present in X-ray spectra due to contamination and hydrogen cannot be detected by EDXS. Furthermore, the sample preparation process for TEM cross-sections involves gluing of sandwiches which introduces additional carbon at the surface region of the sample.

Additional spherical-shaped phases were present. Co-enrichment hints at the formation of a secondary Co-rich perovskite phase, as no common Co-oxide could be assigned to the structure by electron diffraction.

To overcome the surface instability, LSC coated thin-films were investigated. The results are reported in section 4.2.3. Nanocrystalline LSC was successfully prepared by Hayd [50] and Albrecht [116]. It was demonstrated by Hayd and Dieterle [50, 51] that such a functional layer improves the oxygen surface exchange significantly and therefore is suitable for oxygen separation membranes. It was also discussed by Dieterle et al. [51] that coarsening of the LSC coating limits the application of LSC with a nanostructured coating to temperatures below 700 °C. Similar effects were observed in the present study where a sintering of the functional layer with significant growth of the crystallites was discovered even after annealing for only 11.2 h at temperatures in the range 600 °C-700 °C. The application of nanostructured functional layers therefore might be restricted to temperatures well below 700 °C.

The aim of the current study was the investigation of a possible stabilizing effect of such a coating because it could potentially protect BSCF from atmospheres which induce the formation of surface phases (CO_2; water vapor). For the investigation of stabilizing effects, thin-films from Zr- and Y-doped BSCF were prepared because these compositions showed best phase stability for bulk material. EDXS linescans probing the chemical composition of the whole layer system after annealing do not indicate the

formation of A-site cation enriched surface phases. The LSC layer therefore prevents surface degradation of BSCF. Furthermore, no significant interdiffusion between NGO substrate and epitaxial thin-film was detected. However, the formation of secondary phases inside the epitaxial BSCF layers could not be prevented. A large volume fraction of Co_3O_4 precipitates form in Zr-doped BSCF. Y-doping was found to suppress the formation of Co-oxides but could not completely prevent it. Like for the precipitation in bulk material the instability can be explained by the intrinsic excess of Co for $Ba_{0.5}Sr_{0.5}Co_{0.8}Fe_{0.2}O_{3-\delta}$. As the temperatures during the production process of thin-films are lower compared to bulk material, Co_3O_4 forms preferentially. Due to the properties of the Y-cation which can also occupy the A-site [135], the Co-excess could be reduced in Y-doped samples. Indiffusion of Co from the LSC into BSCF could additionaly contribute to the intrinsic instability of functionalized thin-films. As discussed by Dieterle et al. [51] Co_3O_4 precipitates close to the surface of an oxygen conductor are not necessarily undesirable because they are catalytically active and enhance the oxygen surface exchange. However, inside bulk material Co-oxide precipitates mainly act as nucleation center for unwanted secondary phases. Kerman et al. [137] managed to produce a functionalization layer of nanocrystalline BSCF. For application in CO_2-free atmospheres this approach might be very promising to overcome Co-diffusion from the LSC into the BSCF.

4.3.7 Degradation of oxygen permeation

The effect of annealing and doping on the phase composition and microstructure of BSCF was investigated and discussed in the course of this work. For a potential application of BSCF as oxygen separation membrane the link between microstructure and performance has to be discussed in detail. As this work was mainly based on the electron microscopical studies, oxygen permeation experiments could not be conducted. The aim of this section is therefore to put our results in context with macroscopic findings reported by other groups.

Since the formation of secondary phases is mainly confined to the grain boundaries, their effect on the oxygen conductivity has to be discussed in detail. Martynczuk et al. [138] report on an improved oxygen conductivity for larger grain sizes in the system $Ba_{0.5}Sr_{0.5}Fe_{0.8}Zn_{0.2}O_{3-\delta}$. Grain boundaries can therefore be considered as barriers for oxygen diffusion. Arnold et al. [139] confirms these findings for BSCF and even describes an oxygen flux proportional to the grain size. Burriel et al. [112] demonstrated a significantly higher conductivity for monocrystalline BSCF PLD thin-films. Contradictory to these results Baumann et al. [140] cannot confirm a dependence of the oxygen conductivity on grain size. Therefore both bulk diffusion and grain boundary diffusion account for the oxygen conductivity. However, as no dependence

on porosity (influencing bulk diffusion) was found, the authors suggest grain boundary diffusion as most important mechanism. Liang et al. [111] suggest an incorporation of the oxygen into the membrane at the whole surface and, therefore, bulk and grain boundary diffusion as being equally important at the feed side of the membrane. The oxygen flux is then collected at the grain boundaries leading to a grain boundary diffusion at deeper regions of the membrane.

According to the results of this work the plate-like regions also have to be taken into account for the discussion of the conductivity mechanism. Mogensen et al. [141] states that any deviation from the cubic perovskite structure leads to a degradation of the oxygen conductivity. The plate-like regions with numerous cubic-hexagonal interfaces form a barrier for oxygen conductivity along cubic [111]-direction, while cubic layers may still conduct oxygen ions parallel to the {111}-planes. Furthermore, CdI_2 layers can be considered as a barrier for at least electron conductivity due to the anisotropy of the resistance found by David et al. [30]. Larger plate-like regions containing BCO-type phase are mainly detected at temperatures of 900 °C.

As schematically shown in Figure 4.1 plates often form perpendicular to grain boundaries ([111]-direction vertical to grain boundary) at temperatures below 900 °C and for this reason act as oxygen diffusion barrier. This may explain the outstanding performance of Y-doped BSCF, as Y-doping prevents the formation of plate-like regions (see scheme Figure 4.10).

Hexagonal regions are reported to be suppressing oxygen conductivity [24, 111, 142]. Despite the outstanding performance of Y-doped material, the formation of the hexagonal phase in Y-doped BSCF at the grain boundaries is comparable to all the other samples investigated in the course of this work. Therefore, one can conclude that in contrast to the published results [24, 111, 142] after annealing for 100 h the hexagonal phase at the grain boundaries does not influence oxygen conductivity significantly. If one assumes that the grain boundaries generally act as diffusion barriers, the hexagonal phase at the grain boundaries might not have a significant effect compared to secondary phases extending into cubic grains.

The degradation of BSCF could then be explained by a two-step process. The fast formation of the plate-like regions mainly consisting of BCO-type lamellae leads to a strong degradation of the oxygen conductivity which is accompanied by a slower formation of hexagonal phase nucleating at grain boundaries and around plate-like regions. The nucleation of the hexagonal phase is responsible for the degradation at long-term scales. As it significantly increases its volume fraction, it may grow into the cubic grains. This effect leads to the degradation which was accounted to the hexagonal phase in literature [24, 111, 142].

For BCO data on oxygen conductivity is not published. The electrical properties of BCO are described by David et al. [30] as semiconducting with a significantly higher

resistance in stacking direction compared to the in-plane resistance. This indicates that the orientation of plate-like regions to the oxygen migration paths may influence the membrane performance.

The measurement of the electrical conductivity of bulk material (Figure 4.13) also contributes to the comprehension of the BSCF degradation. All samples expect for the Y-doped material show degradation of the electric conductivity at temperatures above the formation threshold of the hexagonal phase at 840 °C. This degradation has to be attributed to the BCO-type lamellae in plate-like regions. Especially at higher temperatures (900 °C) the plate-like regions are found at the grain boundaries reaching inside cubic grains. In contrast to the ion current, the electric current seems to be distributed over the whole sample. Grain boundaries may be charged and have therefore a resistive character. The significant improvement of the electric conductivity for Y-doping (see Figure 4.1.7) may be explained by the interaction of hexagonal phase and plate-like regions. The hexagonal phase may be a good electron conductor. As this phase accumulates at the grain boundaries, an electric short-cut is forming. The plate-like regions block this short cut for all samples except for Y-doping, where plate-like regions were not found. One can postulate an inverse temperature dependence of the electrical conductivity, which explains the significant higher conductivity at 700 °C compared to 800 °C. This model, however, does not explain the slight improvement of the conductivity at temperatures above 840 °C which would rather indicate a semiconducting behavior of the hexagonal phase at higher temperatures.

5 Growth and interfacial properties of $CaCuO_2$ films on $NdGaO_3$ substrates

The perovskite system is a very versatile material class. Depending on the specific cations on the A- and B-site, not only oxygen conductivity, but also properties like magnetism and superconductivity can be tailored. Furthermore, the ability to grow epitaxial thin-films on perovskite substrates by PLD allows to adapt materials with slightly different lattice parameters on the perovskite substrate. In the following chapter, the structural properties of $CaCuO_2$ (CCO) thin-films on $NdGaO_3$ (NGO) substrates were studied. It was investigated if CCO can be stabilized on the substrate. Furthermore, aim of the experiments was the correlation of the interfacial properties of the heterostructure with superconductivity.

5.1 Results

NGO substrates were treated by the method described by Ohnishimi et al. [59] to produce purely A-site terminated substrates, which involves an annealing treatment at 1000 °C for 2 h in air. Figure 5.1 shows an HAADF STEM image of an uncoated NGO substrate oriented in [001]-zone axis which was found to be mainly A-site terminated. Bright atom column contrast corresponds to the heavier Nd-atoms, less intense columns are occupied by Ga-atoms. However, in contrast to the published results of Ohnishimi et al. B-site termination was also found. The dashed boxes in Figure 5.1 mark two regions with different termination. The ratio between A- and B-site was estimated to be about 2:1.

The substrates were coated by PLD using a KrF-excimer Laser ($\lambda = 248\,\text{nm}$). The repetition frequency of the laser was 2 Hz at an energy of $E = 120\,\text{mJ}$ corresponding to a laser fluence of about 3-4 J/cm^2. Layers with a thickness between 10-40 nm were produced at a deposition rate of 0.19 Å per pulse. Figure 5.2a) shows a HRTEM image of CCO on a [001]-oriented NGO substrate. The corresponding Fourier transform of the image is presented in Figure 5.2b). Fourier transforms of image regions indicated in Figure 5.2a) are presented in Figures 5.2c)-e). In Figure 5.2a) can be clearly seen that the first 4 nm of the CCO layer show a different contrast, hinting at a disturbed epitaxial growth at the interface. However, the reflections in the Fourier transform in direction of the interface ([100]-CCO and [$\bar{1}$10]-NGO) are at the same positions, indi-

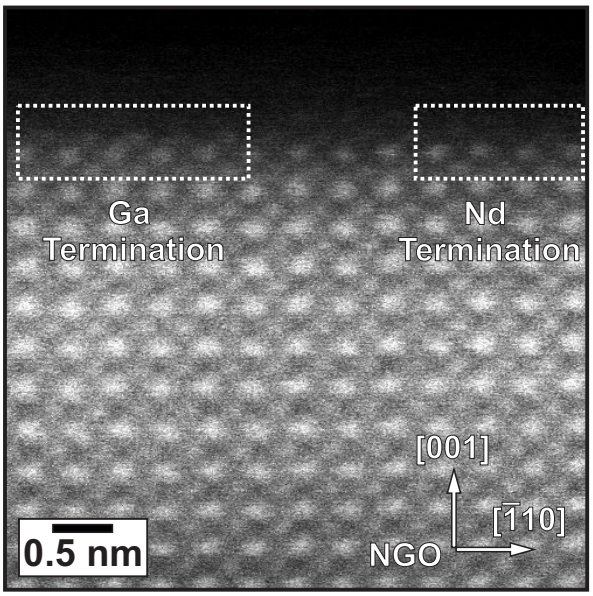

Figure 5.1: HAADF STEM image of the NGO surface prior to CCO deposition showing both A-site and B-site termination.

cating a good lattice parameter matching. In growth direction, the lattice parameter of CCO is significantly smaller than the lattice parameter of the substrate, resulting in different distances of the reflections in the FOURIER transform. The FOURIER transform of the interface region (Figure 5.2c)) shows a broadening of the reflections perpendicular to the interface which are introduced by the distortions of the first atomic planes of the epitaxial PLD layer. These distortions are responsible for the different contrast at the interface in the HRTEM image Figure 5.2a). Reflections from the region above the interface (Figure 5.2d)) appear as sharp reflections and indicate a high degree of crystallinity, in the epitaxial layer above the distorted interface region. Some regions show twin boundaries perpendicular to the interface. The FOURIER transform of the region (Figure 5.2e)) shows streaks perpendicular to the corresponding distortions.
Figure 5.3 shows several twin boundary distortions in detail (marked by arrows). The formation of twin boundaries was shown to be a relaxation mechanism in thin mismatched $LaCoO_3$ layers on LSAT substrates [143] and for epitaxial BSCF films on LSAT as well as NGO (see chapter 4.2.2), which is correlated with the mosaic spread of 0.1° measured by X-ray diffractometry by FUCHS et al. [143].
For thin coatings of 10 nm, Cu-oxide precipitates were found on top of the CCO layer. As shown in Figure 5.4, these secondary phases are spherical and have a diameter in the order of 10 nm. EDXS investigation yielded the presence of Cu and O. Based on the FOURIER analysis of HRTEM images like Figure 5.4, an evaluation of the lattice parameters and a comparison with literature data of CuO [144], Cu_2O [145], Cu_4O_3 [146], and Ca_2CuO_3 [147] was performed. The evaluations demonstrated the existence of dominantly both, Cu_2O and CuO.

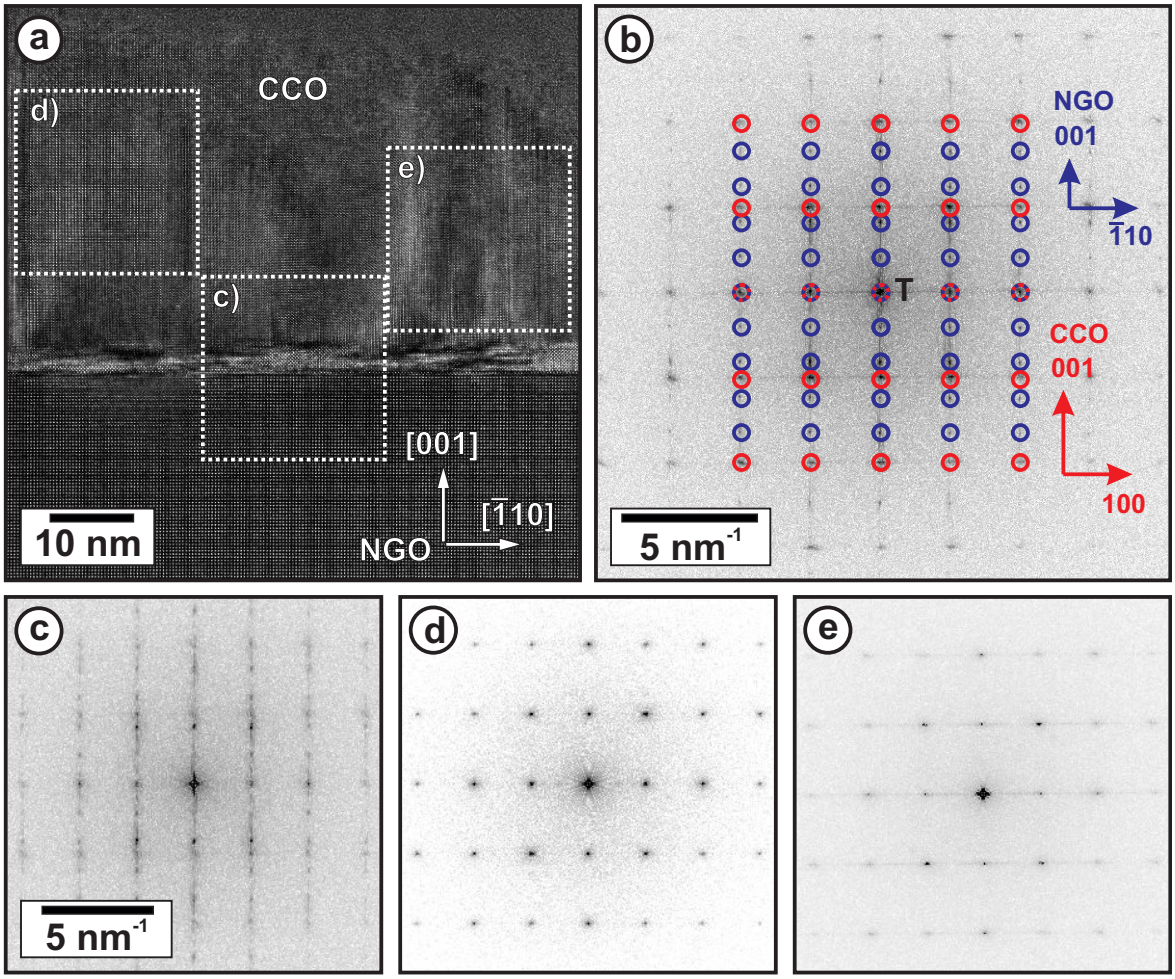

Figure 5.2: a) HRTEM image of CCO grown on a NGO substrate in [001]-zone axis orientation. b) FOURIER transform of a) with reflections of NGO substrate (blue) and CCO layer (red). c)-e) FOURIER transforms of sample regions indicated in a) showing c) the disturbed interface, d) the CCO layer free of distortions, and e) the CCO layer rich of distortions.

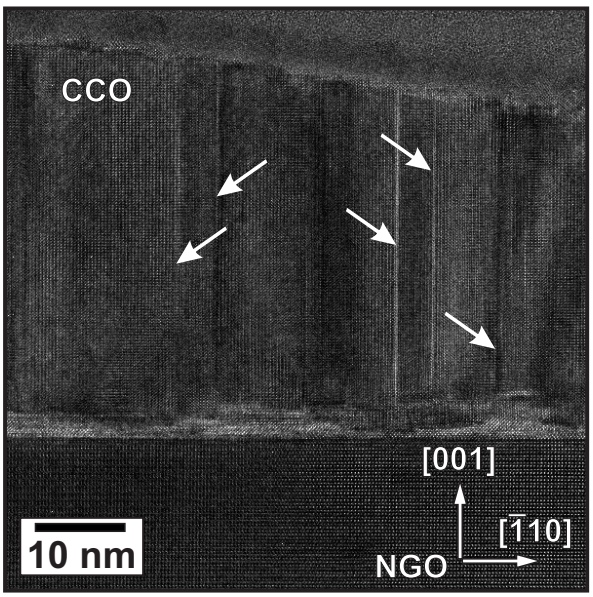

Figure 5.3: HRTEM image of CCO layer on NGO showing perpendicular twin boundaries in the epitaxial layer marked by arrows.

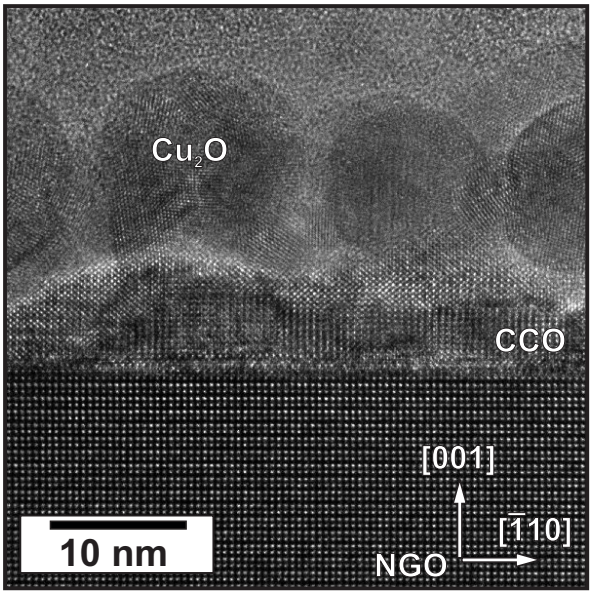

Figure 5.4: HRTEM image of a thin CCO PLD layer with both Cu_2O and CuO precipitates on top.

atom column	atomic number Z $[u]$
Nd	60
GaO	47
CuO	45
Ca	20

Table 5.1: Atomic number Z of atomic columns in CCO-NGO.

Despite the distorted interface region shown in Figure 5.2 and 5.4, smaller, undistorted regions were found and analyzed by quantitative HAADF STEM to determine the stacking of the atomic planes at the interface. Figure 5.5a) shows a HAADF STEM image of such an undistorted interface region. For a quantitative evaluation of the image contrasts, intensity linescans in direction indicated by the arrow along the $[\bar{1}1\bar{1}]$-direction were performed. In this direction, the sequence of the atomic columns in the image plane is A-BO-A-BO. Therefore, all cations of the interface system occur in the intensity linescan, independent of any possible termination. Multiple slices of the dashed box of Figure 5.5a) were aligned by cross-correlation and summed up to improve the SNR. The result of the evaluation is presented in the inset of Figure 5.5b). The intensity scans of the noise-reduced calculated image are shown in Figure 5.5b). The black curve represents an intensity scan of the inset before background subtraction. The background was subtracted by fitting a high-order polynomial to manually defined nodes using the freeware Fityk [148], resulting in the blue curve. As described in section 3.4, the image intensity in HAADF STEM images depends on the atomic number Z for sample regions with the same thickness. Calculated values for the integral atomic numbers in the CCO-NGO system are listed in Table 5.1. The difference between the contrast of GaO and CuO amounts to only $\Delta Z=2$ and therefore cannot be resolved by the presented method. Both potential stacking sequences Ca-CuO-Nd-GaO (A-termination) and CuO-Ca-GaO-Nd (B-termination) can therefore explain the calculated intensity profile shown in Figure 5.5b). The desired A-site termination can not be verified by a Z-contrast-based evaluation.

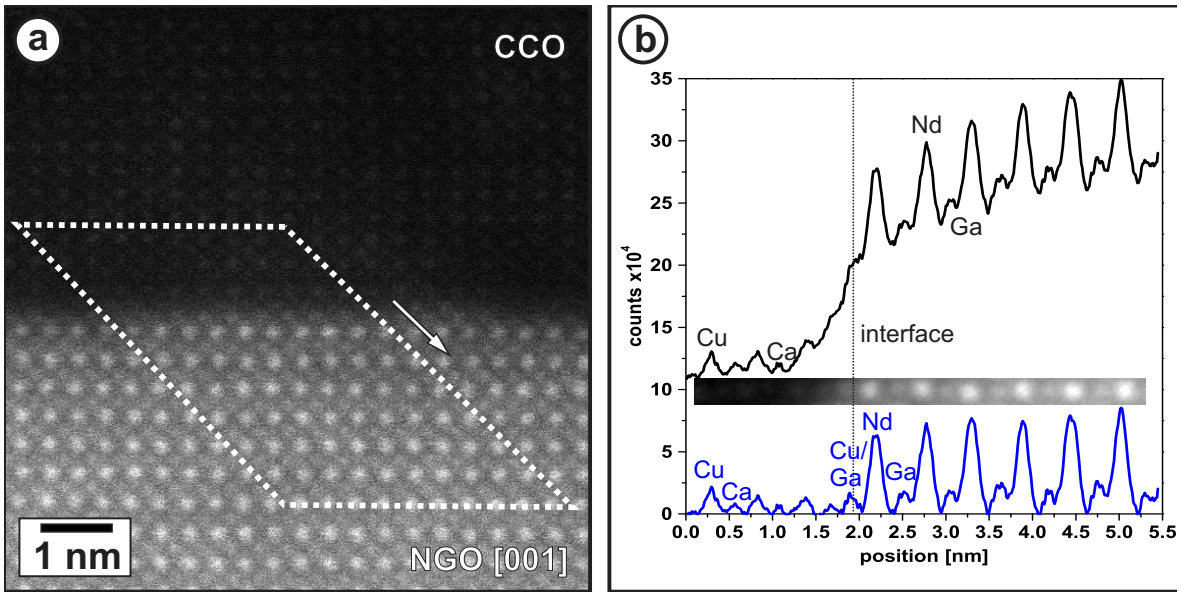

Figure 5.5: a) HAADF STEM image of an undistorted CCO-NGO interface section. The region of quantitative investigation is indicated by a dashed box. The white arrow shows the direction of the intensity linescans shown in b). The inset HAADF STEM image in b) is the sum of multiple aligned slices from the dashed region in a) along the indicated direction. The black curve represents an intensity scan of the inset before background subtraction, the blue curve after background subtraction.

5.2 Discussion

The observation of both, A- and B-site termination of thermally treated NGO substrate is in strong contrast to the nearly perfect A-site termination of substrates prepared by Ohnishi et al. [59]. The same annealing treatment resulted in an interface with A- and B-site termination. Ohnishi et al. conducted AFM measurements resulting in a step hight of one unit cell. For a mixed termination one would expect additional steps of the height of one half unit cell. However AFM measurements on the annealed substrates are hard to perform because the material is isolating. The measurement is therefore influenced by electrostatic charging effects.

Wrong interpretation of the position of the sample surface stemming from sample preparation mainly due to amorphization of the crystal structure can be excluded. The image intensity of the amorphous layer on top of the NGO substrate is very weak, corresponding to an amorphous carbon marker layer which was deposited on top of the annealed substrate before sample preparation for TEM. This leads to the conclusion that the A-site termination may be very hard to stabilize. Wrong termination also hampers superconductivity at the interface which could not be detected in this study. A distorted region at the interface with a thickness of about 4 nm can also be detected by XRD scans [70], which excludes artifacts from sample preparation for TEM. Distortions close to the interface indicate unstable growth conditions of the CCO layer. The

main reason for this behavior may be a residual chemical and thermodynamic instability of CCO under the used deposition conditions. Changing substrate termination introduces additional strain on the epitaxial layer. Several other groups [62, 63] also experienced difficulties in preparing CCO thin-films on NGO substrates. Balestrino et al. [62] also found a broadening of the rocking curves in XRD spectra with a corresponding mosaic spread comparable to our results. Oh and Eckstein [63] found hints at secondary phases. The growth was reported to be more stable due to the introduction of nucleation layers of $SrCuO_2$ [55], deposited on the substrate before CCO deposition. However, $SrCuO_2$ on NGO may impede superconductivity.

To find evidence for superconductivity at the interface due to hole doping of the CuO_2 planes by apex oxygen, perfect layer growth is essential because defects and secondary phases also were reported to introduce superconductivity in related systems [67–69]. Despite the distortions at the interface, the material above the distorted interface was found to be of a very good quality. Vertical distortions are introduced by twin boundaries detected by HRTEM (Figure 5.3) which are responsible for the mosaic spread which was measured to be as low as 0.1 ° [70]. The formation of twin boundaries was already shown to be a relaxation mechanism for epitaxial grown thin-films of related material systems [143] and were also reported by Balestrino et al. [62] for the same material system. However, some undistorted interface regions were found by TEM and were evaluated with regard to termination.

For a film thickness larger than 10 nm precipitates of Cu_2O and CuO were found by lattice spacing analysis. As these precipitates do not occur immediately at the interface, one can exclude impurities in the PLD target. The formation of the precipitates takes place either in the gas phase on top the film after the coating process or during the film growth due to the intrinsic thermodynamic instability of CCO. To reduce this effect, the substrate temperature during coating was chosen as low as possible (650 °C-800 °C). The phase diagram of CCO published by Kobayashi et al. [54] also supports the hypothesis of the thermodynamic instability leading to the decomposition. At conditions like they also usually occur during PLD $CaCuO_2$ decomposes into $CaCuO_3$ and CuO. However, the validity of a phase diagram for epitaxial films during PLD coating has to be scrutinized as these systems are far from thermodynamic equilibrium. According to Ito et al. [149] both, the formation of CuO and Cu_2O are possible under the conditions in the PLD system during deposition. While stable epitaxial growth can be achieved for several atomic layers by PLD, for a larger layer thickness a decomposition takes place. Despite the enrichment of Cu-oxide, no Ca-rich phase was found. This result rises the question how this deviation can be achieved from a stoichiometric target. As Ca-atoms are very light compared to the Cu-cations the EDXS signal is expected to be weak. Small Ca-containing precipitates could therefore neither be detected by EDXS, nor by XRD due to the small overall size.

The intensity analysis of HAADF STEM images hampered by several problems in this system. At first GaO and CuO cannot be distinguished due to the similarity of their atomic numbers (see Table 5.1). The intensities measured in the linescan of Figure 5.5 give rise to both, Ca-CuO-Nd-GaO (A-termination) and CuO-Ca-GaO-Nd (B-termination) stacking as explanation. Furthermore, broadening of the electron probe is a severe problem for the heavy and therefore strongly scattering Nd-columns. Broadening influences the GaO signal, which is convoluted with the Nd-signal. For that reason background subtraction is necessary. Any subtraction of background signal, however, disables the evaluation of the relative intensity and the comparison with image simulations. To prevent these negative effects, the investigation of very thin samples is necessary. As CCO is strongly influenced by amorphisation at thin sample regions, the microscopist has to find a compromise. VanAert et al. [81] describe an evaluation method for quantitative HAADF STEM which resolves atomic number differences up to $\Delta Z=3$ by not only parameterizing the intensity of the columns but also their widths modeled as two dimensional Gaussian. By comparison of known columns of the substrate and deeper in the epitaxial layer, one can also identify the type of the columns at the interface. However, for the current material system with a difference in the atomic number of $\Delta Z=2$, even modern data analysis reaches its limits.

6 Summary

This work was motivated by the degradation of the oxygen-ion conductivity of $Ba_{0.5}Sr_{0.5}Co_{0.8}Fe_{0.2}O_{3-\delta}$ (BSCF), a promising material for oxygen separation membranes, in the application-relevant temperature range between 600 °C and 900 °C. The degradation of the performance of BSCF is associated with the decomposition of the cubic BSCF phase which has been in detail studied in this work. In a further step the knowledge on the decomposition of BSCF was applied to stabilize the cubic phase by doping with single-valent cations and by surface coating.

To achieve these goals, a wide range of electron microscopical techniques was applied. In addition to the application of standard methods, new electron microscopic techniques and evaluation methods were developed. This comprises a Scanning Electron Microscopy (SEM)-based analysis method which facilitates the fast mapping of different BSCF phases as a prerequisite to study a large quantity of samples. After etching with a SiO_2 suspension, different BSCF phases can be recognized. This technique was applied to large batches of samples avoiding time-consuming Transmission Electron Microscopy (TEM) investigations.

Another methodological development concerns the determination of the valence state of multivalent Co-cations which is essential for the understanding of the decomposition of the cubic phase. An established method for Co-valence state determination relies on the measurement of the intensity ratio of the Co-$L_{2,3}$ white-lines which can be derived from Electron Energy Loss Spectroscopy (EELS) measurements. This technique cannot be applied for BSCF because the Co-$L_{2,3}$ white-lines are superimposed by the Ba-$M_{4,5}$ white-lines. The new method is based on the measurement of the distance of the Co-$L_{2,3}$ white-lines. It was shown, that the Co-valence state can be determined with an accuracy of up to ± 0.2.

The new technique allows the acquisition of Co-valence maps because the Co-$L_{2,3}$ white-line distance determination can be automated. Co-valence mapping is further facilitated by the implementation of Principal Component Analysis (PCA) which significantly improves the signal-to-noise ratio. Moreover, qualitative element maps obtained by Energy-Dispersive X-ray Spectroscopy (EDXS) also benefit from PCA because noise-reduced data allows the assessment of composition changes of trace elements.

The decomposition of the undoped cubic BSCF phase was studied on the basis of bulk and thin-film samples which were annealed in the temperature range between 650 °C and 1000 °C. Co-oxide precipitates were found in all samples after annealing. The formation of the hexagonal BSCF phase at temperatures of $T \leq 840$ °C was confirmed which nucleates at grain boundaries. Furthermore, a secondary phase with plate-like morphology was detected in the course of the work which is formed after annealing at $T \leq 900$ °C. The plate-like regions also act as nucleation centers for the hexagonal phase. The microstructure and composition of the plate-like regions were in detail analyzed. They consist of thin lamellae of the cubic, hexagonal and $Ba_{n+1}Co_nO_{3n+3}(Co_8O_8)$ (BCO)-type phases. The BCO-type phase was detected at $T \leq 900$ °C.

Chemical analyses of the different phases were performed to achieve a deeper understanding of cation segregation. The hexagonal phase is depleted in Fe which is compensated by an increased Co-content. The BCO-type phase is characterized by the absence of Sr and the deviation from the ABO_3 composition of the perovskite structure.

The formation of the hexagonal phase is believed to be induced by a decreasing oxygen vacancy concentration at temperatures below 840 °C. To achieve charge balance, the Co-cations are reported to increase their valence state from 2+ towards a 3+ configuration. The associated reduction of the Co-ion radius leads to a lattice shearing from the cubic towards the hexagonal configuration. This model was validated in the present work. The Co-valence state in the cubic phase was determined to be $+2.2 \pm 0.2$ after annealing at 650 °C. In the hexagonal phase an increased Co-valence of $+2.8 \pm 0.2$ was observed.

The observation of the change of the Co-valence state in the hexagonal phase suggests that doping with single-valent cations on the B-site could be promising for the stabilization of the cubic BSCF phase. Microstructural investigations indeed demonstrated an improvement of the stability of the cubic phase for 3 % Y- and Zr-doping.

Y successfully suppresses the formation of plate-like regions and Co-oxide precipitates after annealing in the interesting temperature range (700 °C-1000 °C). This leads to an overall smaller amount of hexagonal phase due to the lack of nucleation centers. Zr was demonstrated to either shift the transition temperature of any secondary phase formation towards lower temperatures, or significantly decelerates the formation rate of secondary phases. It was shown by chemical analyses that dopants diffuse out of the hexagonal phase and, therefore, potentially cause the slower kinetics.

In addition to bulk material, epitaxial BSCF films were produced by Pulsed Laser Deposition (PLD) on $NdGaO_3$ (NGO) and $(LaAlO_3)_{0.3}(Sr_2AlTaO_6)_{0.7}$ (LSAT) substrates to study surface effects of the degradation caused by CO_2 and water vapor in the annealing atmosphere. Beside the hexagonal phase and plate-like regions, Ba- and Sr-rich

surface phases were found after annealing in air. They correspond to carbonates and hydroxides of the earth alkalies. Furthermore, a large volume fraction of Co-oxide precipitates were found in the BSCF films.
To stabilize the BSCF surface and to improve oxygen surface exchange, a nanoporous $La_xSr_{1-x}CoO_{3-\delta}$ (LSC) functional layer was deposited on top of the BSCF films. It was demonstrated, that further precipitation of A-site cation enriched phases could be suppressed. However, secondary phases are formed as in the bulk samples.

The results of this work have considerably extended the understanding of the decomposition of the cubic BSCF phase. Moreover, strategies for the stabilization of the cubic BSCF phase can be derived to avoid the degradation of the O-ion conductivity in long-term applications of BSCF as oxygen separation membrane. The investigation of undoped BSCF indicates that the main stability issues might stem from an excess of Co which could be overcome by a slight change of the composition of the B-site cations. The elucidation of the effect of Zr- and Y-doping will be the basis for next-generation BSCF materials. Optimization of the dopant concentration and the combination of different promising dopants are expected to further improve the stability of BSCF. Additionally, a decrease of the operation temperature without significant performance losses appears possible due to new membrane materials and sophisticated surface coatings like LSC which improves oxygen surface exchange.

In the second part of this work, $CaCuO_2$ (CCO)-NGO interfaces were studied by TEM. The main objective in this field of research is to stabilize epitaxial CCO layers on a substrate providing a pyramidal oxygen coordination at the interface. If the fabrication challenges can be overcome, superconductivity at the CCO-NGO interface can be expected.
X-Ray Diffraction (XRD) investigations of the mosaic spread accompanied by High-Resolution Transmission Electron Microscopy (HRTEM) on cross-section TEM samples led to the identification of a distorted interface region with a thickness of about 4 nm which prevents the development of superconductivity. The reason for the distorted growth was attributed to the residual intrinsic thermodynamic instability of CCO despite stabilization due to strained epitaxial growth on NGO. Furthermore, it was diagnosed by High-Angle Annular Dark-Field (HAADF) Scanning Transmission Electron Microscopy (STEM) that the production of purely A-site terminated NGO, providing the pyramidal oxygen coordination, is very challenging. In the present study, only a preferential A-site termination was achieved. The stacking sequence of the different atomic sites at the interface was also directly probed by HAADF STEM with atomic-resolution. It was demonstrated that a difference of the atomic number of $\Delta Z=2$ for GaO and CuO columns can not be resolved by quantitative STEM investigations.

List of Figures

List of Tables

Bibliography

[1] A. S. Bhalla, R. Guo, and R. Roy. The perovskite structure - a review of its role in ceramic science and technology. *Materials Research Innovations*, **4**, 3–26 (2000). doi:10.1007/s100190000062.

[2] H. Bouwmeester and A. J. Burggraaf. *The CRC handbook of solid state electrochemistry (chapter 14)*. CRC Press (1997). doi:10.1201/9781420049305.

[3] M. Czyperek, P. Zapp, H. Bouwmeester, M. Modigell, K. Ebert, I. Voigt, W. Meulenberg, L. Singheiser, and D. Stöver. Gas separation membranes for zero-emission fossil power plants: MEM-BRAIN. *Journal of Membrane Science*, **359**(1-2), 149–59 (2010). doi:10.1016/j.memsci.2010.04.012.

[4] S. M. Hashim, A. R. Mohamed, and S. Bhatia. Current status of ceramic-based membranes for oxygen separation from air. *Advances in Colloid and Interface Science*, **160**(1-2), 88–100 (2010). doi:10.1016/j.cis.2010.07.007.

[5] A. Leo, S. Liu, and J. C. D. da Costa. Development of mixed conducting membranes for clean coal energy delivery. *International Journal of Greenhouse Gas Control*, **3**, 357–367 (2009). doi:10.1016/j.ijggc.2008.11.003.

[6] Y. Liu, X. Tan, and K. Li. Mixed conducting ceramics for catalytic membrane processing. *Catalysis Reviews: Science and Engineering*, **48**, 145–198 (2006). doi:10.1080/01614940600631348.

[7] J. Sunarso, S. Baumann, J. Serra, W. Meulenberg, S. Liu, Y. Lin, and J. D. da Costa. Mixed ionic-electronic conducting (MIEC) ceramic-based membranes for oxygen separation. *Journal of Membrane Science*, **320**(1-2), 13–41 (2008). doi:10.1016/j.memsci.2008.03.074.

[8] Z. Chen, R. Ran, Z. Shao, H. Yu, J. C. D. da Costa, and S. Liu. Further performance improvement of $Ba_{0.5}Sr_{0.5}Co_{0.8}Fe_{0.2}O_{3-\delta}$ perovskite membranes for air separation. *Ceramics International*, **35**, 2455–2461 (2009). doi:10.1016/j.ceramint.2009.02.015.

[9] B. Cales and J. Baumard. Oxygen semipermeability and electronic conductivity in calcia-stabilized zirconia. *Journal of Materials Science*, **17**, 3243–3248 (1982). doi:10.1007/BF01203490.

[10] Y. Teraoka, H.-M. Zhang, S. Furukawa, and N. Yamazoe. Oxygen permeation through perovskite-type oxides. *Chemistry Letters*, **14**(11), 1743–1746 (1985). doi:10.1246/cl.1985.1743.

[11] Y. Teraoka, H. Zhang, K. Okamoto, and N. Yamazoe. Mixed ionic-electronic conductivity of $La_{1-x}Sr_xCo_{1-y}Fe_yO_{3-\delta}$ perovskite-type oxides. *Materials Research Bulletin*, **23**(1), 51–58 (1988). doi:10.1016/0025-5408(88)90224-3.

[12] Z. Shao, W. Yang, Y. Cong, H. Dong, J. Tong, and G. Xiong. Investigation of the permeation behavior and stability of a $Ba_{0.5}Sr_{0.5}Co_{0.8}Fe_{0.2}O_{3-\delta}$ oxygen membrane. *Journal of Membrane Science*, **172**, 177–188 (2000). doi:10.1016/S0376-7388(00)00337-9.

[13] Persistence of Vision Pty. Ltd. (2004). Persistence of vision raytracer (version 3.6). *Retrieved from http://www.povray.org/download/.*

[14] L. W. Finger, M. Kroeker, and B. H. Toby. *DRAWxtl*, an open-source computer program to produce crystal structure drawings. *Journal of Applied Crystallography*, **40**(1), 188–192 (2007). doi:10.1107/S0021889806051557.

[15] V. Goldschmidt. Die Gesetze der Krystallochemie. *Die Naturwissenschaften*, **21**, 477–485 (1926). doi:10.1007/BF01507527.

[16] R. D. Shannon. Revised effective ionic radii and systematic studies of interatomic distances in halides and chalcogenides. *Acta Crystallographica Section A*, **32**(5), 751–767 (1976). doi:10.1107/S0567739476001551.

[17] P. Zeng, Z. Chen, W. Zhou, H. Gu, Z. Shao, and S. Liu. Re-evaluation of $Ba_{0.5}Sr_{0.5}Co_{0.8}Fe_{0.2}O_{3-\delta}$ perovskite as oxygen semi-permeable membrane. *Journal of Membrane Science*, **291**, 148–156 (2007). doi:10.1016/j.memsci.2007.01.003.

[18] J. Serra, V. Vert, M. Betz, V. Haanappel, W. Meulenberg, and F. Tietz. Screening of A-substitution in the system $A_{0.68}Sr_{0.3}Fe_{0.8}Co_{0.2}O_{3-\delta}$ for SOFC cathodes. *Journal of the Electrochemical Society*, **155**(2), B207–B214 (2008). doi:10.1149/1.2818766.

[19] J. Ovenstone, J.-I. Jung, J. S. White, D. D. Edwards, and S. T. Misture. Phase stability of BSCF in low oxygen partial pressures. *Journal of solid state chemistry*, **181**, 576–586 (2008). doi:10.1016/j.jssc.2008.01.010.

[20] M. A. Alaee, M. M. Movahednia, and T. Mohammadi. Effect of Ba content on oxygen permeation performance of $Ba_xSr_{1-x}Co_{0.8}Fe_{0.2}O_{3-d}$ (x = 0.2, 0.5, and 0.8)

perovskite-type membrane. *Journal of Chemical & Engineering Data*, **54**(11), 3082–3091 (2009). doi:10.1021/je9001762.

[21] Z. Shao, G. Xiong, J. Tong, H. Dong, and W. Yang. Ba effect in doped $Sr(Co_{0.8}Fe_{0.2})O_{3-\delta}$ on the phase structure and oxygen permeation properties of the dense ceramic membranes. *Separation and Purification Technology*, **25**(1-3), 419–429 (2001). doi:10.1016/S1383-5866(01)00071-5.

[22] S. Švarcová, K. Wiik, J. Tolchard, H. J. Bouwmeester, and T. Grande. Structural instability of cubic perovskite $Ba_xSr_{1-x}Co_{1-y}Fe_yO_{3-\delta}$. *Solid State Ionics*, **178**(35-36), 1787–1791 (2008). doi:10.1016/j.ssi.2007.11.031.

[23] M. Arnold, T. M. Gesing, J. Martynczuk, and A. Feldhoff. Correlation of the formation and the decomposition process of the BSCF perovskite at intermediate temperatures. *Chemistry of Materials*, **20**(18), 5851–5858 (2008). doi:10.1021/cm801463h.

[24] K. Efimov, Q. Xu, and A. Feldhoff. Transmission electron microscopy study of $Ba_{0.5}Sr_{0.5}Co_{0.8}Fe_{0.2}O_{3-\delta}$ perovskite decomposition at intermediate temperatures. *Chemistry of Materials*, **22**(21), 5866–5875 (2010). doi:10.1021/cm101745v.

[25] Z.-P. Shao and W.-S. Y. Guo-Xing Xiong. Systematic selection of mixed conducting perovskite materials for oxygen separation. *Journal of Inorganic Materials*, **16**, 297 (2001).

[26] A. S. Harvey, F. J. Litterst, Z. Yang, J. L. M. Rupp, A. Infortuna, and L. J. Gauckler. Oxidation states of Co and Fe in $Ba_{1-x}Sr_xCo_{1-y}Fe_yO_{3-\delta}$ (x, y = 0.2-0.8) and oxygen desorption in the temperature range 300-1273 K. *Physical Chemistry Chemical Physics*, **11**(17), 3090–3098 (2009). doi:10.1039/B819414A.

[27] Y. Teraoka, M. Yoshimatsu, N. Yamazoe, and T. Seiyama. Oxygen-sorptive properties and defect structure of perovskite-type oxides. *Chemistry Letters*, **13**(6), 893–896 (1984). doi:10.1246/cl.1984.893.

[28] M. Arnold, Q. Xu, F. D. Tichelaar, and A. Feldhoff. Local charge disproportion in a high-performance perovskite. *Chemistry of Materials*, **21**(4), 635–640 (2009). doi:10.1021/cm802779f.

[29] J. Sun, M. Yang, G. Li, T. Yang, F. Liao, Y. Wang, M. Xiong, and J. Lin. New barium cobaltite series $Ba_{n+1}Co_nO_{3n+3}Co_8O_8$: Intergrowth structure containing perovskite and CdI_2-type layers. *Inorganic Chemistry*, **45**(23), 9151–9153 (2006). doi:10.1021/ic060992v.

[30] R. David, A. Pautrat, H. Kabbour, M. Sturza, S. Curelea, G. André, D. Pelloquin, and O. Mentré. $(BaCoO_3)_n(BaCo_8O_{11})$ modular intergrowths: Singularity of the n = 2 term. *Chemistry of Materials*, **23**(23), 5191–5199 (2011). doi:10.1021/cm202106t.

[31] D. N. Mueller, R. A. de Souza, T. E. Weirich, D. Roehrens, J. Mayer, and M. Martin. A kinetic study of the decomposition of the cubic perovskite-type oxide $Ba_xSr_{1-x}Co_{0.8}Fe_{0.2}O_{3-\delta}$ (BSCF) (x = 0.1 and 0.5). *Physical Chemistry Chemical Physics*, **12**, 10320–10328 (2010). doi:10.1039/c0cp00004c.

[32] A. S. Harvey, Z. Yang, A. Infortuna, D. Beckel, J. A. Purton, and L. J. Gauckler. Development of electron holes across the temperature-induced semiconductor-metal transition in $Ba_{1-x}Sr_xCo_{1-y}Fe_yO_{3-d}$ (x , y = 0.2-0.8): a soft X-ray absorption spectroscopy study. *Journal of Physics: Condensed Matter*, **21**(1), 015801 (2009). doi:10.1088/0953-8984/21/1/015801.

[33] Z. Yáng, A. S. Harvey, A. Infortuna, and L. J. Gauckler. Phase relations in the Ba-Sr-Co-Fe-O-system at 1273 K in air. *Journal of Applied Crystallography*, **42**, 153–160 (2009). doi:10.1107/S0021889809002040.

[34] C. Niedrig, S. Taufall, M. Burriel, W. Menesklou, S. F. Wagner, S. Baumann, and E. Ivers-Tiffée. Thermal stability of the cubic phase in $Ba_{0.5}Sr_{0.5}Co_{0.8}Fe_{0.2}O_{3-\delta}$ (BSCF). *Solid State Ionics*, **197**(1), 25–31 (2011). doi:10.1016/j.ssi.2011.06.010.

[35] Y. Teraoka, H. Shimokawa, C. Y. Kang, H. Kusaba, and K. Sasaki. Fe-based perovskite-type oxides as excellent oxygen-permeable and reduction-tolerant materials. *Solid State Ionics*, **177**, 2245 – 2248 (2006). doi:10.1016/j.ssi.2006.05.037.

[36] H. Wang, C. Tablet, A. Feldhoff, and J. Caro. A cobalt-free oxygen-permeable membrane based on the perovskite-type oxide $Ba_{0.5}Sr_{0.5}Zn_{0.2}Fe_{0.8}O_{3-\delta}$. *Advanced Materials*, **17**, 1785–1788 (2005). doi:10.1002/adma.200401608.

[37] A. Feldhoff, J. Martynczuk, and H. Wang. Advanced $Ba_{0.5}Sr_{0.5}Zn_{0.2}Fe_{0.8}O_{3-\delta}$ perovskite-type ceramics as oxygen selective membranes: Evaluation of the synthetic process. *Progress in Solid State Chemistry*, **35**(2-4), 339–353 (2007). doi:10.1016/j.progsolidstchem.2007.01.007.

[38] A. Feldhoff, J. Martynczuk, M. Arnold, M. Myndyk, I. Bergmann, V. Šepelák, W. Gruner, U. Vogt, A. Hähnel, and J. Woltersdorf. Spin-state transition of iron in $(Ba_{0.5}Sr_{0.5})(Fe_{0.8}Zn_{0.2})O_{3-\delta}$ perovskite. *Journal of Solid State Chemistry*, **182**(11), 2961–2971 (2009). doi:10.1016/j.jssc.2009.07.058.

[39] J. Martynczuk, K. Efimov, and A. Feldhoff. Performance of zinc-doped perovskite-type membranes at intermediate temperatures for long-term oxygen permeation and under a carbon dioxide atmosphere. *Journal of Membrane Science*, **344**, 62–70 (2009). doi:10.1016/j.memsci.2009.07.035.

[40] J. Martynczuk, F. Liang, M. Arnold, V. Šepelák, and A. Feldhoff. Aluminum-doped perovskites as high-performance oxygen permeation materials. *Chemistry of Materials*, **21**(8), 1586–1594 (2009). doi:10.1021/cm803217t.

[41] L. Zhao, B. He, X. Zhang, R. Peng, G. Meng, and X. Liu. Electrochemical performance of novel cobalt-free oxide $Ba_{0.5}Sr_{0.5}Fe_{0.8}Cu_{0.2}O_{3-\delta}$ for solid oxide fuel cell cathode. *Journal of Power Sources*, **195**(7), 1859–1861 (2010). doi:10.1016/j.jpowsour.2009.09.078.

[42] X. Meng, B. Meng, X. Tan, N. Yang, and Z.-F. Ma. Synthesis and properties of $Ba_{0.5}Sr_{0.5}(Co_{0.6}Zr_{0.2})Fe_{0.2}O_{3-\delta}$ perovskite cathode material for intermediate temperature solid-oxide fuel cells. *Materials Research Bulletin*, **44**(6), 1293–1297 (2009). doi:10.1016/j.materresbull.2008.12.015.

[43] S. Yakovlev, C.-Y. Yoo, S. Fang, and H. J. M. Bouwmeester. Phase transformation and oxygen equilibration kinetics of pure and Zr-doped $Ba_{0.5}Sr_{0.5}Co_{0.8}Fe_{0.2}O_{3-\delta}$ perovskite oxide probed by electrical conductivity relaxation. *Applied Physics Letters*, **96**(25), 254101 (2010). doi:10.1063/1.3455908.

[44] P. Haworth, S. Smart, J. Glasscock, and J. D. da Costa. Yttrium doped BSCF membranes for oxygen separation. *Separation and Purification Technology*, **81**(1), 88–93 (2011). doi:10.1016/j.seppur.2011.07.007.

[45] P. Haworth, S. Smart, J. Glasscock, and J. D. da Costa. High performance yttrium-doped BSCF hollow fibre membranes. *Separation and Purification Technology*, **94**(0), 16 – 22 (2012). doi:10.1016/j.seppur.2012.04.005.

[46] M. Arnold, H. Wang, and A. Feldhoff. Influence of CO_2 on the oxygen permeation performance and the microstructure of perowskite-type $(Ba_{0.5}Sr_{0.5})(Co_{0.8}Fe_{0.2})O_{3-\delta}$ membranes. *Journal of Membrane Science*, **293**, 44–52 (2007). doi:10.1016/j.memsci.2007.01.032.

[47] A. Yan, V. Maragou, A. Arico, M. Cheng, and P. Tsiakaras. Investigation of a $Ba_{0.5}Sr_{0.5}Co_{0.8}Fe_{0.2}O_3$ based cathode SOFC: II. the effect of CO_2 on the chemical stability. *Applied Catalysis B: Environmental*, **76**, 320–327 (2007). doi:10.1016/j.apcatb.2007.06.010.

[48] J. Yi and M. Schroeder. High temperature degradation of $Ba_{0.5}Sr_{0.5}Co_{0.8}Fe_{0.2}O_{3-\delta}$ membranes in atmospheres containing concentrated carbon dioxide. *Journal of Membrane Science*, **378**(1-2), 163–170 (2011). doi:10.1016/j.memsci.2011.04.044.

[49] W. K. Hong and G. M. Choi. Oxygen permeation of BSCF membrane with varying thickness and surface coating. *Journal of Membrane Science*, **346**(2), 353–360 (2010). doi:10.1016/j.memsci.2009.09.056.

[50] J. Hayd, L. Dieterle, U. Guntow, D. Gerthsen, and E. Ivers-Tiffée. Nanoscaled $La_{0.6}Sr_{0.4}CoO_3$ as intermediate temperature solid oxide fuel cell cathode: Microstructure and electrochemical performance. *Journal of Power Sources*, **196**(17), 7263–7270 (2011). doi:10.1016/j.jpowsour.2010.11.147.

[51] L. Dieterle, P. Bockstaller, D. Gerthsen, J. Hayd, E. Ivers-Tiffée, and U. Guntow. Microstructure of nanoscaled $La_{0.6}Sr_{0.4}CoO_{3-\delta}$ cathodes for intermediate-temperature solid oxide fuel cells. *Advanced Energy Materials*, **1**(2), 249–258 (2011). doi:10.1002/aenm.201000036.

[52] H. Zhang and W. Yang. Highly efficient electrocatalysts for oxygen reduction reaction. *Chemical Communications*, (41), 4215–4217 (2007). doi:10.1039/B707907A.

[53] K. Yvon and M. François. Crystal structures of high-T_c oxides. *Zeitschrift für Physik B Condensed Matter*, **76**, 413–444 (1989). doi:10.1007/BF01307892.

[54] N. Kobayashi, Z. Hiroi, and M. Takano. Compounds and phase relations in the SrO-CaO-CuO system under high pressure. *Journal of Solid State Chemistry*, **132**(2), 274–283 (1997). doi:10.1006/jssc.1997.7442.

[55] A. Gupta, B. Hussey, T. Shaw, A. Guloy, M. Chern, R. Saraf, and B. Scott. Layer-by-layer growth of thin films of the infinite-layer compounds $SrCuO_2$ and $CaCuO_2$. *Journal of Solid State Chemistry*, **112**(1), 113–119 (1994). doi:10.1006/jssc.1994.1274.

[56] T. Siegrist, S. M. Zahurak, D. W. Murphy, and R. S. Roth. The parent structure of the layered high-temperature superconductors. *Nature*, **334**(6179), 231–232 (1988). doi:10.1038/334231a0.

[57] H. Yamauchi, M. Karppinen, and S. Tanaka. Homologous series of layered cuprates. *Physica C: Superconductivity*, **263**(1-4), 146–150 (1996). doi:10.1016/0921-4534(96)00075-5.

[58] C. Kim, A. Y. Matsuura, Z.-X. Shen, N. Motoyama, H. Eisaki, S. Uchida, T. Tohyama, and S. Maekawa. Observation of spin-charge separation in one-dimensional $SrCuO_2$. *Phys. Rev. Lett.*, **77**, 4054–4057 (1996). doi:10.1103/PhysRevLett.77.4054.

[59] T. Ohnishi, K. Takahashi, M. Nakamura, M. Kawasaki, M. Yoshimoto, and H. Koinuma. A-site layer terminated perovskite substrate: $NdGaO_3$. *Applied Physics Letters*, **74**(17), 2531–2533 (1999). doi:10.1063/1.123888.

[60] M. Kawasaki, K. Takahashi, T. Maeda, R. Tsuchiya, M. Shinohara, O. Ishiyama, T. Yonezawa, M. Yoshimoto, and H. Koinuma. Atomic control of the $SrTiO_3$ crystal surface. *Science*, **266**(5190), 1540–1542 (1994). doi:10.1126/science.266.5190.1540.

[61] D. Di Castro, M. Salvato, A. Tebano, D. Innocenti, C. Aruta, W. Prellier, O. I. Lebedev, I. Ottaviani, N. B. Brookes, M. Minola, M. M. Sala, C. Mazzoli, P. Medaglia, G. Ghiringhelli, L. B. M. Cirillo, and G. Balestrino. High Tc superconductivity in superlattices of insulating oxides. *ArXiv e-prints [cond-mat.supr-con]* (2011). doi:10.1103/PhysRevB.86.134524.

[62] G. Balestrino, R. Desfeux, S. Martellucci, A. Paoletti, G. Petrocelli, A. Tebano, B. Mercey, and M. Hervieu. Growth of $CaCuO_2$ and $Sr_xCa_{1-x}CuO_2$ epitaxial films on $NdGaO_3$ substrates by pulsed laser deposition. *Journal of Materials Chemistry*, **5**, 1879–1883 (1995). doi:10.1039/JM9950501879.

[63] S. Oh and J. Eckstein. Infinite-layer ($Ca_{1-x}Sr_xCuO_2$) film growth by molecular beam epitaxy and effect of hole doping. *Thin Solid Films*, **483**(1-2), 301–305 (2005). doi:10.1016/j.tsf.2005.01.087.

[64] G. A. Ovsyannikov, S. A. Denisuk, I. K. Bdikin, Z. G. Ivanov, and T. Claeson. The growth and conductivity of $CaCuO_2$ epitaxial thin films. *Physica C: Superconductivity*, **408-410**(0), 616–617 (2004). doi:10.1016/j.physc.2004.03.050.

[65] G. A. Ovsyannikov, V. V. Demidov, Y. V. Kislinski, P. V. Komissinski, and D. Winkler. Conductivity and antiferromagnetism of $CaCuO_2$ thin films doped by Sr. *Physica C: Superconductivity*, **460-462**, 536–537 (2007). doi:10.1016/j.physc.2007.03.144.

[66] J. Schön, M. Dorget, F. Beuran, X. Zu, E. Arushanov, C. D. Cavellin, and M. Laguës. Superconductivity in $CaCuO_2$ as a result of field-effect doping. *Nature*, **414**(6862), 434–6 (2001). rejected.

[67] M. Azuma, Z. Hiroi, M. Takano, Y. Bando, and Y. Takeda. Superconductivity at 110 K in the infinite-layer compound $(Sr_{1-x}Ca_x)_{1-y}CuO_2$. *Nature*, **356**(6372), 775–776 (1992). doi:10.1038/356775a0.

[68] C. Prouteau, P. Strobel, J. Capponi, C. Chaillout, and J. Tholence. Optimization of superconductivity in the high-pressure Sr-Ca-Cu-O system. *Physica C: Superconductivity*, **228**, 63–72 (1994). doi:10.1016/0921-4534(94)90174-0.

[69] H. Shaked, Y. Shimakawa, B. A. Hunter, R. L. Hitterman, J. D. Jorgensen, P. D. Han, and D. A. Payne. Superconductivity in the Sr-Ca-Cu-O system and the phase with infinite-layer structure. *Phys. Rev. B*, **51**, 11784–11790 (1995). doi:10.1103/PhysRevB.51.11784.

[70] D. Fuchs, P. Müller, A. Sleem, R. Schneider, D. Gerthsen, and H. v. Löhneysen. Growth and interfacial properties of epitaxial $CaCuO_2$ thin films. *Journal of Applied Physics*, **112**(10), 103529 (2012). doi:10.1063/1.4767117.

[71] D. B. Williams and C. B. Carter. *Transmission Electron Microscopy - A textbook for Materials Science*. Springer, 2 edition (2009). doi:10.1007/978-0-387-76501-3.

[72] L. Reimer. *Scanning Electron Microscopy: Physics of Image Formation and Microanalysis*. Springer, 2 edition (1998).

[73] P. Stadelmann. Image analysis and simulation software in transmission electron microscopy. *Microscopy and Microanalysis*, **9**, 60–61 (2003). doi:10.1017/S1431927603012224.

[74] J. Ayache, L. Beaunier, J. Boumendil, G. Ehret, and D. Laub. *Sample Preparation Handbook for Transmission Electron Microscopy - Techniques*. Springer (2010).

[75] H. Koster and F. H. Mertins. Powder Diffraction of the cubic perovskite $Ba_{0.5}Sr_{0.5}Co_{0.8}Fe_{0.2}O_{3-\delta}$. *Powder Diffraction*, **18**(1), 56–59 (2003). doi:10.1154/1.1536927.

[76] A. V. Crewe. Scanning electron microscopes: Is high resolution possible? *Science*, **154**(3750), 729–738 (1966). doi:10.1126/science.154.3750.729.

[77] A. V. Crewe, J. Wall, and L. M. Welter. A high-resolution scanning transmission electron microscope. *Journal of Applied Physics*, **39**(13), 5861–5868 (1968). doi:10.1063/1.1656079.

[78] J. Wall, J. Langmore, M. Isaacson, and A. V. Crewe. Scanning transmission electron microscopy at high resolution. *Proceedings of the National Academy of Sciences*, **71**(1), 1–5 (1974).

[79] A. Crewe. Electron microscopes using field emission source. *Surface Science*, **48**(1), 152 – 160 (1975). doi:10.1016/0039-6028(75)90314-3.

[80] D. H. Shin, E. J. Kirkland, and J. Silcox. Annular dark field electron microscope images with better than 2 Å resolution at 100 kV. *Applied Physics Letters*, **55**(23), 2456–2458 (1989). doi:10.1063/1.102297.

[81] S. V. Aert, J. Verbeeck, R. Erni, S. Bals, M. Luysberg, D. V. Dyck, and G. V. Tendeloo. Quantitative atomic resolution mapping using high-angle annular dark field scanning transmission electron microscopy. *Ultramicroscopy*, **109**(10), 1236–1244 (2009). doi:10.1016/j.ultramic.2009.05.010.

[82] S. J. Pennycook. *A Scan Through the History of STEM*. Springer New York (2011). doi:10.1007/978-1-4419-7200-2.

[83] J. P. Morniroli and J. W. Steeds. Microdiffraction as a tool for crystal structure identification and determination. *Ultramicroscopy*, **45**(2), 219 – 239 (1992). doi:10.1016/0304-3991(92)90511-H.

[84] B. F. Buxton, J. A. Eades, J. W. Steeds, and G. M. Rackham. The symmetry of electron diffraction zone axis patterns. *Philosophical Transactions of the Royal Society of London. Series A, Mathematical and Physical Sciences*, **281**(1301), 171–194 (1976).

[85] H. Hotelling. Analysis of a complex of statistical variables into principal components. *Journal of Educational Psychology*, **24**(6), 417–441 (1933).

[86] A. Miranda, Y.-A. Borgne, and G. Bontempi. New routes from minimal approximation error to principal components. *Neural Processing Letters*, **27**, 197–207 (2008). doi:10.1007/s11063-007-9069-2.

[87] M. Meffert. Elektronenmikroskopische Untersuchung von $(Ba_{0,5}Sr_{0,5})(Co_{0,8}Fe_{0,2})_{0,97}X_{0,03}O_{3-\delta}$ (X=Zr, Sc, Y) (2012). Diploma thesis.

[88] G. Cliff and G. W. Lorimer. The quantitative analysis of thin specimens. *Journal of Microscopy*, **103**(2), 203–207 (1975). doi:10.1111/j.1365-2818.1975.tb03895.x.

[89] Z. Horita, T. Sano, and M. Nemoto. An extrapolation method for the determination of Cliff-Lorimer k_{AB} factors at zero foil thickness. *Journal of Microscopy*, **143**(3), 215–231 (1986). doi:10.1111/j.1365-2818.1986.tb02779.x.

[90] Z. Horita, T. Sano, and M. Nemoto. Simplification of X-ray absorption correction in thin-sample quantitative microanalysis. *Ultramicroscopy*, **21**(3), 271–276 (1987). doi:10.1016/0304-3991(87)90152-5.

[91] C. T. Chantler. Theoretical form factor, attenuation, and scattering tabulation for Z=1-92 from E=1-10 eV to E=0.4-1.0 MeV. *Journal of Physical and Chemical Reference Data*, **24**(1), 71–643 (1995). doi:10.1063/1.555974.

[92] C. Chantler, K. Olsen, R. Dragoset, J. Chang, A. Kishore, S. Kotochigova, and D. Zucker. X-ray form factor, attenuation and scattering tables (2005). http://physics.nist.gov/PhysRefData/FFast/html/form.html.

[93] R. Kriegel, R. Kircheisen, and J. Töpfer. Oxygen stoichiometry and expansion behavior of $Ba_{0.5}Sr_{0.5}Co_{0.8}Fe_{0.2}O_{3-d}$. *Solid State Ionics*, **181**(1-2), 64–70 (2010). doi:10.1016/j.ssi.2009.11.012.

[94] C. C. Ahn, editor. *Transmission Electron Energy Loss Spectrometry in Materials Science and the EELS Atlas*. Wiley-VCH, 2 edition (2004). doi:10.1002/3527605495.

[95] R. D. Leapman and L. A. Grunes. Anomalous L_3/L_2 white-line ratios in the 3d transition metals. *Phys. Rev. Lett.*, **45**, 397–401 (1980). doi:10.1103/PhysRevLett.45.397.

[96] B. T. Thole and G. van der Laan. Branching ratio in X-ray absorption spectroscopy. *Phys. Rev. B*, **38**, 3158–3171 (1988). doi:10.1103/PhysRevB.38.3158.

[97] D. H. Pearson, C. C. Ahn, and B. Fultz. White lines and d-electron occupancies for the 3 d and 4 d transition metals. *Phys. Rev. B*, **47**, 8471–8478 (1993). doi:10.1103/PhysRevB.47.8471.

[98] Z. Wang, J. Yin, and Y. Jiang. EELS analysis of cation valence states and oxygen vacancies in magnetic oxides. *Micron*, **31**(5), 571–580 (2000). doi:10.1016/S0968-4328(99)00139-0.

[99] Z. Wang, J. Bentley, and N. Evans. Valence state mapping of cobalt and manganese using near-edge fine structures. *Micron*, **31**(4), 355–362 (2000). doi:10.1016/S0968-4328(99)00114-6.

[100] H. Shuman and A. Somlyo. Electron energy loss analysis of near-trace-element concentrations of calcium. *Ultramicroscopy*, **21**(1), 23 – 32 (1987). doi:10.1016/0304-3991(87)90004-0.

[101] R. Leapman and C. Swyt. Separation of overlapping core edges in electron energy loss spectra by multiple-least-squares fitting. *Ultramicroscopy*, **26**(4), 393–403 (1988). doi:10.1016/0304-3991(88)90239-2.

[102] J. Fink, T. Müller-Heinzerling, B. Scheerer, W. Speier, F. U. Hillebrecht, J. C. Fuggle, J. Zaanen, and G. A. Sawatzky. 2p absorption spectra of the 3d elements. *Phys. Rev. B*, **32**, 4899–4904 (1985). doi:10.1103/PhysRevB.32.4899.

[103] F. M. F. de Groot, M. Abbate, J. van Elp, G. A. Sawatzky, Y. J. Ma, C. T. Chen, and F. Sette. Oxygen 1s and cobalt 2p X-ray absorption of cobalt oxides. *Journal of Physics: Condensed Matter*, **5**(14), 2277 (1993). doi:10.1088/0953-8984/5/14/023.

[104] F. de Groot. X-ray absorption and dichroism of transition metals and their compounds. *Journal of Electron Spectroscopy and Related Phenomena*, **67**(4), 529–622 (1994). doi:10.1016/0368-2048(93)02041-J.

[105] F. de Groot. Multiplet effects in X-ray spectroscopy. *Coordination Chemistry Reviews*, **249**(1-2), 31–63 (2005). doi:10.1016/j.ccr.2004.03.018.

[106] M. Abbate, J. C. Fuggle, A. Fujimori, L. H. Tjeng, C. T. Chen, R. Potze, G. A. Sawatzky, H. Eisaki, and S. Uchida. Electronic structure and spin-state transition of $LaCoO_3$. *Phys. Rev. B*, **47**, 16124–16130 (1993). doi:10.1103/PhysRevB.47.16124.

[107] C. Mitterbauer, G. Kothleitner, W. Grogger, H. Zandbergen, B. Freitag, P. Tiemeijer, and F. Hofer. Electron energy-loss near-edge structures of 3d transition metal oxides recorded at high-energy resolution. *Ultramicroscopy*, **96**(3-4), 469–480 (2003). doi:10.1016/S0304-3991(03)00109-8.

[108] J. Zaanen and G. A. Sawatzky. Strong interference between decay channels and valence-electron rearrangements in core-hole spectroscopy. *Phys. Rev. B*, **33**, 8074–8083 (1986). doi:10.1103/PhysRevB.33.8074.

[109] J. Haeberle. Elektronenmikroskopische Untersuchung von BSCF (2012). Bachelor thesis.

[110] C. A. Schneider, W. S. Rasband, and K. W. Eliceiri. NIH Image to ImageJ: 25 years of image analysis. *Nat Meth*, **9**(7), 671–675 (2012). doi:10.1038/nmeth.2089.

[111] F. Liang, H. Jiang, H. Luo, J. Caro, and A. Feldhoff. Phase stability and permeation behavior of a dead-end $Ba_{0.5}Sr_{0.5}Co_{0.8}Fe_{0.2}O_{3-\delta}$ tube membrane in high-

purity oxygen production. *Chemistry of Materials*, **23**(21), 4765–4772 (2011). doi:10.1021/cm2018086.

[112] M. Burriel, C. Niedrig, W. Menesklou, S. F. Wagner, J. Santiso, and E. Ivers-Tiffée. BSCF epitaxial thin films: Electrical transport and oxygen surface exchange. *Solid State Ionics*, **181**(13-14), 602–608 (2010). doi:10.1016/j.ssi.2010.03.005.

[113] S. Sasaki, K. Fujino, and Y. Takéuchi. X-ray determination of electron-density distributions in oxides, MgO, MnO, CoO, and NiO, and atomic scattering factors of their constituent atoms. *Proceedings of the Japan Academy, Series B*, **55**(2), 43–48 (1979).

[114] J. Picard, G. Baud, J. Besse, and R. Chevalier. Croissance cristalline et Étude structurale de Co_3O_4. *Journal of the Less Common Metals*, **75**(1), 99–104 (1980). doi:10.1016/0022-5088(80)90373-2.

[115] C. Gammer, C. Mangler, C. Rentenberger, and H. Karnthaler. Quantitative local profile analysis of nanomaterials by electron diffraction. *Scripta Materialia*, **63**(3), 312–315 (2010). doi:10.1016/j.scriptamat.2010.04.019.

[116] B. Albrecht. Elektronenmikroskopische Untersuchungen an BSCF3X/LSC - Dünnschichtsystemen (X=Zr, Y) (2013). Diploma thesis.

[117] K. Yamaura, H. Zandbergen, K. Abe, and R. Cava. Synthesis and properties of the structurally one-dimensional cobalt oxide $Ba_{1-x}Sr_xCoO_3$ ($0 \leq x \leq 0.5$). *Journal of Solid State Chemistry*, **146**(1), 96–102 (1999). doi:10.1006/jssc.1999.8313.

[118] P. Müller, H. Störmer, L. Dieterle, C. Niedrig, E. Ivers-Tiffée, and D. Gerthsen. Decomposition pathway of cubic $Ba_{0.5}Sr_{0.5}Co_{0.8}Fe_{0.2}O_{3-\delta}$ between 700 °C and 1000 °C analyzed by electron microscopic techniques. *Solid State Ionics*, **206**(0), 57–66 (2012). doi:10.1016/j.ssi.2011.10.013.

[119] B. Fisher and D. S. Tannhauser. The phase diagram of cobalt monoxide at high temperatures. *Journal of The Electrochemical Society*, **111**(10), 1194–1196 (1964). doi:10.1149/1.2425953.

[120] M. Chen, B. Hallstedt, and L. Gauckler. Thermodynamic assessment of the co-o system. *Journal of Phase Equilibria*, **24**, 212–227 (2003). doi:10.1361/105497103770330514.

[121] M. Oku and Y. Sato. In-situ X-ray photoelectron spectroscopic study of the reversible phase transition between CoO and Co_3O_4 in oxygen of 10^{-3} pa. *Applied Surface Science*, **55**(1), 37–41 (1992). doi:10.1016/0169-4332(92)90378-B.

[122] B. Rutkowski, J. Malzbender, R. Steinbrech, T. Beck, and H. Bouwmeester. Influence of thermal history on the cubic-to-hexagonal phase transformation and creep behaviour of $Ba_{0.5}Sr_{0.5}Co_{0.8}Fe_{0.2}O_{3-\delta}$ ceramics. *Journal of Membrane Science*, **381**(1-2), 221–225 (2011). doi:10.1016/j.memsci.2011.07.036.

[123] L. Katz and R. Ward. Structure relations in mixed metal oxides. *Inorganic Chemistry*, **3**(2), 205–211 (1964). doi:10.1021/ic50012a013.

[124] K. Yvon and E. Parthé. On the crystal chemistry of the close-packed transition-metal carbides. I. The crystal structure of the ζ-V, Nb and Ta carbides. *Acta Crystallographica Section B*, **26**(2), 149–153 (1970). doi:10.1107/S0567740870002091.

[125] E. Parthé and K. Yvon. On the crystal chemistry of the close packed transition metal carbides. II. A proposal for the notation of the different crystal structures. *Acta Crystallographica Section B*, **26**(2), 153–163 (1970). doi:10.1107/S0567740870002108.

[126] J. Hutchison and A. Jacobson. Electron microscopy of the perovskite-related phases 4H $Ba_{0.1}Sr_{0.9}MnO_{2.96}$, 5H $Ba_5Nb_4O_{15}$ and 6H $BaFeO_{2.79}$. *Journal of Solid State Chemistry*, **20**(4), 417–422 (1977). doi:10.1016/0022-4596(77)90179-7.

[127] J. van Landuyt, G. van Tendeloo, and S. Amelinckx. High resolution electron microscopy of polytypes. *Progress in crystal growth and characterization*, **7**, 343–378 (1983).

[128] K. Boulahya, M. Parras, and J. M. González-Calbet. The $A_{n+2}B_nB'O_{3n+3}$ family (B=B'=Co): Ordered intergrowth between 2H-$BaCoO_3$ and $Ca_3Co_2O_6$ structures. *Journal of Solid State Chemistry*, **145**(1), 116–127 (1999). doi:10.1006/jssc.1999.8230.

[129] K. Boulahya, M. Parras, and J. M. Gonzalez-Calbet. New commensurate phases in the family $(A_3Co_2O_6)_\alpha(A_3Co_3O_9)_\beta$ (A = Ca, Sr, Ba). *Chemistry of Materials*, **12**(1), 25–32 (2000). doi:10.1021/cm991028g.

[130] K. Boulahya, M. Parras, and J. M. Gonzalez-Calbet. The orthorhombic $(Ba_8Co_6O_{18})_\alpha(Ba_8Co_8O_{24})_\beta$ series, a new family of monodimensional oxides. *Chemistry of Materials*, **12**(9), 2727–2735 (2000). doi:10.1021/cm001056v.

[131] K. Boulahya, M. Parras, J. M. González-Calbet, and A. Vegas. A new orthorhombic $Ba_8Co_7O_{21}$ phase: Polymorphism in the $(Ba_3Co_2O_6)_\alpha(Ba_3Co_3O_9)_\beta$ system. *Journal of Solid State Chemistry*, **151**(1), 77–84 (2000). doi:10.1006/jssc.2000.8625.

[132] J. Darriet, L. Elcoro, A. El Abed, E. Gaudin, and J. M. Perez-Mato. Crystal structure of $Ba_{12}Co_{11}O_{33}$. Reinvestigation using the superspace group approach of orthorhombic oxides $A_{1+x}(A'_xB_{1-x})O_3$ based on $[A_8O_{24}]$ and $[A_8A'_2O_{18}]$ layers. *Chemistry of Materials*, **14**(8), 3349–3363 (2002). doi:10.1021/cm0211610.

[133] L. Ge, W. Zhou, R. Ran, S. Liu, Z. Shao, W. Jin, and N. Xu. Properties and performance of A-site deficient $(Ba_{0.5}Sr_{0.5})_{1-x}Co_{0.8}Fe_{0.2}O_{3-\delta}$ for oxygen permeating membrane. *Journal of Membrane Science*, **306**(1-2), 318–328 (2007). doi:10.1016/j.memsci.2007.09.004.

[134] L. Ge, R. Ran, K. Zhang, S. Liu, and Z. Shao. Oxygen selective membranes based on B-site cation-deficient $(Ba_{0.5}Sr_{0.5})(Co_{0.8}Fe_{0.2})O_{3-\delta}$ perovskite with improved operational stability. *Journal of Membrane Science*, **318**, 182–190 (2008). doi:10.1016/j.memsci.2008.02.015.

[135] K. Zhang, R. Ran, L. Ge, Z. Shao, W. Jin, and N. Xu. Double-site yttria-doped $Sr_{1-x}Y_xCo_{1-y}Y_yO_{3-\delta}$ perovskite oxides as oxygen semi-permeable membranes. *Journal of Alloys and Compounds*, **474**(1-2), 477–483 (2009). doi:10.1016/j.jallcom.2008.06.120.

[136] R. Ran, Y. Guo, D. Gao, S. Liu, and Z. Shao. Effect of foreign oxides on the phase structure, sintering and transport properties of $Ba_{0.5}Sr_{0.5}Co_{0.8}Fe_{0.2}O_{3-\delta}$ as ceramic membranes for oxygen separation. *Separation and Purification Technology*, **81**(3), 384–391 (2011). doi:10.1016/j.seppur.2011.08.005.

[137] K. Kerman, B.-K. Lai, and S. Ramanathan. Thin film nanocrystalline $Ba_{0.5}Sr_{0.5}Co_{0.8}Fe_{0.2}O_3$: Synthesis, conductivity, and micro-solid oxide fuel cells. *Journal of Power Sources*, **196**(15), 6214–6218 (2011). doi:10.1016/j.jpowsour.2011.03.049.

[138] J. Martynczuk, M. Arnold, and A. Feldhoff. Influence of grain size on the oxygen permeation performance of perovskite-type $(Ba_{0.5}Sr_{0.5})(Fe_{0.8}Zn_{0.2})O_{3-\delta}$ membranes. *Journal of Membrane Science*, **322**(2), 375–382 (2008). doi:10.1016/j.memsci.2008.05.064.

[139] M. Arnold, J. Martynczuk, K. Efimov, H. Wang, and A. Feldhoff. Grain boundaries as barrier for oxygen transport in perovskite-type membranes. *Journal of Membrane Science*, **316**(1-2), 137–144 (2008). doi:10.1016/j.memsci.2007.10.002.

[140] S. Baumann, F. Schulze-Küppers, S. Roitsch, M. Betz, M. Zwick, E. Pfaff, W. Meulenberg, J. Mayer, and D. Stöver. Influence of sintering conditions on

microstructure and oxygen permeation of $Ba_{0.5}Sr_{0.5}Co_{0.8}Fe_{0.2}O_{3-\delta}$ (BSCF) oxygen transport membranes. *Journal of Membrane Science*, **359**(1-2), 102–109 (2010). doi:10.1016/j.memsci.2010.02.002.

[141] M. Mogensen, D. Lybye, N. Bonanos, P. Hendriksen, and F. Poulsen. Factors controlling the oxide ion conductivity of fluorite and perovskite structured oxides. *Solid State Ionics*, **174**(1-4), 279–286 (2004). doi:10.1016/j.ssi.2004.07.036.

[142] A. C. v. Veen, M. Rebeilleau, D. Farrusseng, and C. Mirodatos. Studies on the performance stability of mixed conducting BSCFO membranes in medium temperature oxygen permeation. *Chem. Commun.*, **2003**, 32–33 (2003). doi:10.1039/B207848A.

[143] D. Fuchs, L. Dieterle, E. Arac, R. Eder, P. Adelmann, V. Eyert, T. Kopp, R. Schneider, D. Gerthsen, and H. v. Löhneysen. Suppression of the ferromagnetic state in $LaCoO_3$ films by rhombohedral distortion. *Phys. Rev. B*, **79**, 024424 (2009). doi:10.1103/PhysRevB.79.024424.

[144] S. Åsbrink and L.-J. Norrby. A refinement of the crystal structure of copper(II) oxide with a discussion of some exceptional e.s.d.'s. *Acta Crystallographica Section B*, **26**(1), 8–15 (1970). doi:10.1107/S0567740870001838.

[145] M. Foo, Q. Huang, J. Lynn, W.-L. Lee, T. Klimczuk, I. Hagemann, N. Ong, and R. Cava. Synthesis, structure and physical properties of Ru ferrites: $BaMRu_5O_{11}$ (M=Li and Cu) and $BaM'_2Ru_4O_{11}$ (M'=Mn, Fe and Co). *Journal of Solid State Chemistry*, **179**(2), 563–572 (2006). doi:10.1016/j.jssc.2005.11.014.

[146] Y. Gotoh, I. Yamaguchi, Y. Takahashi, J. Akimoto, M. Goto, M. Onoda, H. Fujino, T. Nagata, and J. Akimitsu. Structural modulation, hole distribution, and hole-ordered structure of the incommensurate composite crystal $(Sr_2Cu_2O_3)_{0.70}CuO_2$. *Phys. Rev. B*, **68**, 224108 (2003). doi:10.1103/PhysRevB.68.224108.

[147] D. Lines, M. Weller, D. Currie, and D. Ogbome. Alkaline earth copper oxides. *Materials Research Bulletin*, **26**(4), 323–331 (1991). doi:10.1016/0025-5408(91)90028-K.

[148] M. Wojdyr. *Fityk*: a general-purpose peak fitting program. *Journal of Applied Crystallography*, **43**(5 Part 1), 1126–1128 (2010). doi:10.1107/S0021889810030499.

[149] T. Ito, H. Yamaguchi, K. Okabe, and T. Masumi. Single-crystal growth and characterization of Cu_2O and CuO. *Journal of Materials Science*, **33**, 3555–3566 (1998). doi:10.1023/A:1004690809547.

Own publications and contributions to conferences

Reviewed publications

- P. Müller, L. Dieterle, E. Müller, H. Störmer, D. Gerthsen, C. Niedrig, S. Taufall, S.F. Wagner, and E. Ivers-Tiffée. $Ba_{0.5}Sr_{0.5}Co_{0.8}Fe_{0.2}O_{3-\delta}$ (BSCF) for oxygen separation membranes. *ECS Transactions*, **28**, 309-314 (2010). doi: 10.1149/1.3495854

- P. Müller, H. Störmer, L. Dieterle, C. Niedrig, E. Ivers-Tiffée, and D. Gerthsen. Decomposition pathway of cubic $Ba_{0.5}Sr_{0.5}Co_{0.8}Fe_{0.2}O_{3-\delta}$ (BSCF) between 700 °C and 1000 °C analyzed by electron microscopic techniques. *Solid State Ionics*, **206**(1), 57-66 (2012). doi: 10.1016/j.ssi.2011.10.013

- D. Fuchs, P. Müller, A. Sleem, R. Schneider, D. Gerthsen, and H. v. Löhneysen. Interfacial growth and properties of the infinite layer compound $CaCuO_2$. *Journal of Applied Physics* **112**, 103529 (2012). doi: 10.1063/1.4767117

- P. Müller, H. Störmer, M. Meffert, L. Dieterle, C. Niedrig, S.F. Wagner, E. Ivers-Tiffée, and D. Gerthsen. Secondary phase formation in $Ba_{0.5}Sr_{0.5}Co_{0.8}Fe_{0.2}O_{3-\delta}$ (BSCF) studied by electron microscopy. *Chemistry of Materials*, **25**, 564-573 (2013). doi: 10.1021/cm303670m

- P. Müller, M. Meffert, H. Störmer, and D. Gerthsen. Fast mapping of the cobalt valence state in $Ba_{0.5}Sr_{0.5}Co_{0.8}Fe_{0.2}O_{3-d}$ by Electron Energy Loss Spectroscopy. *Microscopy & Microanalysis* (submitted).

Reviewed publications on other topics

- Y.-C. Hung, P. Müller, Y.-S. Wang, and L. Fruk. Phototriggered growth of crystalline Au structures in the presence of a DNA-surfactant complex. *Nanoscale* **4**, 5585-5587 (2012). doi: 10.1039/c2nr31618h

- B. Geiseler, M. Miljevic, P. Müller, and L. Fruk. Phototriggered Production of Reactive Oxygen by TiO_2 Nanospheres and Rods. *Journal of Nanomaterials*

2012, ID 708519 (2012). doi: 10.1155/2012/708519

- M. Pfaff, M. Klein, E. Müller, P. Müller, A. Colsmann, U. Lemmer, and D. Gerthsen. Nanomorphology of P3HT:PCBM-based absorber layers of organic solar cells after different processing conditions analyzed by low-energy scanning transmission electron microscopy. *Microscopy & Microanalysis* **Vol**(18), 1380-1388 (2012). doi: 10.1017/S143192761201344X

  Status: March 2013

Contributions to conferences

- P. Müller, H. Störmer, M. Burriel, C. Niedrig, S. Wagner, E. Ivers-Tiffée, and D. Gerthsen. Microstructural and Electrochemical Properties of Mixed Ionic/ Electronic Conducting (MIEC) $Ba_{0.5}Sr_{0.5}Co_{0.8}Fe_{0.2}O_{3-\delta}$ (BSCF) Perovskite Materials (Poster). *11th international Fischer Symposium on Microscopy in Electrochemistry*, Benediktbeuern, Germany, July 26-31 (2009).

- P. Müller, H. Störmer, D. Gerthsen, J. Santiso, J. Roqueta, M. Burriel, C. Niedrig, S. Wagner, and E. Ivers-Tiffée. TEM investigations of mixed ionic/ electronic conducting $Ba_{0.5}Sr_{0.5}Co_{0.8}Fe_{0.2}O_{3-\delta}$ (BSCF) materials (Poster). *Microscopy Conference - MC2009*, Graz, Austria, August 30-September 4 (2009).

- P. Müller, L. Dieterle, E. Müller, H. Störmer, D. Gerthsen, C. Niedrig, S. Taufall, S.F. Wagner, and E. Ivers-Tiffée. $Ba_{0.5}Sr_{0.5}Co_{0.8}Fe_{0.2}O_{3-\delta}$ (BSCF) for Oxygen Separation Membranes (Talk). *217th ECS Meeting* Vancouver, Canada, April 25-30 (2010).

- P. Müller, H. Störmer, L. Dieterle, D. Gerthsen, and D. Fuchs. Transmission Electron Microscopy Investigations of $Ba_{0.5}Sr_{0.5}Co_{0.8}Fe_{0.2}O_{3-\delta}$ (BSCF) Thin Films Fabricated by Pulsed-Laser Deposition (PLD) (Talk). *Electroceramics XII*, Trondheim, Norway, June 14-17 (2010).

- P. Müller, L. Dieterle, H. Störmer, and D. Gerthsen. Determination of the Crystal Structure of $Ba_{0.5}Sr_{0.5}Co_{0.8}Fe_{0.2}O_{3-\delta}$ (BSCF) by Electron Diffraction (Poster). *Workshop: Facets of Electron Crystallography*, Berlin, Germany, July 7-9 (2010).

- P. Müller, H. Störmer, L. Dieterle , D. Gerthsen, M. Burriel, C. Niedrig, S. Wagner, and E. Ivers-Tiffée. Nanostructured Functional Layers for Advanced Oxygen Separation Membranes (Poster). *1st International Conference on Materials for Energy*, Karlsruhe, Germany, July 4-8 (2010).

- P. Müller, L. Dieterle, H. Störmer, D. Gerthsen, and D. Fuchs. Determination of Phase Composition of $Ba_{0.5}Sr_{0.5}Co_{0.8}Fe_{0.2}O_{3-\delta}$ (BSCF) under Application-Relevant Conditions using Advanced Electron Microscopy (Poster). *Summer School: Ceramic Membranes for Green Chemical Production ans Clean Power Generation*, Valencia, Spain, September 8-10 (2010).

- P. Müller, H. Störmer, L. Dieterle, C. Niedrig, S.F. Wagner, D. Gerthsen, and E. Ivers-Tiffée. Determination of the Phase Composition in $Ba_{0.5}Sr_{0.5}Co_{0.8}Fe_{0.2}O_{3-\delta}$ (BSCF) by means of Electron Microscopy (Talk). *18th International Conference on Solid State Ionics*, Warsaw, Poland, July 3-8 (2011).

- P. Müller, H. Störmer, L. Dieterle, N. Firman, and D. Gerthsen. Investigation of the decomposition pathway of cubic $Ba_{0.5}Sr_{0.5}Co_{0.8}Fe_{0.2}O_{3-\delta}$ (BSCF) by electron microscopy (Poster). *Microscopy Conference - MC2011*, Kiel, Germany, August 28-September 2 (2011).

- P. Müller, M. Meffert, H. Störmer, C. Niedrig, S.F. Wagner, E. Ivers-Tiffée, and D. Gerthsen. Electron Microscopy investigations of zirconium-, yttrium- and scandium-doped $Ba_{0.5}Sr_{0.5}(Co_{0.8}Fe_{0.2})_{0.97}X_{0.03}O_{3-\delta}$ (BSCF3X) (Talk). *Electroceramics XIII*, Enschede, Netherlands, June 24-27 (2012).

- C. Niedrig, P. Müller, B. Albrecht, W. Menesklou, S. F. Wagner, H. Störmer, D. Gerthsen, and E. Ivers-Tiffée. Enhanced Oxygen Surface Exchange in BSCF (Poster). *Electroceramics XIII*, Enschede, Netherlands, June 24-27 (2012).

- P. Müller, M. Meffert, H. Störmer, C. Niedrig, S. F. Wagner, E. Ivers-Tiffée, and D. Gerthsen. Analysis of co-doped $Ba_{0.5}Sr_{0.5}(Co_{0.8}Fe_{0.2})_{0.97}X_{0.03}O_{3-\delta}$ (BSCF3X) by Electron Microscopy (Poster). *12th International Conference on Inorganic Membranes*, Enschede, Netherlands, July 9-13 (2012).

- M. Pfaff, M. F. G. Klein, E. Müller, P. Müller, A. Colsmann, U. Lemmer, and D. Gerthsen. Nanomorphology of P3HT:PCBM-based Organic Solar Cells Analyzed by Low-Energy Scanning Transmission Electron Microscopy (Poster). *Microscopy & Microanalysis 2012*, Phoenix, USA, July 29-August 2 (2012).

- K. Gao, P. Müller, M. Faust, R. Schneider, and M. Seipenbusch. In situ observation of sintering behavior of Pt particles supported on silica nanoparticles. *European Aerosol Conference*, Granada, Spain, September 2-7 (2012).

- P. Müller, B. Albrecht, H, Störmer, D. Fuchs, C. Niedrig, S. F. Wagner, E. Ivers-Tiffée, and D. Gerthsen. Electron microscopy study of surface-functionalized

$Ba_{0.5}Sr_{0.5}Co_{0.8}Fe_{0.2}O_{3-\delta}$ (BSCF) membranes (awarded Poster). *The 15th European Microscopy Congress*, Manchester, United Kingdom, September 16-21 (2012).

- M. Meffert, P. Müller, H. Störmer, C. Niedrig, S. F. Wagner, E. Ivers-Tiffée, and D. Gerthsen. Electron microscopy study of $Ba_{0.5}Sr_{0.5}(Co_{0.8}Fe_{0.2})_{0.97}X_{0.03}O_{3-\delta}$ (BSCF3X) (Poster). *The 15th European Microscopy Congress*, Manchester, United Kingdom, September 16-21 (2012).

- M. Pfaff, M. F. G. Klein, J. Subbiah, E. Müller, P. Müller, A. Colsmann, W. W. H. Wong, A. B. Holmes, U. Lemmer, D. J. Jones, and D. Gerthsen. Nanomorphology of fluorenyl hexa-peri-hexabenzocoronene-based absorber layers of organic solar cells (Talk). *The 15th European Microscopy Congress*, Manchester, United Kingdom, September 16-21 (2012).

- M. Pfaff, M. F. G. Klein, E. Müller, P. Müller, A. Colsmann, U. Lemmer, and D. Gerthsen. Low-energy scanning transmission electron microscopy studies of P3HT:PCBM-based organic solar cell absorber layers (Poster). *The 15th European Microscopy Congress*, Manchester, United Kingdom, September 16-21 (2012).

- M. Pfaff, M. F. G. Klein, E. Müller, P. Müller, A. Colsmann, U. Lemmer, and D. Gerthsen. Nanomorphology of P3HT:PCBM-based Organic Solar Cells Analyzed by Low-Energy Scanning Transmission Electron Microscopy (Poster). *CFN Summerschool 2012 on Nano-Energy*, Bad Herrenalb, Germany, September 14-17 (2012).

- M. Meffert, P. Müller, H. Störmer, C. Niedrig, S. F. Wagner, E. Ivers-Tiffée, and D. Gerthsen. Electron microscopy study of $Ba_{0.5}Sr_{0.5}(Co_{0.8}Fe_{0.2})_{0.97}X_{0.03}O_{3-\delta}$ (BSCF3X) (Poster). *CFN Summerschool 2012 on Nano-Energy*, Bad Herrenalb, Germany, September 14-17 (2012).

- C. Niedrig, P. Müller, B. Albrecht, W. Menesklou, S. F. Wagner, H. Störmer, D. Gerthsen, and E. Ivers-Tiffée. Enhanced Oxygen Surface Exchange in BSCF (Poster). *CFN Summerschool 2012 on Nano-Energy*, Bad Herrenalb, Germany, September 14-17 (2012).

- B. Albrecht, P. Müller, H. Störmer, D. Fuchs, C. Niedrig, W. Menesklou, S.F. Wagner, E. Ivers-Tiffée, and D. Gerthsen. Enhanced Oxygen Surface Exchange in $Ba_{0.5}Sr_{0.5}Co_{0.8}Fe_{0.2}O_{3-\delta}$ (BSCF) (Poster). *CFN Summerschool 2012 on Nano-Energy*, Bad Herrenalb, Germany, September 14-17 (2012).

- K. Gao, M. Yu, P. Müller, R. Schneider, D. Gerthsen, M. Seipenbusch. In- and ex-situ observation of the ripening of supported noble metal nanoparticles (Poster). *Nano-structure in disperse systems: production, characterization and functionality*, Karlsruhe, Germany, November 12-13 (2012).

- M. Meffert, P. Müller, H. Störmer, C. Niedrig, S. F. Wagner, E. Ivers-Tiffée, and D. Gerthsen. Electron microscopy study of Y-doped BSCF (Talk). *DPG spring meeting SKM*, Regensburg, Germany, March 10-15 (2013).

- K. Gao, P. Müller, R. Schneider, D. Gerthsen, and M. Seipenbusch. Ripening of the noble metal supported nanoparticles and in situ observation. *International Congress on Particle Technology*, Nürnberg, Germany, April 23-25 (2013)

- M. Meffert, P. Müller, H. Störmer, C. Niedrig, S. F. Wagner, E. Ivers-Tiffée, and D. Gerthsen. Electron Microscopy Study of Yttrium-doped BSCF3Y (Talk). *2nd International Conference on Materials for Energy*, Karlsruhe, Germany, May 12-16 (2013).

- M. Meffert, P. Müller, H. Störmer, C. Niedrig, S. F. Wagner, E. Ivers-Tiffée, and D. Gerthsen. Electron Microscopy Study of Yttrium-doped BSCF3Y (talk). *Solid State Ionics*, Kyoto, Japan, June 2-7 (2013).

Status: March 2013

Danksagung

An dieser Stelle möchte ich mich bei allen bedanken, die mich während meiner Arbeit am LEM unterstützt haben.

Prof. Dr. Dagmar Gerthsen danke ich für die exzellente Betreuung meiner Arbeit und für die vielen wertvollen Tipps und guten Ratschläge bei Konferenzbeiträgen und Veröffentlichungen. Bei der Überarbeitung von Manuskripten zeigte Sie eine ungebrochene Geduld und gab mit ihrem umfangreichen Fachwissen viele neue Denkanstöße.

Des Weiteren möchte ich mich bei Prof. Dr.-Ing. Ellen Ivers-Tiffée für die Übernahme des Korreferates und die vielen guten Ratschläge bei gemeinsamen Besprechungen bedanken.

Heike Störmer half mir eigentlich bei allem Denkbaren und ist mit die beste Kollegin die man sich vorstellen kann. Aufgrund ihrer langjährigen Erfahrung in Elektronenmikroskopie und Materialwissenschaften ist sie die ideale Ansprechpartnerin eines jeden Doktoranden. Danke Heike!

Levin Dieterle war während meiner Diplomarbeit und in der Anfangsphase meiner Doktorarbeit mein Onkel für alles und gab viele wertvolle Tipps zu Probenpräparation, Kristallografie und natürlich Elektronenmikroskopie.

Vielen Dank an Frau Sauter für die ganze unsichtbare Hilfe im Hintergrund und die ermunternen Worte zwischen Tür und Angel.

Vielen Dank an Matthias Meffert, Benjamin Albrecht und Jan Haeberle für die gute Zusammenarbeit während eurer Diplomarbeiten bzw. Bachelorarbeit zu BSCF! Ich wünsche euch alles Gute für eure weitere wissenschaftliche Laufbahn!

Ohne die Hilfe von Nadejda Firman wäre diese Arbeit nicht zustande gekommen. Vielen Dank für deine Hilfe bei allen Fragen zu Präparation und für all die Proben bei denen du mir bei der Präparation geholfen hast!

Bei Herrn Schneider möchte ich mich für die Hilfe bei der Mikroskopie und die Korrektur der Kapitel zur Elektronenmikroskopie bedanken.

Mein Dank geht auch an Dirk Fuchs, für die gute Zusammenarbeit, die wertvollen Diskussionen und die Hilfe bei der Probenherstellung.

Ich danke Christian Niedrig und Stefan Wagner für die gute Kooperation, die Probenherstellung und aufwendigen Charakterisierungen unserer Proben.

Mein Dank geht auch an Prof. Armin Feldhoff (Universität Hannover) für die wertvollen Diskussionen im Rahmen von Tagungen und während meines Besuchs in Hannover.

Vielen Dank an Prof. Henny Bouwmeester und Dr. Chung-Yul Yoo (Universität Twente) für die gute Kooperation!

Vielen Dank an Ljiljana Fruk und ihre Gruppe für die gute Kooperation bei der Charakterisierung von Nanoteilchen!

Danke an Kun Gao für die gute Zusammenarbeit bei der Untersuchung von Edelmetall-Katalysatoren.

Vielen Dank an Anne Kast, die mir den entscheidenden Tipp für die Zeit nach der Doktorarbeit gab!

Natürlich geht mein Dank auch an alle weiteren Kollegen am LEM. Bei Fragen zu Geräten oder wissenschaftlichen Themen gab es immer einen kompetenten Ansprechpartner.
Die wichtigsten aller Kollegen sind aber natürlich die LEM-Lauf-Freunde (n.e.V.). Sie sorgen mit ihren wöchentlichen Laufveranstaltungen und den Après-Jogg-Events für den nötigen körperlichen und geistigen Ausgleich nach der Arbeit und spornen durch die jährlichen Sportveranstaltungen zu Höchstleistungen an.

Großes Lob auch an die fleißigen und begabten Konditoren Anne, Simon und Lukas!

Vielen Dank an meine Eltern, meinen Bruder und meine Freunde die mich bei allen meinen Entscheidungen unterstützt haben und dadurch immer einen wichtigen Rückhalt boten.

Danke Marina für alles !!!